Earth-abundant water-splitting catalysts coupled to silicon solar cells for solar-to-fuels conversion

Share Your Story

The Harvard community has made this article openly available.
Please share how this access benefits you. Submit a story .

Accessibility

Earth–abundant water–splitting catalysts coupled to

silicon solar cells for solar–to–fuels conversion.

A dissertation presented

by

Casandra R. Cox

to

The Department of Chemistry and Chemical Biology

in partial fulfillment of the requirements

for the degree of

Doctor of Philosophy

in the subject of

Chemistry

Harvard University

Cambridge, Massachusetts

September 2014

Casandra R. Cox   Daniel G. Nocera

Earth–abundant water–splitting catalysts coupled to silicon solar cells for solar–to–fuels conversion.

Abstract

Direct solar–to–fuels conversion can be achieved by coupling semiconductors with water–splitting catalysts. A 10% or higher solar to fuels conversion is minimally necessary for the realization of a robust future technology. Many water–splitting devices have been proposed but due to expensive designs and/or materials, none have demonstrated the necessary efficiency at low–cost that is a requisite for large–scale implementation. In this thesis, a modular approach is used to couple water–splitting catalysts with crystalline silicon (c–Si) photovoltaics, with ultimate goal of demonstrating a stand–alone and direct solar-to-fuels water–splitting device comprising all non–precious, technology ready, materials.

Since the oxygen evolution reaction is the key efficiency–limiting step for water–splitting, we first focus on directly interfacing oxygen evolution catalysts with c–Si photovoltaics. Due to the instability of silicon under oxidizing conditions, a protective interface between the PV and OER catalyst is required. This coupling of catalyst to Si semiconductor thus requires optimization of two interfaces: the silicon|protective layer interface; and, the protective layer|catalyst interface. A modular approach allows for the independent optimization and analysis of these two interfaces.

A stand–alone water–splitting device based on c–Si is created by connecting multiple single junction c-Si solar cells in series. Steady–state equivalent circuit analysis allows for a targeted solar–to–fuels efficiency to be designed within a predictive framework for a series–connected c–Si solar cells and earth–abundant water–splitting catalysts operating at neutral pH. Guided by simulation and modeling, a completely modular, stand–alone water–splitting device possessing a 10% SFE is demonstrated. Importantly, the modular approach enables facile characterization and trouble–shooting for each component of the solar water–splitting device. Finally, as direct solar water–splitting is far from a mature technology, alternative concepts are presented for the future design and integration of solar water–splitting devices based on all earth–abundant materials.

Table of Contents

List of Figures

List of Tables

List of Abbreviations

ALD	atomic–layer deposition
AM	air mass
a–Si	amorphous silicon
b	Tafel slope
BJ	buried junction
BOS	balance of systems
B_i	borate buffer
c_b	bulk concentration
CIGS	copper indium gallium diselenide
CoB_i	cobalt–based catalysts deposited from borate electrolyte
CoP_i	cobalt–based catalysts deposited from phosphate electrolyte
c–Si	crystalline silicon
CV	cyclic voltammogram or cyclic voltammetry
CVD	chemical vapor deposition
D	diffusion coefficient
E-beam	electron beam evaporation
EC	electrochemical
E_F	Fermi energy or level
F	Faraday's constant
FF	fill factor
FTO	fluorine doped tin oxide
HEC	hydrogen–evolution catalyst
HER	hydrogen–evolution reaction
ITO	tin–doped indium oxide
J	current–density
J_0	exchange current density
J_{SC}	short–circuit current
k_b	Boltzmann's constant
MPP	maximum power–point
n	ideality factor
NHE	normal hydrogen electrode
NiB_i	nickel based catalyst deposited from borate electrolyte
NiFeO	nickel iron oxide
OEC	oxygen evolution catalyst
OER	oxygen evolution reaction
P	power
PCET	proton–coupled electron tranfer
PEC	photoelectrochemical
PSII	photosystem I
PSII	photosystem II
P_i	phosphate buffer
PV	photovoltaic
q	charge

R	resistance
s	series
SEI	semiconductor electrolyte interface
SEM	scanning electron micrograph
SFE	solar–to–fuels efficiency
sh	shunt
SJ	solution junction
sol	solution
T	temperature
TCO	transparent conductive oxide
th	thermodynamic
V_{Appl}	potential applied to the electrode
V_{OC}	open circuit voltage
W_P	watt at peak power
η	overpotential
η_C	coupling efficiency
η_{EC}	electrochemical efficiency
η_{PV}	PV efficiency
δ	Nernst diffusion layer

Acknowledgments

During the past six years at MIT and then at Harvard, I have had the pleasure of meeting some amazing people and scientists during this time and I would like to thank them for having an impact on me and my decisions.

From a scientific perspective I first have to thank my PhD advisor Dan Nocera. I have learned a lot from him. He has taught me many technical skills including how to write a paper, how to make my research accessible and interesting to others, and how to make pretty figures. His unique advising style of always pushing you when you need it has taught me more than anything else I've encountered in graduate school. He seems to always be so intuitive to what his students need to be successful and no matter how many times we mess up he never gives up on us.

I would also like to acknowledge my long–time collaborator Tonio Buonassisi for our many thought provoking meetings.

From my undergraduate academic experience I like to thank my under–graduate research advisor Dr. Stephen Mezyk for sparking my interest in doing research and pursuing a graduate degree.

I thank Dr. James Kiddle for being a great collaborator and kindred spirit. We have been great friends and have had so much fun together.

Now for the part most people skip to acknowledging all of the lab mates and colleagues that have inspired, influenced, and/or have just been great friends over the years:

I would like to thank Dr. Liz Young for telling me that I was not alone in feeling like I was the only person in my class who didn't understand everything and felt way too behind to keep on going. I also admire Liz's no nonsense attitude and the ability to always stand up for herself and others without being shy or afraid what others might think.

I will also have to thank Dr. Matt Kanan for always being so inspiring and kind even to a lowly first year graduate student. I was always so impressed seeing him at the Miracle of Science every Saturday with a new scientific paper to read along side a beer and burger. I also appreciate the friendship we have maintained over the years and how he always makes time to meet me for a drink when he is town.

Additionally I would like to thank Dr. Steve Reece. Although we didn't overlap, being the great mentor that he is really helped me a lot during my first few years in graduate school.

Dr. Mark Winkler was a great colleague and collaborator. For having so many helpful meetings and pep talks now and then.

Dr. Joep Pijpers got me started on my project and was a great mentor during the short time period we worked together.

Dr. Dino Villagran is one of the nicest people but somehow has made every female in lab cry over some ridiculous thing.

Dr. Alex Radosevich for teaching every one how to bootie bomb.

Dr. Bob McGuire for being such a fun and nice person.

Dr. Dilek Doğutan and I joined the Nocera lab around the same time. It has been nice seeing her progress from a post–doc to her current position where she has so much leadership responsibility. She really helps facilitate the research in our lab on a daily basis.

Dr. David Powers for giving great pep–talks during this last month and being a good friend.

Dr. Eric Bloch has been someone I have only known a short time but has been a really fun and kind person.

Dr. Tom Kempa for reading over portions of my thesis and for all of our long talks about science.

Dr. Chris Gagliardi for being such a nice and funny person.

Dr. Emily McClaurin for being such a good friend to me during my first few years. She always put up with my crisis (which were fairly often). She taught me a lot of things about how to handle myself in lab and our "CHEMREF" sessions were always helpful.

Dr. Changhoon Lee for being someone who I could never hear speak but I knew he was a kind person.

Dr. Yogesh Suredranath was the person I was most scared to present in front of at group meeting so I would go through my slides with him beforehand. He always gave time and attention to people who asked for it.

Dr. Matt Chambers for being the eternal optimist and always playing devil's advocate. We had a lot of fun times especially at the Bleacher Bar. Let's go Buffalo!

Dr. Arturo Pizano we had a lot of crazy times and I could always count on him to enable a "f* it day."

In my first year I started out as one of four and am the only one who made it through. I would specifically like to thank Pete Curtain for being such a smart and happy person. He is someone I have always missed, especially in times where I just wanted a person who could be a partner in crime during the various phases of graduate school. My last memory of a big hung before telling him good luck before he left is still one my favorite memories.

Kwabena Bediako for being so knowledgeable and helpful. However, sharing frustrations with science and graduate school with someone who makes it all seem so easy made me feel not so alone. I also always appreciate the pep talks walking home after a long day in lab.

Chris Lemon for being a great friend. Chris was always there when I needed him and was always ready to grab a beer and hang out after a long day in lab. He is one of the hardest workers in lab and never seems frustrated. I love our "gay–tes" at Cambridge Common.

Andrew Ullman for being so quirky. I have loved seeing the transformation from hippie to clean–cut and dad–like (thanks Anne Marie). His love for reading old textbooks is hilarious and he has the best smile out of anyone in lab.

Mike Huynh for being the smartest, hardest–working, and kindest person in lab all of which comes completely naturally. I think I had the best person to give group meeting with and enjoyed his delicious home–cooked treats he would surprise me with.

Bon Jun Koo I don't even know where to start. You have been a great friend and have always been there for me. Obviously my favorite thing about you is your confusion with the English language and American culture, which has made me laugh countless times. I also love your no nonsense attitude especially during long group meetings.

Nancy Li has been like a little sister to me over the past year. I love our talks about all things shopping and being terrible influences on one another when it comes to purchasing things we don't need. She is so thoughtful and such a hard worker. I think she will have a very successful PhD experience.

Dan Graham all I can say is thank you for always being the scape–goat.

Bryce Anderson and Andrew Maher are both fun, sincere, and kind people and made sharing an office with no windows seem not so bad.

Evan Jones for always seeming to be in the wrong place at the wrong time, which makes me laugh.

Seung–Jun Hwang for putting up with all of our questions on the Korean language after Bon Jun confuses us.

There have been many people I didn't get to know very well to all of you I wish the best of luck.

On a more personal note:

I would like to thank my amazing husband Eric Hontz. In the last two years he has helped me in every aspect of life. We have so much fun together and I am so excited about our future together.

I would like to thank my dad for always visiting me in every place I've lived and being proud of me.

I would like to thank my mother for being the strongest person I know. She has been so encouraging and helpful and I love her very much.

Chapter 1– Introduction:

1.1 The need for clean–energy

One of the greatest challenges facing the world today is the need for clean–renewable energy resources to supply the needs of a quickly growing world–population. Current world energy consumption is 524 quadrillion BTU (5.5 x 10^{20} Joules or 17.5 TW per year).[1] Due to an increase in world population to 3 billion people by 2050, the world energy consumption is expected to increase by 56% and double by the end of the century. [1-3] Most of this population growth is occurring in the developing world, which presently does not have the infrastructure or wealth to keep up with this demand.[4]

Presently 86% of the current world–energy is supplied by fossil fuels and it is projected that even with increase world population, fossil fuels can continue to power the planet for many years to come.[5,6] However, increasing levels of CO_2 in the atmosphere have been rising since the industrial revolution when the world population was seven times less than today. Given that human activity led to increased concentrations of CO_2 in the atmosphere with a considerably smaller population, the impact of today's rapidly growing world population could lead to much more severe results. The common goal amongst scientists and policy makers is to prevent the concentrations of CO_2 in the atmosphere from reaching levels such that the change in global temperature is more than 2^oC.[7] While it remains unclear what impact the increased global temperature will have, it seems unwise to perform an uncontrolled experiment on the environment.

This quandary necessitates new technologies to produce and store renewable energy that minimizes the environmental consequences associated with burning fossil fuels.

1.2 Renewable Energy

Due to the inefficiency of photosynthesis (1%)[8] and the spatial limitations of wind power,[9] neither biomass nor wind is a viable option to fully meet the world energy needs. The sun is by far the most abundant source of energy as more energy from the sun strikes the earth in just one hour than is presently consumed in one year. Impressively, covering 0.1% of the Earth's surface with solar cells with an efficiency of 10% would satisfy present energy needs.[10,11] Unfortunately due to the intermittent and diurnal nature of sunlight, in order to make solar–energy as a viable resource requires capture, conversion, and storage.
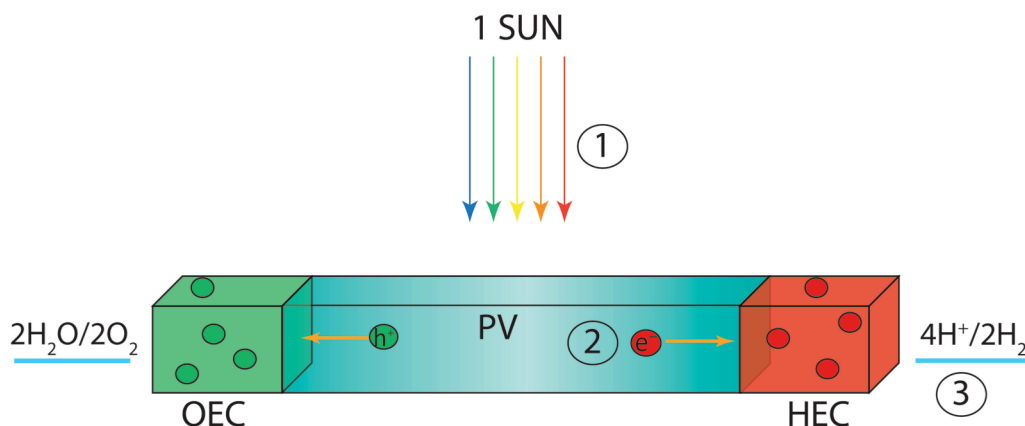
Figure 1.1 Schematic showing (1) solar capture of solar energy by a photovoltaic device, (2) conversion of solar photons into a wireless current, and (3) storage via breaking the bonds of H_2O to make H_2 which can be used as a fuel. Adapted from ref. 5.

1.3 Capture of solar power and conversion to electrical power

An elegant technological approach to directly convert sunlight into electricity without moving parts or environmental emissions is to utilize semiconductors. Semiconductors take advantage of the fact that photons with energy equal to the optical band–gap (similar to HOMO–LUMO transition for molecules) can create an electron–hole pair that can be separated between two different materials, thus effectively establishing a potential difference across the interface. However, since semiconductors are transparent to photons below the band–gap and photons having energies much higher than the band gap rapidly release heat to the lattice of the solid the upper bound conversion efficiency of solar power input to electric power output of a single–absorber is 32% based on a semiconductor with a band–gap of 1.4 eV. [12]
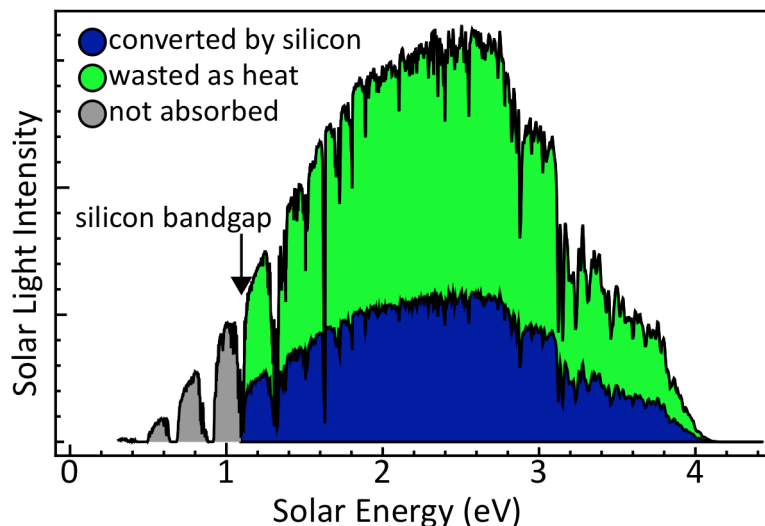
Figure 1.2 Solar irradiance at the surface of the Earth. The band–gap of silicon is overlaid as an example showing that photons absorbed at the band–gap can be converted and those absorbed above the band–gap are wasted as heat.

After photogenerated electrons and holes are created, an electric field is required to separate charges such that they can be transferred to an external load. An electric field can be established by interfacing a semiconductor with another material containing a different work function (also called Fermi level, electron affinity). This can include a metal, another semiconductor, doping two sides of the same semiconductor, or an electrolyte containing a redox couple. Once interfaced, charge transfer between the two materials occurs until equilibrium is established. This produces a region in each material that is depleted of majority charge carriers (electrons for an n–type semiconductor and holes for a p–type semiconductor), which is depicted as band–bending within the semiconductor (upward for n–type, downward for p–type). This translates to a built in potential due the electric field formed at the junction. Upon illumination, a non–equilibrium concentration of photogenerated electrons and holes disturb the previously established equilibrium formed at the interface and the electric field serves to separate the photogenerated electrons and holes such that they can be extracted to do electrical work. The electrical power generated could be used directly. However due to the intermittent nature of sunlight, it is also important to store the electrical power generated in a fuel.

1.4 Conversion of electrical power into fuels

The best–known example of converting solar energy and storing it as chemical energy can be found in nature. Photosynthetic organisms capture sunlight and convert water and carbon dioxide into oxygen and reduced organic species, which can be used as fuels. Fuels are a particularly attractive modality for storage

due to the high energy density the chemical bond. The primary steps in photosynthesis are absorption of solar energy by chlorophyll and other pigments, after which the photogenerated electrons and holes are separated in the Photosystem II (PSII) reaction center. The oxidative power of the photogenerated holes in PSII are transferred to the oxygen evolving complex to split water, producing molecular oxygen which is released into the atmosphere, as well as protons and electrons which are transferred and consumed in Photosystem I (PSI) to reduce NADP^{+} into NADPH (natures form of hydrogen), which is ultimately used to reduce CO_2 to carbohydrates. Since products from the water–splitting reaction are subsumed in subsequent photosynthetic processes, water–splitting is the most critical step in photosynthesis.[6,13,14]

The thermodynamics of water–splitting can be described by the following oxygen evolution and hydrogen evolution electrochemical half reactions (OER and HER, respectively):

$$2H_2O \rightarrow O_2 + 4H^+ + 4e^- \qquad \text{E}^{\text{o}}_{\text{anode}} = 1.23\text{V} - 0.059(\text{pH}) \text{ vs. NHE} \qquad (1.1)$$

$$4H^+ + 4e^- \rightarrow 2H_2 \qquad \text{E}^{\text{o}}_{\text{cathode}} = 0\text{V} - 0.059(\text{pH}) \text{ vs. NHE} \qquad (1.2)$$
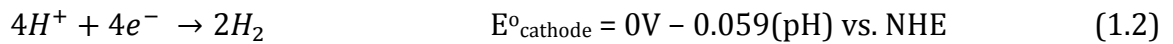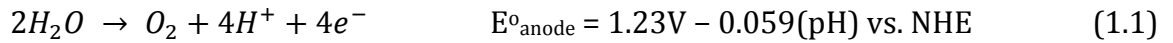
combining equations (1) and (2) indicates that a total voltage of 1.23 V is required to drive the uphill water–splitting reaction. However, additional voltage is necessary to drive the reaction kinetics or rate of the reaction for a given current density (J_{EC}) making the overall voltage for water–splitting (V_{EC}):

$$V_{EC}(J_{EC}) = \eta_{th} + \eta_{OER}(J_{EC}) + \eta_{HER}(J_{EC}) + \eta_R(J_{EC}) \qquad (1.3)$$

where, η_{OER} and η_{HER} are the anodic and cathodic overpotentials, respectively, that

arise from the intrinsic activation barrier for the electrochemical half–reaction

occurring at the electrode–solution interface and η_R accounts for resistive losses

which can arise from resistance through the electrodes, contacts, or mass transport

limitations. Water–splitting catalysts can minimize η_{OER} and η_{HER}. While the impact

of η_R can be minimized through optimal cell designs,[15–17] the activation

overpotentials are intrinsic properties of the catalysts utilized at the anode and

cathode. This overpotential, which is also a metric for catalyst activity, is typically

reported in units of mV decade^{-1}, and is logarithmically related to the current

density (J) as given by the Tafel law[18]:

$$J = b \log \left(\frac{J}{J_o} \right) \qquad (1.4)$$

where b is the Tafel slope and J_0 is the exchange current–density that characterizes

the intrinsic activity of the electrode under equilibrium conditions. In order to

optimize the efficiency for water–splitting, that is the ratio of the thermodynamic

potential for water splitting to the thermodynamic potential, catalysts exhibiting

high J_0 and a low Tafel slopes are necessary.

1.5 Photoelectrochemical water–splitting

The concept of a photoelectrochemical (PEC) device was first popularized by the 1976 paper of Fujishima and Honda. [19] They described immersing a TiO_2 semiconductor in solution, illuminating it with UV light, and observing upon application of a potential bias the evolution of both hydrogen and oxygen. Since this study, hundreds of device–constructs have been investigated as PECS. They can broadly be classified as those that either employ a solution junction (SJ) or buried junction (BJ) for charge separation.[20,21,22] While the physical principles underlying the operation of the methods are quite similar,[21] the position of charge separating interfaces relative to interfaces injecting charge into water redox couples has important consequences for implementation of either method. SJ–PEC operates on the principle that upon submerging a semiconductor in a solution containing a redox couple, charge transfer at the interface will occur provided appropriate alignment between the semiconductor Fermi level (E_F) and the Nernst potential of redox species. The depletion region formed due to band–bending within the semiconductor allows for charge injection into the solution. For the case of water splitting by a SJ–PEC, the quasi–Fermi level for photogenerated electrons or holes must straddle the thermodynamic potential for the water–splitting reaction (i.e. 1.23 V).[23] Due to the previously mentioned kinetic overpotentials the actual voltage required for water–splitting lies between 1.6–2 V. Since the photovoltage generated from a semiconductors is typically at least 0.4 V less than its band–gap,[24] this requires the semiconductor to have a band–gap in excess of 2 V. Therefore, even with proper band–alignment, only a small fraction of the solar spectrum can be

utilized limiting the efficiency to 7%.[23,25] Furthermore, semiconductors are rarely

good water–splitting catalysts.[26] This limitation may be addressed by depositing

water–splitting catalysts on the semi–conductor surface. But surface modification

often affects the efficiency of light absorption and charge separation through the

semiconductor–electrolyte interface (SEI).[27,28] Since charge separation and catalysis

are intimately tied together, optimization of optimization of the individual

components of such a device is challenging and such devices have only

demonstrated solar–to–fuel efficiencies (SFE) of less than 1%.[29]
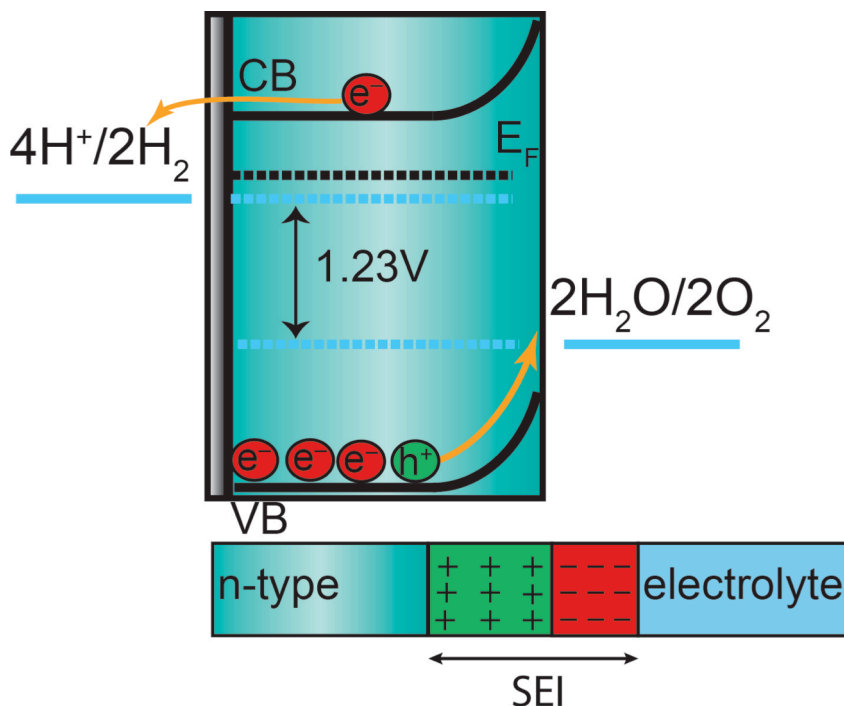
Figure 1.3 Qualitative schematic of an *n*–type semiconductor/electrolyte junction for photoelectrochemical water–splitting.

1.5.1 BJ–PEC requirements

Many of the aforementioned challenges with SJ–PEC can be overcome by

relying on a solid–state semiconductor–semiconductor junction (also referred to as

a buried junction) to perform charge separation. In the BJ–PEC configuration a

solid–state junction is formed either between two semiconductors or by doping two sides of the same semiconductor. By controlling the doping–levels, the width of the depletion region can be optimized for maximum charge separation.[30] Thirty years of ongoing research in the photovoltaic (PV) community has led to doping as a mature technology and optimal charge separation and photovoltage characteristics has been achieved.[31] The buried–junction can be connected to relevant interfaces (e.g. for charge injection to catalysts) through Ohmic contacts, which can be either thin–metal films or conductive oxides deposited on the surface of the semiconductor. Since the semiconductor surface is completely protected from the aqueous environment, semiconductor stability no longer poses a problem. Ultimately, the only requirement is of the BJ–PEC is that an appropriate voltage is supplied to drive the HER and OER conversions.[29]
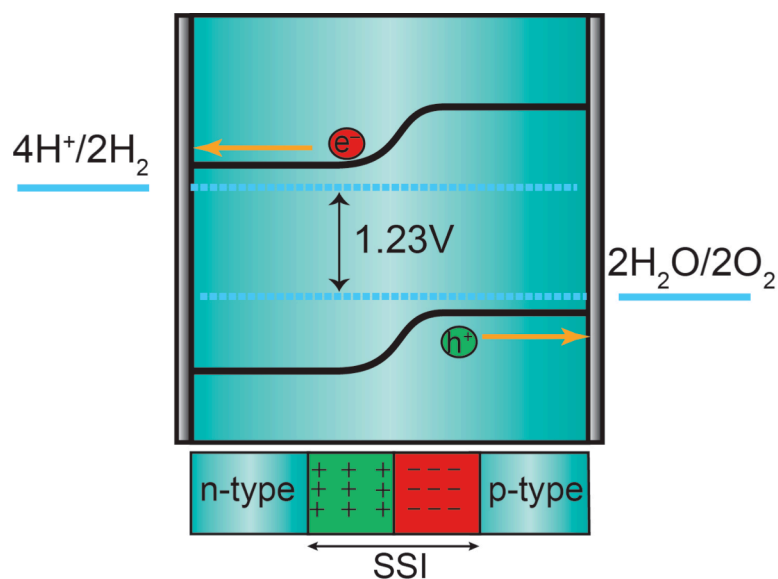
Figure 1.4 Qualitative schematic of a buried semiconductor/electrolyte junction for photoelectrochemical water–splitting.

Furthermore, decoupling the absorption and charge rectification properties from the water–splitting catalysis enables independent optimization of all the required components. The Ohmic contacts can be optimized by choosing highly conductive materials with proper band–alignment to allow facile charge transport.[32,33] Water–splitting catalysts can be independently evaluated and interfaced.

1.5.2 BJ–PEC devices

Many buried junction BJ–PEC devices have been demonstrated in the last 30 years. To date the highest solar–to–fuels efficiency (SFE) devices utilized either expensive multi–junction III–V solar cells,[34,35] low efficiency amorphous silicon (a–Si) solar cells,[35-38] and most recently copper indium gallium diselenide (CIGS) solar cells.[39,40] In all cases the integrated BJ–PEC device suffered from either low SFE,[36-38] and/or were composed of expensive PV materials, expensive catalysts, and operated in strongly acidic or basic electrolytes hindering long–term stability.[34,35,39,40] For these reasons, none of these devices were realistic for economic viability. In order to make this technology realistic from both a cost and stability perspective, low–cost high efficiency PV materials and high efficiency earth–abundant catalyst that operate in benign aqueous environments are necessary.

1.6 Crystalline Silicon

Silicon is prime candidate material for buried–junction devices owing to its almost optimal band–gap of 1.1 eV which absorbs a large fraction of the solar spectrum and it is the second most abundant material on the planet. Additionally

silicon solar cells and modules are one of the most mature technologies developed for solar capture and conversion.[31] Currently, the record solar conversion efficiency for c–Si solar cells has hit 25%, which is quite impressive considering the thermodynamic limit of 29%.[31,41,42] Traditionally silicon PV's have been thought to be too expensive.[11,13,43,44] However, after 30 years of optimization the price of silicon solar cells has declined and the conversion efficiency has improved. [31,41,45] From 2004–2008 crystalline silicon (c–Si) PV modules remained steady at \$3.5–\$4 per peak watt (W_P^{-1}). However, due to the price decrease in polycrystalline silicon, which is used a feedstock material for c–Si, in 2008 the price decreased by half and in 2011 fell below \$1 W_p^{-1}.[41–47] In order to be cost competitive with current the baseload fossil fuel electrical utility plants in the US without subsidies the price
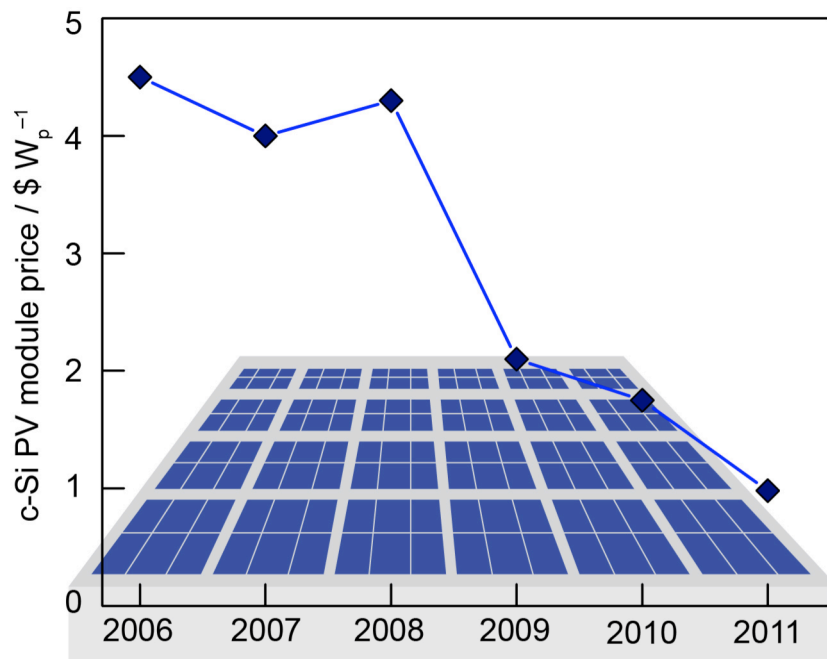
Figure 1.5 Chinese c–Si PV module prices since 2006. The data was adapted from ref. 43.

needs to further decrease to \$0.5–0.75 W_P^{-1}. Modeling and outlined pathways show

that this goal should be achievable by the year 2020.[47,48] However, even the current

status of c–Si PV's has made them a cost–competitive technology with the current

resources used in developing nations such as Africa, the Persian Gulf, and India.[45]

1.7 Earth–abundant water–splitting catalysts

Traditionally catalysts for water–splitting include rare earth elements of

noble metals including Pt, Ir, Ru.[49-51] Our labs changed the paradigm by discovering

active catalysts composed of Earth–abundant materials. Oxidation of Co^{2+} salts in

buffered solutions yield a cobalt–oxide water–oxidation catalyst self–assembles

onto conductive substrates.[52,53] This technique has been extended to other earth–

abundant metals such as Ni and Mn.[54-56] These catalyst are stable by virtue of a self–

healing mechanism,[57-60] and they operate under a variety of pH ranges,[55,56,61,62] and

in the presence of impurities. [61,62] Additionally, it has been shown that these

catalysts can be easily interfaced with semiconductors[63-68] and specifically with

buried–junction silicon PV's.[36,69-71] Since these OER catalysts operate under a variety

of pH neutral conditions, the choice of catalyst for the hydrogen evolution reaction

(HER) has not required platinum.[36,72] Specifically, NiMo(Zn) alloys for hydrogen

evolution, which also self–assemble onto conductive substrates from an aqueous

solution containing Ni^{2+}, sodium molybdate and anhydrous zinc chloride in the

presence of pyrophosphate, bicarbonate, and hydrazine. Subsequent leaching in

base produces a high surface area material.[73] Theses alloys are able to achieve

current densities of 700 mA cm^{-2} at 100 mV overpotential and, with continued

leaching, can attain activities as high as at 1000 mA cm^{-2} at an overpotential of 35 mV. [72,74]
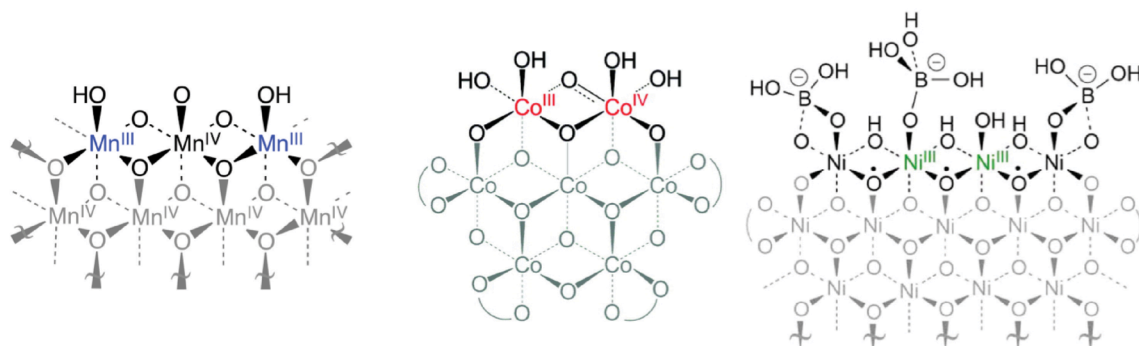
Figure 1.6 Depictions of the molecular structure of our Mn, Co, and Ni water–oxidation catalysts. Reprinted with permission from Mike Huynh.

1.8 Overview

The following chapters of the thesis will discuss the interfacing of water–splitting catalysts with c–Si photovoltaics to produce BJ–PEC devices using a completely modular approach. Chapter 2 focuses on directly depositing OER catalysts onto single–junction c–Si PV's to create a light–assisted photoanode. Of particular importance is the ability to protect silicon from the oxidizing conditions required for water–splitting with a protective interface. Fabrication of these silicon photoanodes requires optimization of two interfaces: a silicon–protective layer interface and a protective layer catalyst interface. Optimization of both lead to a lower overpotential (as determined by Tafel analysis) required for OER.

Since a single–junction c–Si solar cell does not supply the voltage required to achieve water–splitting without the use of an external potential bias, in order to realize a stand–alone water–splitting device based on c–Si, multiple single–junction

c–Si solar cells need to be connected in series. Given that the technical aspects of device integration can be quite challenging, it is beneficial to predict the behavior of a coupled photovoltaic–electrochemical device (PV–EC). In Chapter 3, steady–state equivalent–circuit analysis of a PV based on a string of single–junction c–Si solar cells driving an electrochemical load based on the OER–catalysts developed in our lab allows us to predict the coupled behavior between the PV and EC components. Importantly this allows us to observe the impact solar–to–fuel efficiency based on parameters such as choice of catalysts as well as resistive losses.

Guided by modeling and simulation, a modular PV–EC device is presented in Chapter 4 that is constructed from c–Si and non–precious catalysts. A 10% solar–to–fuels efficiency is demonstrated. This chapter illustrates how a modular approach allows for independent characterization of each component.

The final chapter discusses future directions for the improved design of buried–junction devices for solar–to–fuel conversion. Concepts are presented for improving PV–EC design integration and minimizing cell resistances. Utilization of alternative photovoltaic materials is presented such as perovskite solar cells, which in only the last 5 years have immerged as a cheap PV material with efficiencies competitive with c–Si. [75,76] Additionally, in order to facilitate the interfacing of water–splitting catalysts with PV materials, a brief overview and preliminary results are presented that establish the potential of vapor–deposition techniques to provide an alternate route to deposit OER-catalysts.

1. 9 Conclusion

Direct solar–to–fuel conversion has been identified as a "holy grail" of science.[13] However, a commitment to solution–based PECs over the last 50 years has impeded progress and few water–splitting devices demonstrating the necessary efficiencies have been conceived. The following chapters will highlight how utilizing a modular approach to design buried junction devices allows for independent characterization, optimization, and choice of all components, with the eventual goal of creating a highly efficient stand–alone water–splitting device composed of all non–precious technology ready materials.

1.10 References.

1. Energy Information Administration (200514) *Annual Energy Outlook* (US Dept. of Energy, Washington DC.)

2. Lee R (2011) The outlook for population growth. *Science* **333**, 569–573.

3. United Nations department of Economic and Social Affairs (2013) *World Population prospects: The 2012 Revision*. (United Nations, New York).

4. Holdren JP (2008) Science and Technology for Sustainable Well–Being. *Science* **319**, 424–434.

5. Lewis NS, Nocera DG (2006) Powering the planet: chemical challenges in solar energy utilization. *Proc. Natl. Acad. Sci.* **103**, 15729–15735.

6. Thomas JM (2014) Reflections on the topic of solar fuels. *Energy Environ. Sci.* **7**, 19–20.

7. Peters GP, Andrew RM, Boden T, Canadell JG, Cias P, Le Quéré C, Marland G, Raupach MR, Wilson C (2013) The challenge to keep global warming below 2 °C. *Nat. Clim. Change* **3**, 4–6.

8. Barber J (2006) Photosynthetic energy conversion: natural and artificial. *Chem. Soc. Rev.* **38**, 15729–15735.

9. United Nations Development Program (2000) World *Energy Assessment: Energy and the Challenge of Sustainability.* (United Nations, New York).

10. Grätzel M (2001) Photoelectrochemical cells. *Nature* **414**, 338–344.

11. Grätzel M (2007) Photovoltaic and photoelectrochemical conversion of solar energy. *Philos. Trans. R. Soc. Math. Phys. Eng. Sci.* **365**, 993–1005.

12. Nozik AJ, Miller J (2010) Introduction to solar photon conversion. *Chem. Rev.* **110**, 6443–6445.

13. Bard AJ, Fox MA (1995) Artificial photosynthesis: solar splitting of water to hydrogen and oxygen. *Acc. Chem. Res.* **28**, 141–145.

14. Blankenship RE, Tiede DM, Barber J, Brudvig GW, Ghiradi M, Gunner MR, Junge W, Kramer DM, Melis A, Moore TA, Moser CC, Nocera DG, Nozik AJ, Ort DR, Parson WW, Prince RC, Sayre RT (2011) Comparing photosynthetic and

photovoltaic efficiencies and recognizing the potential for improvement. *Science* **332**, 805–809.

15.   Haussener S, Xiang X, Spurgeon JM, Ardo S, Lewis NS, Weber AZ (2012). Modeling, simulation, and design criteria for photoelectrochemical water–splitting. *Energy Environ. Sci.* **5**, 9922–9935.

16.   Modestino MA, Walczak KA, Berger A, Evans CM, Newman JA, Ager JW, Segalman RA (2013) Robust production of purified H_2 in a stable, self–regulating, and continuously operating solar fuel generator. *Energy Environ. Sci.* **7**, 297–301.

17.   Newman J (2013) Scaling with ohm's law; wired vs. wireless photoelectrochemical Cells. *J. Electrochem. Soc.* **160**, F309–F311.

18.   Bard AJ (2000) *Electrochemical Methods: Fundamentals and Applications*. (Wiley, 2000).

19.   Fujishima A, Honda K (1972) Electrochemical photolysis of water at a semiconductor electrode. *Nature* **238**, 37–38.

20.   Surendranath Y, Bediako DK, Nocera DG (2012) Interplay of oxygen–evolution kinetics and photovoltaic power curves on the construction of artificial leaves. *Proc. Natl. Acad. Sci.* **109**, 15617–15621.

21.   Jacobsson JT, Fjällström V, Edoff M, Edvinsson T (2014) Sustainable solar hydrogen production: from photoelectrochemical cells to PV–electrolysis and back again. *Energy Environ. Sci.* **7**, 2056–2070.

22.   Conibeer GJ, Richards BS (2007) A comparison of PV/electrolyzer and photoelectrolytic technologies for use in solar to hydrogen energy storage systems *Int. J. Hydrog. Energy* **32**, 2703–2711.

23.   Weber MF, Dignam MJ (1986) Splitting water with semiconducting photoelectrodes—efficiency considerations. *Int. J. Hydrog. Energy* **11**, 225–232.

24.   Lewis NS (2005) Chemical control of charge transfer and recombination at semiconductor photoelectrode surfaces. *Inorg. Chem.* **44**, 6900–6911.

25.   Weber MF, Mamiche–Afara S, Dignam MJ, Pataki L, Venter RD (1987) Sputtered fuel cell electrodes. *J. Electrochem. Soc.* **134**, 1416–1419.

26. Gerischer H (1977) On the stability of semiconductor electrodes against photodecomposition. *J. Electroanal. Chem. Interfacial Electrochem.* **82**, 133–143.

27. Zhong DK, Choi S, Gamelin DR (2011) Near–complete supporession of surface recombination in solar photoelectrolysis by "Co–Pi" catalyst–modified W:BiO$_4$. *J. Am. Chem. Soc.* **133**, 18370–18377.

28. Lin F, Boettcher SW (2013) Adaptive semiconductor / electrocatalyst junctions in water–splitting photoanodes. *Nature Mat.* **13**, 81–86.

29. Walter MG *et al.* (2010) Solar water splitting cells. *Chem Rev* **110,** 6446–6473.

30. Nelson J. *The Physics of Solar Cells.* (Imperial College Press, 2003).

31. Green, MA (2009) The path to 25% silicon solar cell efficiency: history of silicon cell evolution. *Prog. Photovolt. Res. Appl.* **17,** 183–189.

32. Gordon RG (2000) Criteria for choosing transparent conductors. *MRS Bull.* **25,** 52–57.

33. Beyer W, Hüpkes J, Stiebig H (2007) Transparent conducting oxide films for thin film silicon photovoltaics. *Thin Solid Films* **516,** 147–154.

34. Khaselev O, Turner JA (1998) A monolithic photovoltaic–photoelectrochemical device for hydrogen production via water–splitting. *Science* **280**, 425-427.

35. Khaselev O, Bansal A, Turner JA (2001) High–efficiency integrated multijunction photovoltaic/electrolysis systems for hydrogen production. *Int. J. Hydrog. Energy* **26**, 127–132.

36. Reece SY, Hamel JA, Sung K, Jarvi TD, Esswein AJ, Pijpers JJH, Nocera DG (2011) Wireless solar water splitting using silicon–based semiconductors and earth–abundant catalysts. *Science* **334**, 645–648.

37. Cristino V , Beradi S, Caramori S, Argazzi R, Carli S, Meda L, Tacca A, Bignozzi CA (2013) Efficient solar water oxidation using photovoltaic devices functionalized with earth–abundant oxygen evolving catalysts. *Phys. Chem. Chem. Phys.* **15**, 13083–13092.

38. Rocheleu RE, Miller EL, Misra A (1998) High–efficiency photo–electrochemical hydrogen production using multijunction amorphous silicon photoelectrodes. *Energy Fuels* **12**, 3–10.

39. Jacobsson TJ, Platzer–Björkman C, Edoff M, Edvinsson T (2013) CuInxGa1–xSe$_2$ as an efficient photocathode for solar hydrogen generation. *Int. J. Hydrog. Energy* **38**, 15027–15035.

40. Jacobsson TJ, Fjällström V, Sahlberg M, Edoff M, Edvinsson TA (2013) A Monolithic device for solar water splitting based on series interconnected thin film absorbers reaching over 10% solar–to–hydrogen efficiency. *Energy Environ. Sci.* **6**, 3676–3683.

41. Green MA (2003) Crystalline and thin–film silicon solar cells: state of the art and future potential. *Sol. Energy* **74,** 181–192.

42. Swanson RM (2005) Approaching the 29% limit efficiency of silicon solar cells. in *Conf. Rec. Thirty–First IEEE Photovolt. Spec. Conf.* 889–894 doi:10.1109/PVSC.2005.1488274

43. Lewis NS (2007) Toward cost–effective solar energy use. *Science* **315**, 798–801.

44. Wadia C, Alivisatos AP, Kammen DM (2009) Materials availability expands the opportunity for large–scale photovoltaics deployment. *Environ. Sci. Technol.* **43**, 2072–2077.

45. Bazilian M (2013) Re–considering the economics of photovoltaic power. *Renew. Energy* **53**, 329–338.

46. Chu S, Majumdar A (2012) Opportunities and challenges for sustainable energy future. *Nature* **488**, 294–303.

47. Swanson RM (2012) *Plantary talk at the DOE SunShot grand challenge: Summit and technology Forum.* (US Department of Energy).

48. Powell DM, Winkler MW, Choi HJ, Simmons CB, Berney Needleman D, Buonassisi T (2012) Crystalline silicon photovoltaics: a cost framework for determining technology pathways to reach a baseload electricity costs. *Energy Environ. Sci.* **5**, 5874–5883.

49. Morris ND, Mallouk TE (2002) A high–throughput optical screening method for the optimization of colloidal water oxidation catalyst. *J. Am. Chem. Soc.* **124**, 11114–11121.

50. McCrory CCL, Jung S, Peter JC, Jaramillo TF (2013) Benchmarking heterogenous electrocatalysts for the oxygen evolution reaction. *J. Am. Chem. Soc.* **45**, 16977–16987.

51. McKone JR, Lewis NS, Gray HB (2014) Will solar–driven water–splitting devices see the light of day? *Chem. Of Mater.* **26**, 407–414.

52. Kanan MW, Nocera DG (2008) In situ formation of an oxygen–evolving catalyst in neutral water containing phosphate and Co^{2+}. *Science* **321**, 1072–1075.

53. Kanan MW, Surendrantath Y, Nocera DG (2009) Cobalt–phosphate oxygen–evolving compound. *Chem. Soc. Rev.* **38**, 109–114.

54. Dincă M, Surendranath Y, Nocera, DG (2010) Nickel–borate oxygen–evolving catalyst that functions under benign conditions. *Proc. Natl. Acad. Sci.* **107**, 10337–10341.

55. Bediako DK, Surendranath Y, Nocera DG (2013) Mechanistic studies of the oxygen evolution reaction mediated by a nickel–borate thin film electrocatalyst. *J. Am. Chem. Soc.* **135**, 3662–3674.

56. Huynh M, Bediako DK, Nocera DG (2014) A functionally stable manganese oxide oxygen evolution catalyst in acid. *J. Am. Chem. Soc.* **136**, 6002–6010.

57. Lutterman DA, Surendranath Y, Nocera DG (2009) A self–healing oxygen evolving Catalyst. *J. Am. Chem. Soc.* **131**, 3838–3839.

58. Surendranath Y, Lutterman DA, Liu Y, Nocera DG (2012) Nucleation, growth, and repair of a cobalt–based oxygen evolving catalyst. *J. Am. Chem. Soc.* **134**, 6326–6336.

59. Huynh M, Bediako DK, Liu Y, Nocera DG (2014) Nucleation and growth mechanisms of an electrodeposited manganese oxide oxygen evolution catalyst. *J. Phys. Chem. C* doi:10.1021/jp501768n.

60. Bediako DK, Costentin C, Jones EC, Nocera DG, Savéant JM (2013) Proton–electron transport and transfer in electrocatalytic films. Applications to a cobalt–based O_2–evolution catalyst. *J. Am. Chem. Soc.* **135**, 10492–10502.

61. Surendranath Y, Dincă M, Nocera DG (2009) Electrolyte–dependent electrosynthesis and activity of cobalt–based water oxidation catalysts. *J. Am. Chem. Soc.* **131**, 2615–2620.

62. Esswein AJ, Surendranath Y, Reece SY, Nocera DG (2011) Highly active cobalt phosphate and borate based oxygen evolving catalysts operating in neutral and natural waters. *Energy Environ. Sci.* **4**, 499–504.

63.   Sun J, Zhong DK, Gamelin DR (2010) Composite photoanodes for photoelectrochemical solar water splitting. *Energy Environ. Sci.* **3**, 1252–1261.

64.   Zhong DK, Gamelin DR (2010) Photoelectrochemical water oxidation by cobalt catalyst ('Co–Pi')/α–Fe_2O_3 composite photoanodes: oxygen evolution and resolution of a kinetic bottleneck. *J. Am. Chem. Soc.* **132**, 4202–4207.

65.   Steinmiller EMP, Choi KS (2009) Photochemical deposition of cobalt–based oxygen evolving catalyst on a semiconductor photoanode for solar oxygen production. *Proc. Natl. Acad. Sci.* **106**, 20633–20636.

66.   Seabold JA, Choi KS, (2011) Effect of a cobalt–based oxygen evolution catalyst on the stability and the selectivity of photo–oxidation reactions of a WO_3 photoanode. *Chem. Mater.* **23**, 1105–1112.

67.   Abdi FF, Han L, Smets AHM, Zeman M, Dam B, van de Krol R (2013) Efficient solar water splitting by enhanced charge separation in a bismuth vanadate–silicon tandem photoelectrode. *Nat. Commun.* **4**, 1–7.

68.   Abdi FF, van de Krol R (2012) Nature and light dependence of bulk recombination in Co–Pi–catalyzed $BiVO_4$ photoanodes. *J. Phys. Chem. C* **116**, 9398–9404.

69.   Pijpers JJH, Winkler, MT, Surendranath Y, Buonassisi T, Nocera DG (2011)Light–induced water oxidation at silicon electrodes functionalized with a cobalt oxygen–evolving catalyst. *Proc. Natl. Acad. Sci.* **108**, 10056–10061.

70.   Young ER, Nocera DG, Bulović V (2010) Direct formation of a water oxidation catalyst from thin–film cobalt. *Energy Environ. Sci.* **3**, 1726–1728.

71.   Cox CR , WinklerMT, Pijpers JJH, Buonassisi T, Nocera DG (2012) Interfaces between water splitting catalysts and buried silicon junctions. *Energy Environ. Sci.* **116**, 9398–9404.

72.   Nocera DG (2012) The artificial leaf. *Acc. Chem. Res.* **45**, 767–776.

73.   Conway BE, Bai L (1986) H_2 evolution kinetics at high activity Ni–Mo–Cd electrocoated cathodes and its relation to potential dependence of adsorption of H. *Int. J. Hydrog. Energy* **11**, 533–540.

74.   Reece SY, Esswein AJ, Sung K, Green Z, Nocera, DG (2013) *Compositions, electrodes, methods, and systems for water electrolysis and other electrochemical techniques. US Patent Appl No.* 8361288.

75.   Hodes G, Cahen D (2014) Photovoltaics: perovskite cells roll forward. *Nat. Photon.* **8**, 87-88.

76.   Snaith HJ (2013) Perovskites: the emergence of a new era for low–cost, high–efficiency solar cells. *The Journal of Physical Chemistry Letters.* **4**, 3623–3630.

Chapter 2–Interfaces between crystalline silicon solar cells and water–oxidation catalysts

2.1 Introduction:

The general requirements for direct solar–to–fuels conversion as well as device constructs were described in Chapter 1. However, of the two half–reactions required for water–splitting, the complex nature of the proton coupled electron transfer (PCET) chemistry of the water–oxidation reaction[1-5] requires the largest overpotential (typically around 250–400mV overpotential at 10mA cm^{-2})[6] and thus limits the overall efficiency for solar–water–splitting devices.[7,8] For this reason most of the research and development for creating solar–water–splitting devices has focused on creating photoanodes that are capable of driving the water–oxidation reaction as well as demonstrating stability under the highly oxidizing conditions.[9,10]

The primary focus has been on large band–gap *n*–type metal oxide semiconductors.[9] Large band–gap materials should be able to supply large photovoltages needed as well as remain stable under oxidizing conditions.[11] However, even after decades of research, these metal–oxide photoanodes still face numerous challenges. First since they possess large band–gaps, they absorb very little of the solar spectrum. Second, they are very rarely configured within a buried–junction, so they suffer from all the aforementioned limitations of the solution–junction approach. Additionally, since the water–oxidation reaction requires four hole equivalents, under operating conditions, photogenerated holes accumulate in the space charge layer at the semiconductor–solution interface and recombination competes with water–oxidation.[12-14] Lastly, since the kinetics of the oxygen evolution reaction (OER) are rate limiting, oxygen evolution catalysts (OECs) must be placed on the electrode surface.[15] Surface modification with catalysts can affect

the charge–separation quality; since catalysts typically aren't transparent only thin monolayers can be used otherwise they can hinder light absorption.[16]

Creating a photoanode with a buried–junction configuration can circumvent many of the challenges outlined above. Years of research have led to optimization of doping crystalline semiconductors with smaller band–gaps that absorb a large fraction of the solar spectrum. The focus and technology ready materials consist of group III–V semiconductors (GaAs, GaP), silicon (crystalline or amorphous), or most recently focused on copper indium gallium diselenide (CIGS). Due to the abundance and overwhelming market advantage of silicon discussed in Chapter 1, it seems a prime materials candidate to construct a photoanode for water–oxidation.

Requirements to enable the use of silicon as a photoanode material include the need to overcome the instability of silicon under highly oxidizing conditions[17] as well as to decrease the kinetic limitations for the water–oxidation reaction by interfacing silicon with OECs. It has been known that silicon surfaces can be protected with thin metal films or conductive oxides.[18-23] The function of the protective layer is two–fold: it must protect the silicon surface from oxidation and enable photogenerated carriers to migrate freely from the buried silicon junction to immobilized OECs. In other words, an Ohmic contact has to be established between the PV element and the catalytic sites, allowing for charge transport with minimum voltage drops. This requires optimization of two interfaces, first the silicon–protective layer interface and second the protective layer/catalyst interface. Herein we present a controlled study on silicon photoanode performance as it relates to

interfaces and choice of both the protective layer (ITO, FTO, Ni) and OER catalysts (CoP_i, CoB_i, NiB_i, NiFeO).

2.2 Results

Fig. 2.1 shows a schematic of a single–junction crystalline silicon (c–Si) photoanode used for these studies. It is worth noting that since illumination occurs at the *n*–side, the *p*–side can be coated with a protective layer that is either a transparent conductive oxide (TCO) typically either tin–doped indium oxide (ITO) or fluorine–doped tin oxide (FTO), or an opaque thin metal film. Additionally, since
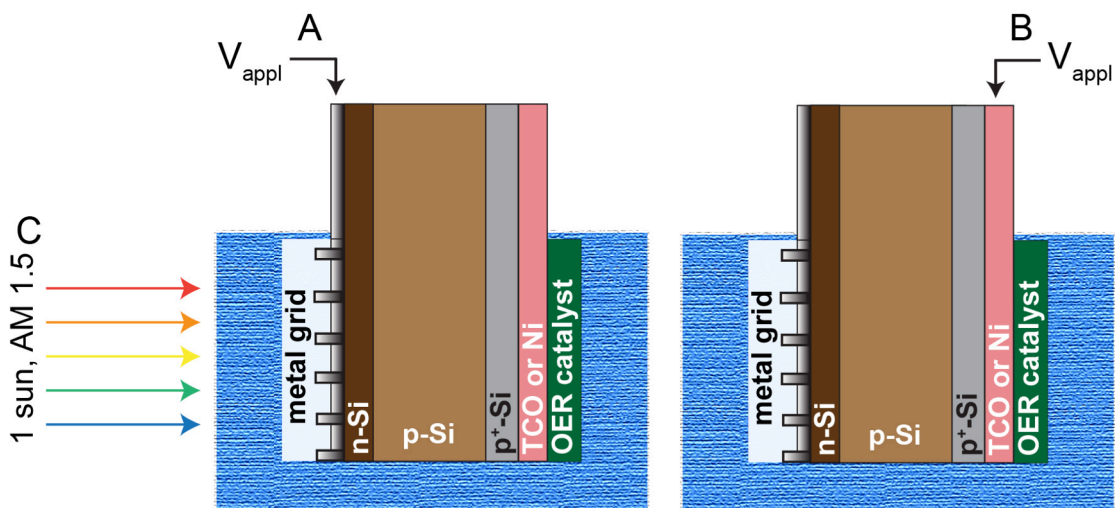
Figure 2.1 Schematic of the OER–catalyst functionalized silicon solar cell used in these studies. For electrochemical measurements, an external voltage may be applied to the contacts at either side of the cell with or without illumination. **A.** The solar cell is operating under reverse bias conditions with voltage applied to the front metal contacts on the *n*–side in the dark. **B.** The voltage can be applied directly to the protective–layer, in which case the PV is bypassed and the current–voltage characteristics are those of the OER–catalyst on an electrode. **C.** The solar–cell is illuminated with AM 1.5 illumination and the current–voltage behavior reflects the activity of the OER–catalyst functionalized solar cell.

the OER catalyst is deposited on the protective material, which is on the *p*–side of the photoanode, there are no limitations as to the thickness of the catalyst layer

since light absorption occurs at the *n*–side. Because the Co–OECs and Ni–OECs developed in our lab are porous in nature, this allows us to deposit thicker films, which contain a larger number of active sites.[24,25] The second more noteworthy detail is the addition of an optional highly doped *p*⁺–Si layer, which was previously demonstrated to be necessary for the Ohmic behavior between the silicon and protective layer interface.[20]
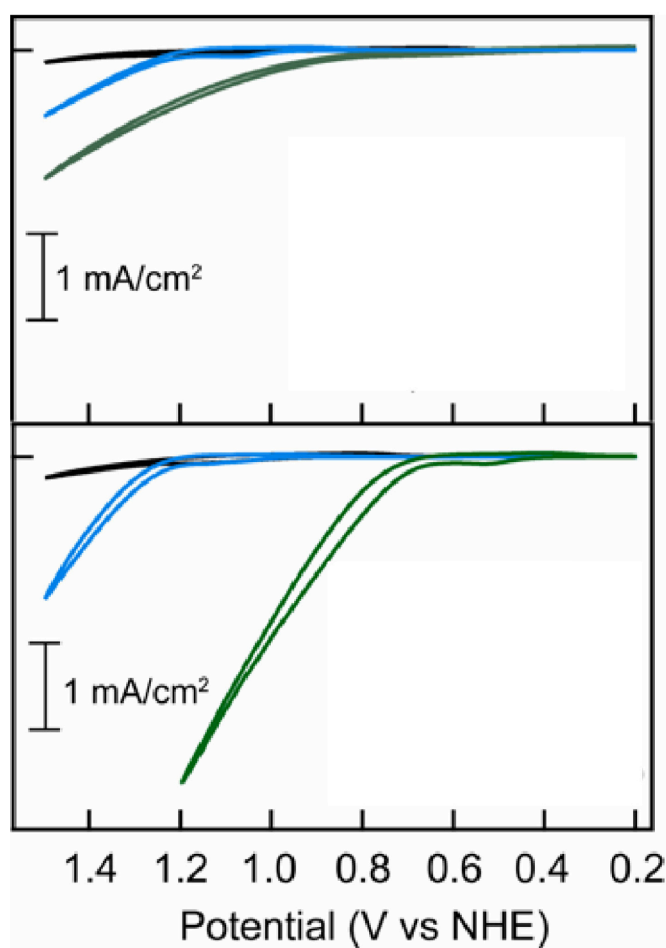
Figure 2.2 CV curves of (top) *np*Si|ITO|CoP$_i$ and (bottom) *npp*⁺Si|ITO|CoP$_i$ in 0.1 M KP$_i$ electrolyte at pH 7 in the dark with V$_{appl}$ through the *n*–side of the cell (——, black), with V$_{appl}$ thought the *n*–side under 1 sun AM 1.5 illumination (——, green) , and in the dark with V$_{appl}$ through the ITO layer bypassing the PV (——, blue). Taken from reference 20.

The importance of the p^+–Si layer is illustrated Fig. 2.2, which shows a shows the cyclic voltammagrams (CV) for a npSi|ITO|CoP$_i$ photoanode and npp^+Si|ITO|CoP$_i$ operating in 0.1 M KP$_i$ electrolyte at pH 7. At pH 7, the thermodynamic potential for water–oxidation is 0.82 V vs. the normal hydrogen electrode (NHE). In the dark, measuring the anodic current by applying the potential across the front metal contacts on the n–side (under reverse bias), the current is negligible as it should be for a high quality PV device.[26] The anodic potential can also be applied between the ITO and catalyst layer. In this case the PV is bypassed and the current–voltage characteristics measured simply reflect the properties of the CoP$_i$ catalyst on an ITO electrode. The CV shows that the onset for water–oxidation occurs at 1.2 V vs. NHE, which is in agreement with the overpotential required to drive the water–oxidation reaction using the CoP$_i$ catalyst on commercial ITO electrodes.[27] When illuminating the photoanode from the n–side with a light intensity of 100mW cm^{-2} (AM 1.5 illumination), the potential onset for water–oxidation has decreased as compared to the measurement where PV–bypassed indicating that some of the photogenerated holes generated in the silicon are injected into the ITO layer, and go on to participate in the water–oxidation reaction with the CoP$_i$ catalyst. However, the increase in current as a function of applied potential exhibits a modest slope after the onset potential. In the absence of an interface oxide, which would render the p–Si|ITO a Schottky–type contact, this interface can be represented with a traditional semiconductor|metal contact band–diagram. As p–Si (E_F = 5.0–5.2 eV)[28] is brought into contact with ITO (E_F = 4.4–4.7 eV),[29,30] which is an n–type semiconductor degenerately doped to the metallic limit, electrons flow from ITO generating a

space–charge layer (up to 1 μm) in *p*–Si that is associated with downward band–

bending (Fig. 2.3A). The relatively low density of acceptors in lightly doped p–Si

yields a large space–charge layer, which in conjunction with downward band–

bending provides a barrier for hole transport (Fig. 2.3B). This barrier can be

mitigated by heavily doping *p*–Si to create a *p+*–layer, which contains a higher

density of acceptors. The resultant reduction in width of the space–charge layer

provides a path for photogenerated holes to tunnel from *p+*–Si into ITO. This

interface can now be considered an Ohmic contact (Fig. 2.3B). Furthermore,

addition of a *p+*–layer introduces a back–surface field, which acts as a barrier for the

migration of photogenerated electrons toward *p+*–Si|ITO interface that could result

in deleterious charge recombination.[26]
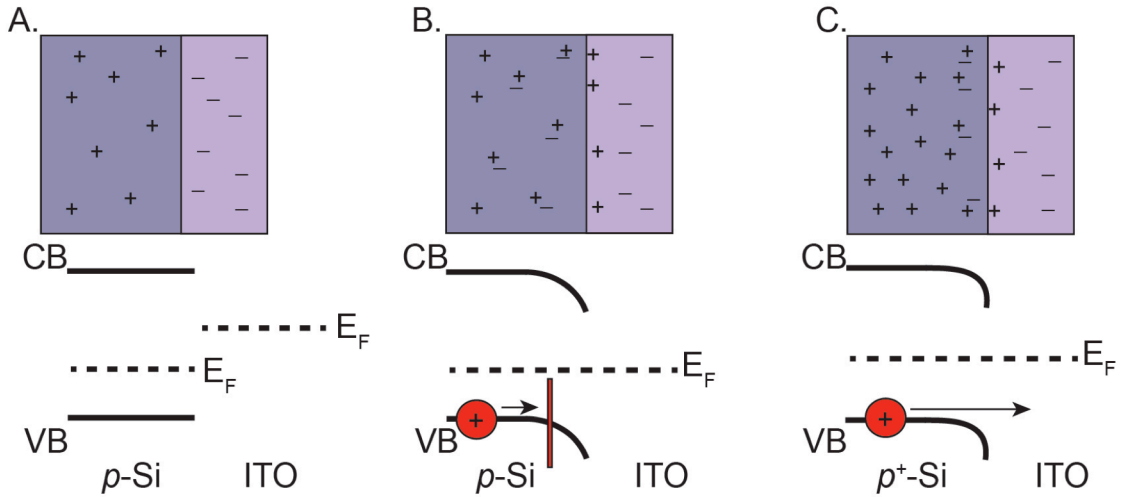
Figure 2.3 Schematic showing the band-diagrams at the *p*–Si|ITO interface. **A.** Before contact. **B**. After equilibration of Fermi levels after interfacing *p*–Si with ITO. **C.** After equilibration of the Fermi levels after interfacing *p+*–Si with ITO.

The effects of *the p+*–layer are exemplified by examining at the CV of the

*npp+*Si|ITO|CoP$_i$ photoanode under illumination in Fig. 2.2B; in contrast to the

*np*Si|ITO|CoP$_i$ the current increases much faster with applied potential. Additionally,

now the difference in the onset potential for water–oxidation between the light and the situation where the PV is bypassed, matches the V_{OC} of the solar cell.

The steady–state performance of the catalyst functionalized silicon solar cells can be evaluated by using Tafel analysis. While Tafel analysis is typically used to determine mechanistic behavior, for the experiments described here, mechanistic information about the OER–catalysts from the Tafel plot is convoluted by the electrical properties of the PV and TCO/Ni components of the anode. Accordingly, the Tafel data is examined solely as a measure of the steady–state activity of the photo–assisted anode as a function of applied potential. Fig. 2.4 shows the Tafel analysis of the npp^+Si|ITO|CoP$_i$ in the dark shows a high slope of 285 mV decade^{-1}, again corresponding to a high quality junction. In the configuration where the PV is
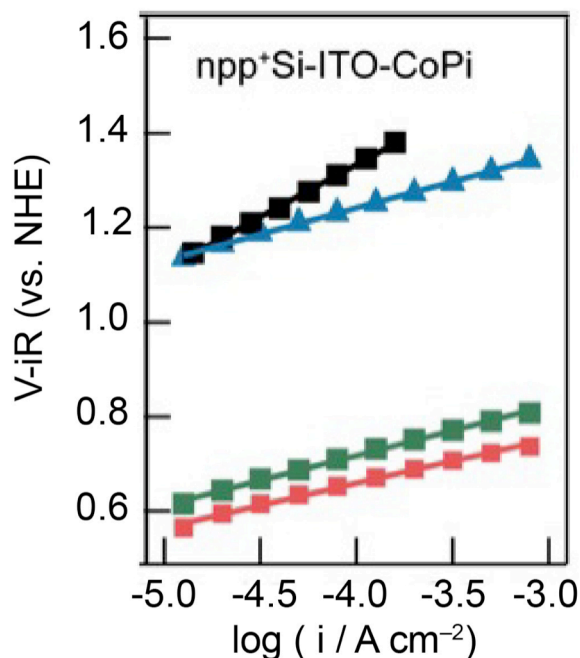
Figure 2.4 Tafel plots for npp^+Si|ITO|CoP$_i$ with potential applied to the metal front contact for measurements in dark (black squares, ■), at 100 mW cm^{-2} (green squares, ■), and 1000 mW cm^{-2} (orange red squares, ■) illumination. The blue triangles (▲) correspond to a measurement in dark where the potential was applied through the ITO film at the back of the sample. Figure taken from ref 20.

bypassed, the slope is significantly lowered 110 mV decade^{-1}. The slope under illumination is identical and the only difference is that the applied voltage for the water–oxidation reaction is decreased by the V_{OC} of the solar cell. This implies that the addition of the p^+–layer allows for optimal conduction from the PV to the catalyst. However, a slope of 110 mV decade^{-1} is still higher than the 60 mV decade^{-1} slope we would expect based on studies of the CoP$_i$ catalyst on commercial ITO electrodes. This indicates that there is hindered conduction across the ITO layer to the OER catalyst.[20]

2.2.1 Optimization of OER–catalyst functionalized silicon solar–cells

The solar cells used in the previous study demonstrated less than optimal performance. The *J–V* curve for generation 1 solar cells displayed J_{SC} = 26.7mA cm^{-2}, V_{OC} = 0.57 V, and fill factors of 0.47 giving PV efficiencies of 7.1%. This limits the electrochemical experiments to ~3 mA cm^{-2}, which is adequate for the purposes of general electrochemical characterization, but with the eventual goal would be to implement these solar cells into a stand–alone water–splitting device improvement is necessary.[20] For generation 2 solar cell, a Si$_3$N$_4$ layer was employed on the *n*–Si surface to act as a passivation layer by tying up dangling bonds and as an anti–reflection coating. Additionally, the front metal contact grid was patterned photolithographically such that both series resistance and shadowing were minimized. The resulting generation 2 solar cells possessed J_{SC} = 28–34 mA cm^{-2}, V_{OC} = 0.5–0.53 V, and fill factors ranging from 0.7–0.77, resulting in PV efficiencies of 10–13%.
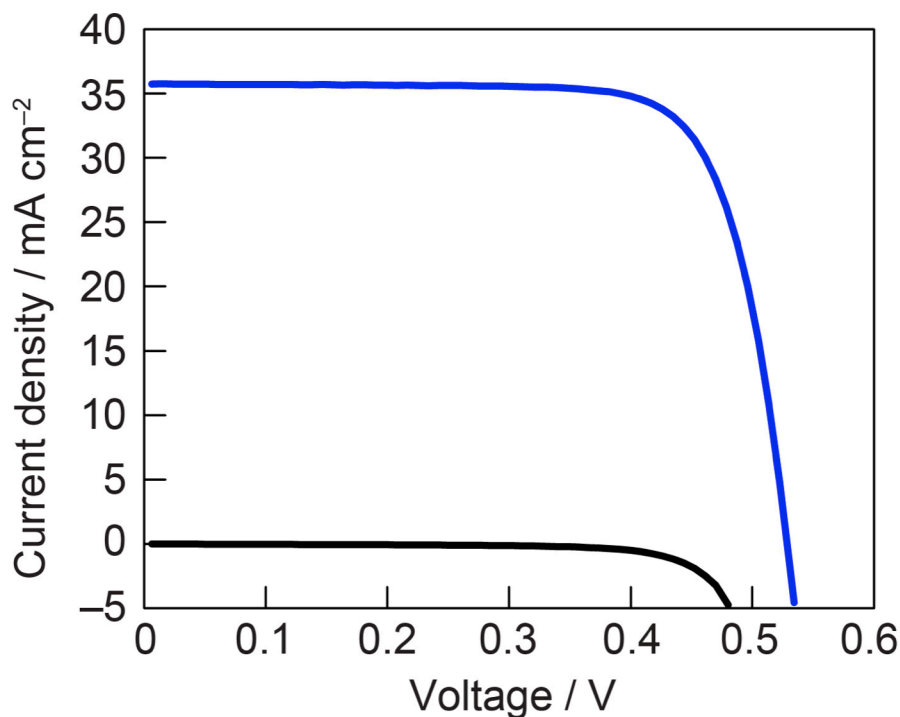
Figure 2.5 Representative *J–V* curve for generation 2 *npp⁺*–Si solar cells used in this study in the dark (━━, black) and under AM 1.5 illumination (━━, blue).

The previous results suggest that the activity of the OER–catalyst functionalized silicon photoanode depends on both intrinsic catalyst activity as well as the protective material used to interface the OER–catalyst with the solar cell. For typical experiments used to isolate the activity of an OER–catalyst, high quality commercial electrodes and precisely controlled deposition conditions are used such that the observed current–voltage behavior is truly indicative of the catalyst's mechanism. However, most fabrication procedures that enable such high quality electrode materials implement high temperature deposition conditions that are detrimental to solar cells. In order to achieve maximal anode activity, it is preferable if the current–voltage behavior closely mimics the intrinsic behavior of the catalyst and the protective material used has little influence over anode activity.

Additionally, since ITO is a rather expensive material, it has been known to show exhibit changes in electrochemical properties at anodic potentials,[31] and poor long–term stability[19] it is preferable to substitute ITO with alternative materials such as FTO or thin metal films. For this reason, a variety of silicon solar cells with various protective–layer/catalyst combinations were examined to establish design principles that need to be considered when interfacing catalysts with silicon solar cells. For example, Fig. 2.6 shows scanning electron micrograph (SEM) images of the CoB_i catalyst deposited on FTO and Ni, respectively. In both cases the morphology of the CoB_i catalyst is similar and comprises a roughened surface that exhibits spherical nodules; the FTO|CoB_i electrode shows larger aggregates of these nodules owing to a longer deposition time to achieve the same amount of charge passed. Since Ni is prone to oxidation at the same potentials required for deposition, the amount of charge passed over a given time period does not correspond to a controlled catalyst thickness, as is the case of an ITO or FTO electrode.
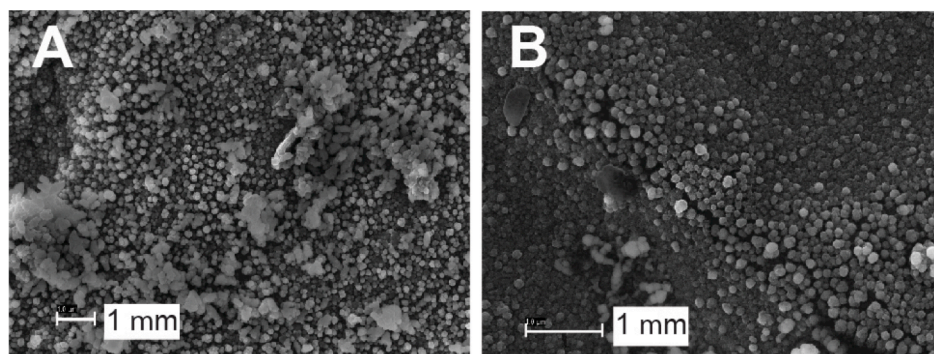
Figure 2.6 Plane view SEM images of OER–catalyts deposited on surface–protected *npp*⁺Si|electrodes. From left to right **A** *npp*⁺|FTO|CoB_i and **B** *npp*⁺Si|Ni|CoB_i.

The oxidation of Ni can be further confirmed by measuring the Faradaic efficiency of the OER–functionalized silicon electrode, which allows us to assess the extent to which the current produced from the cell is consumed in the $4e^-–4H^+$

water–oxidation process to O_2.
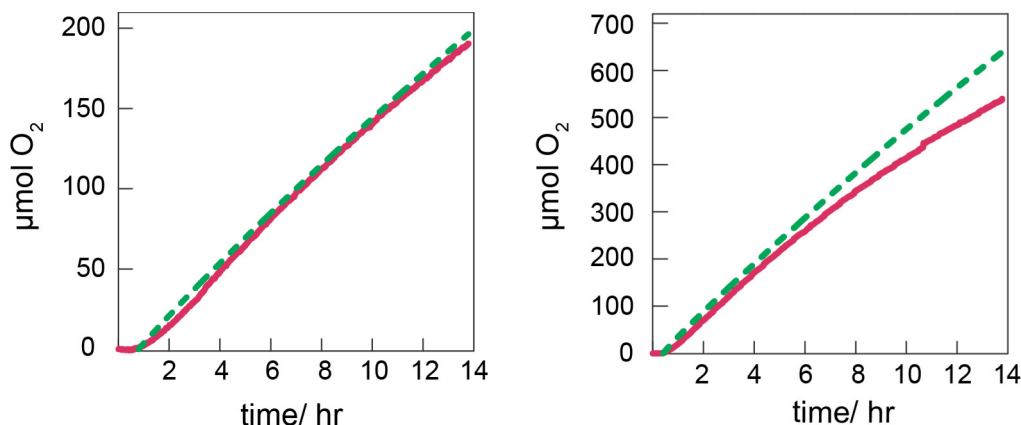
Figure 2.7 O_2 production measured by a fluorescent sensor (▬, red) and the amount produced based on current passed assuming 100% Faradaic efficiency (▬, green) for **(left)** npp^+–Si|FTO|CoB$_i$ and **(right)** npp^+–Si|Ni|CoB$_i$.

Fig. 2.7 shows a comparison between Ni and FTO passivated solar cells, both

functionalized with the CoB$_i$ catalyst. The Faradaic efficiency of a FTO–protected

electrode is unity whereas that of the Ni protective coating is ca. 80%.

Fig. 2.8 shows representative Tafel plots for a CoB$_i$–functionalized solar cell

with the three different interfaces materials ITO, FTO, and Ni. Consistent with

previous results, in all cases, the onset for water oxidation is shifted negatively by

0.5 V at any applied overpotential, thus indicating that the photovoltage of the solar

cell is efficiently harnessed for solar–to–fuel conversion. Despite the similar voltage

offset, different Tafel slopes are observed for the three systems. The remaining

variation in the slopes of the blue and red dots can be fully attributed to different

electrical resistances across the protective layer/catalyst interface, since the

composition of the protective layer is the only parameter that is varied between Fig.

2.8 a–c. The Tafel slopes presented in Fig. 2.8 embody the behavior of the inherent

activity and interfacial resistance.
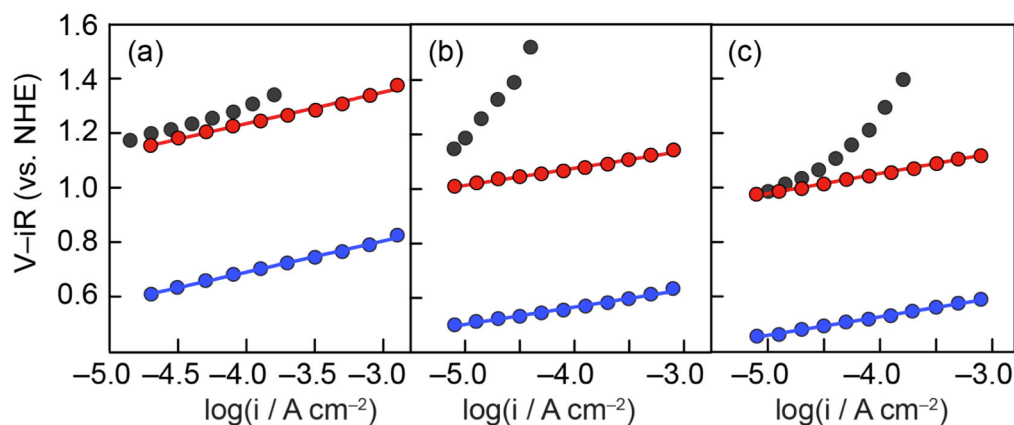
Figure 2.8 Tafel plots of (a) *npp⁺*Si|ITO|CoB$_i$ (b) *npp⁺*Si|FTO|CoB$_i$ and (c) *npp⁺*Si|Ni|CoB$_i$. With the potential applied to the metal front contact for measurements in the dark (●), under 1 sun AM 1.5 illumination (●), and in the dark with the potential applied through the protective coating at the back of the sample (●).

Resistive losses at this interface will reduce the activity of the electrode, since the resulting voltage drop results in an effective lower potential available for OER catalysis. Other OER–catalysts such as NiB$_i$ and NiFeO were also employed in order to observe the influence of catalysts with better activity than the CoB$_i$. For example, The CoB$_i$ and NiB$_i$ catalysts have intrinsic Tafel slopes of 60 and 30 mV decade^{-1}, respectively, arising from a one– electron and two–electron pre–equilibrium prior to a chemical rate–determining step.[27,32,33] For the case of NiFeO, the Tafel slope is known to exhibit variance in the rate–limiting step depending on the Fe content, but is generally reported to be 45 mV decade^{-1}.[34–36]

The Tafel slopes for the various systems are summarized in shown in Graph 2.1 and in all cases the overall Tafel slope exceeds the intrinsic Tafel slopes of the catalysts, thus indicating that there is a series resistance resulting from the interface. Metal interfaces are known to make very good Ohmic contacts[18] whereas the electrical properties of the TCO's depends strongly on the deposition conditions

of the TCO.[18,37,38] It should be noted that for these studies the electrical and quality

of the interface materials used were based on ease of fabrication and deposition

conditions that were non–detrimental to solar cell operation as opposed utilizing

high temperature commercial deposition techniques such as atomic–layer

deposition or chemical vapor deposition (ALD and CVD, respectively), which

produce more uniform, high quality materials. For example, the sheet resistance of

the protective coating used varied for different materials. The resistance of

sputtered Ni was measured to be very low (13 Ω sq^{-1}). But the sheet resistance of

the FTO, as measured in a four–point probe measurement on an FTO deposited on

glass, was found to be 41 Ω sq^{-1}. For commercial FTO on glass (prepared by CVD at

600 ^{o}C), the sheet resistance is 7 Ω sq^{-1}. Using profilometry, we determined that our

sprayed FTO had a thickness of 400 nm, so the voltage drop due to resistive losses

within such a thin FTO and/or ITO are presumably not very large. However, we

cannot exclude the presence of local inhomogeneities in the FTO/ITO that could

potentially lead to local voltage drops.

2.3 Discussion

The different Tafel slopes shown in Fig. 2.8 and shown in Graph 2.1 depend

both on catalytic activity and Ohmic resistances arising primarily between the

catalyst|Si interface, and the variability in the data can be explained by one or a

combination of the above explanations. To isolate the latter, we examined the anode

activity of a variety of catalyst–protective coating combinations on the Si buried

junction. For a given OER catalyst, the trend is the same. The Tafel slope for a FTO–coated electrode is lower than that of ITO, and Ni–coated electrodes exhibit high variability.
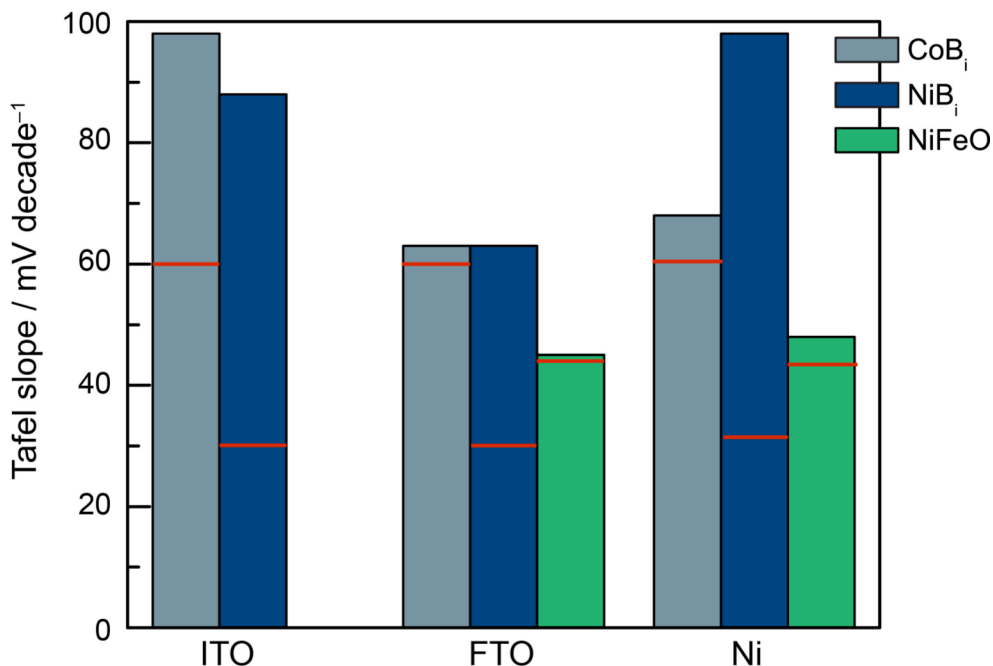
Figure 2.9 Graph showing the variability in Tafel slope for various combinations of OER–catalyst functionalized c–Si solar cells. The red lines indicate the value based on previously reported Tafel analysis.

We believe that the variance of the Ni interface arises from oxidation of the Ni to NiO.[39] The attenuated Faradaic efficiency of the Ni–coated electrode supports this contention inasmuch as some current would be appropriated for the oxidation of Ni to NiO. We note that formation of a NiO layer does not need to be detrimental to the overall OER process since NiO is known to be conductive and hence will not necessarily impair hole transport from the buried junction.[22,40] This suggests that Tafel slopes do not always just reflect Ohmic resistances but that the current does not necessarily translate to water splitting as indicated by Fig. 2.7. It is conceivable

that during oxidation of Ni to NiO, the contact of the protective Si surface changes,

leading to inhomogeneous interfacial properties and changes in anode activity, as

we observed. We show in Table 1 that the consequences of Ni oxidation may be

mitigated by using a more dense catalyst such as NiFeO (Faradaic efficiency of 92%).

Table 2.1 Summary of Faradaic efficiencies for

npp^+–Si | interface | catalyst films.

Electrode	Faradaic Efficiency (%)
npp^+Si|ITO|CoB$_i$	100
npp^+Si|ITO|NiB$_i$	100
npp^+Si|FTO|CoB$_i$	100
npp^+Si|FTO|NiB$_i$	100
npp^+|Si|FTO|NiFeO	100
npp^+Si|Ni|CoB$_i$	86
npp^+Si|Ni|NiB$_i$	80
npp^+Si|Ni|NiFeO	92

Importantly, recent results in the literature have shown that thin metal films

such as Ni have been deposited on silicon using (using Electron–beam evaporation

or ALD) have demonstrated that they can be used to serve as both a protective

coating and once oxidized, as the OER–catalyst.[22,41] Given the good Ohmic contact

between silicon and Ni or other metal films, such an approach may contribute to

optimization of electrode activity.

2.4 Conclusion

The above demonstrates that the overpotential for water splitting by a

buried–junction photoelectrochemical device (BJ–PEC) can be significantly

improved through optimization of the interface between the Si junction and OER catalyst. Although the conductivity and quality of the interface materials could be improved by optimizing deposition conditions (ALD, CVD etc.), what remains clear is that the materials used to interface semiconductors with water–splitting catalysts influence photoanode activity. Furthermore, the ability to independently characterize and optimize each component of the photoanode highlights the modular approach that can be used with buried–junction devices. While the single–junction solar cells used do not supply enough voltage to split water without the use of an external potential bias, the design principles reported here show that the interface optimization between the silicon solar cell and OER catalyst results in a higher activity photoanode, which can be used to construct a stand–alone water–splitting device.

2.5 Experimental

Solar cell fabrication. Solar cell fabrication generation 1 and 2: For the studies included, two iterations of solar cell fabrication procedures were employed. Boron–doped p–type silicon was commercially purchased (International Wafer Service) and used as a starting material (3'' diameter, 0.3–0.5 mm thick). The resistivity was 3 Ω cm^{-2}, corresponding to a dopant concentration of 5×10^{15} cm^{-3}. Prior to phosphorous diffusion, wafers were cleaned using the RCA process to remove organic and metallic contaminants as described in the *Handbook of Semiconductor Wafer Cleaning Technology* (41). An np–Si junction was created via phosphorus diffusion by heating the substrate in a tube furnace while flowing

phosphoryl chloride (POCl$_3$) in a nitrogen carrier gas at 822 °C for 20 min, followed by 20 min of annealing in an O$_2$–N$_2$ atmosphere at 822 °C. In this configuration, phosphorus diffusion occurs on both sides of the wafer, resulting in an *npn*–wafer. The processing yields an emitter with a sheet resistance between 60–70 Ω square^{-1}. As a result of the high–temperature treatment in air, the surface of the *npn*–wafer was covered with a phosphorus silicate glass surface layer, which was removed by dipping in 10% HF solution. To create the optional *p*$^+$ layer, a 1µm film of aluminum–doped silicon (1% Si) was sputtered onto one side the *npn*–wafer followed by a rapid thermal annealing (RTA) step in N$_2$ at 900 °C. During the RTA step, Al diffuses through the *n*–Si layer and converts it to an *npp*$^+$–Si wafer. For generation 2 solar cells, a Si$_3$N$_4$ layer was employed on the *n*–Si surface as a passivation layer and as an anti–reflection coating layer. The Si$_3$N$_4$ layer was formed in a Tystar furnace by low–pressure chemical vapor deposition using a 3:1 mixture of ammonia and dichlorosiline (pressure =250 mTorr) at 770 °C for 20 min, yielding a 80 nm–thick film with a refractive index of 2.01. Additionally, the grid was optimized for both series resistance and shadowing. Using photolithography seven equally spaced grid lines (width 25 mm) collected current from a 1.10 cm^2 device.

A contact–passivation layer was deposited atop the aluminum contact to isolate it from catalytic processes. Films of indium–tin–oxide (ITO) or Ni were deposited on the *p*$^+$–side of the *npp*$^+$–Si wafer using an AJA International sputtering system (Orion 5). The AJA system is equipped with three 300 W guns, two of which are RF for either conductive or dielectric materials, and one of which is DC for conductive materials only 100 nm thick ITO was reactively sputtered in an 11:1

mixture of Ar:O$_2$. To improve conductivity of the ITO layer[37] the entire silicon wafer was then annealed in a N$_2$ atmosphere at 400 °C for 45 min. Nickel films 100 nm thick were sputtered in a pure Ar environment. In all cases, the pressure was ~4 × 10^{-6} bar and deposition rates of all films were measured using a quartz crystal monitor (QCM) in a preliminary 'conditioning' run. FTO was deposited on the p^+– side of the silicon wafer by spray pyrolysis. In a typical spray deposition, 60 mL of ethanol containing 4.2 g SnCl$_4$•5H$_2$O and 0.7 mL saturated NH$_4$F was used to coat one 3″ diameter wafer with FTO. Before the spray pyrolysis, the silicon wafer was heated to 400 °C in air. After spraying the FTO precursor solution, a transparent film formed on the wafer. This FTO coated wafer was annealed at 400 °C in air for 1 h. Ti/Pd/Ag metal contacts were deposited (20 / 20 / 250 nm, Ti adjacent to Si) on the n–side of the silicon wafer; the residual Al from the formation of the p^+ layer was used to contact the base of the PV device. Following metallization, the 3″ diameter wafer was cut into 1.5 × 2.5 cm^2 pieces using a 1064 nm YAG laser cutter.

Electrochemical Methods. Electrochemical experiments were performed using a CH Instruments 760D potentiostat and an Ag/AgCl reference electrode (BASi, MF–2052). All electrode potentials were converted to the NHE scale using E(NHE) = E(Ag/AgCl) + 0.197. Platinum mesh (Alfa Aesar) was used as the auxiliary electrode. Unless otherwise stated, the electrolyte was 0.5 M potassium borate (B$_i$) at a pH of 9.2 with 1.5 M KNO$_3$ as a supporting electrolyte.

Catalyst Film Preparation. Catalyst films were deposited on completed PV– devices that included a contact–passivation layer. Catalyst films of CoB$_i$ and NiB$_i$

electrodeposited in a two–compartment electrochemical cell with a glass frit junction of fine porosity. The working compartment was charged with ~50 mL of solution of 25 mL of 0.2 M B_i electrolyte and 25 mL of 1 mM Co^{2+} or Ni^{2+} solution. The auxiliary compartment was charged with ~50 mL of 0.1 M B_i electrolyte. The working electrode was a 1.5 × 2.5 cm^2 piece of *npp*+–silicon solar cell, fabricated as described above. Typically, a 1 cm^2 area of the working electrode was immersed in the solution and electrolysis was carried by applying 0.85 V vs. NHE directly to the TCO/Ni side until 26 mC cm^{-2} of charge had passed for CoB_i deposition, and 2.6 mC cm^{-2} of charge had passed for NiB_i deposition. High–activity NiB_i is achieved by anodizing NiB_i films in 1 M KB_i by passage of 3.5 mA cm^{-2} for 1 h with stirring.[33,42] NiFeO catalyst films were deposited by reactive sputtering using the AJA International sputtering system, mentioned above. Films of 100 nm thickness were deposited by reactive sputtering from an iron–doped nickel sputtering target (19% Fe) in an $Ar:O_2$ atmosphere of 3:1.[34]

Photoelectrochemical Methods. Photoelectrochemistry experiments were performed in a one–compartment quartz cell. The light source was a Sol 2A solar simulator (Newport Corp.).

Tafel Data Collection. The Tafel behavior of surface–passivated, catalyst–functionalized, solar cells was measured in the region of water oxidation over a 200 mV range in 10–30 mV increments. Depending on the whether P_i or B_i analogous of the catalysts were used, measurements were conducted in a solution containing 0.5

M KB_i/KP_i and 1.5 KNO_3 at pH 9.2, using an Ag/AgCl reference electrode and a Pt auxiliary electrode.

O_2 Quantification. An Ocean Optics oxygen sensor system (NeoFox® Phase Measurement System) was used for the quantitative detection of O_2. The experiment was performed in a custom built two–compartment gas–tight electrochemical cell. The electrolyte was a 0.5 M KB_i and 1.5 M KNO_3 solution at pH 9.2; the solution was purged by bubbling with high purity Ar for 2 h with vigorous stirring and it was then transferred to the electrochemical cell under Ar. The two–compartment cell comprised a catalyst–functionalized silicon solar cell working electrode, an Ag/AgCl reference electrode, and a Pt mesh counter–electrode. Measurements of the FOXY probe were recorded at 10 s intervals, and the data was converted into the partial pressure of O_2 in the headspace using a calibration curve defined by air, 20.9% O_2 and high purity N_2 (0% O_2). After recording the partial pressure of O_2 for 2 h in the absence of an applied potential, the sample was illuminated with 1 sun AM 1.5 light and electrolysis was initiated at 0.6 V vs. NHE. Due to variations in the PV characteristics for each samples, a potential bias of 0.6 V produced operating current densities ranging from 1.5–5 mA cm^{-2}. Electrolysis with O_2 sensing was continued for ~12 h. Upon terminating the electrolysis, the O_2 signal was recorded for an additional 2 h to ensure that the O_2 yield reached a plateau. At the conclusion of the experiment, the solution and the headspace volumes in the working compartment were measured (around 55 mL and 62 mL, respectively). The total charge passed in the electrolysis was divided by 4F to get the theoretical O_2 yield. The partial pressure of O_2 was converted into μmols, and corrected for dissolved O_2

in solution using Henry's Law. The total O_2 yields from both the theoretical and the experimental results were used to determine the Faradaic efficiency.

2.6 References:

1. Cukier RI, Nocera DG (1998) Proton–coupled electron transfer. *Annu. Rev. Phys. Chem.* **49**, 337–369.

2. Eisenberg R, Gray, HB (2008) Preface on making oxygen. *Inorg. Chem.* **47**, 1697–1699.

3. Betley, TA *et al.* (2008) A ligand field chemistry of oxygen generation by the oxygen–evolving complex and synthetic active sites. *Philos. Trans. R. Soc. B Biol. Sci.* **363,** 1293–1303.

4. Hammes–Schiffer, S (2009) Theory of proton–coupled electron transfer in energy conversion processes. *Acc. Chem. Res.* **42,** 1881–1889

5. Concepcion JJ *et al.* (2009) Making oxygen with ruthenium complexes. *Acc. Chem. Res.* **42,** 1954–1965.

6. McCrory CCL, Jung S, Peters JC, Jaramillo TF (2013) Benchmarking heterogeneous electrocatalysts for the oxygen evolution reaction. *J. Am. Chem. Soc.* **135**, 16977–16987.

7. Rocheleau RE, Miller EL (1997) Photoelectrochemical production of hydrogen: engineering loss analysis. *Int. J. Hydrog. Energy* **22,** 771–782.

8. Surendranath Y, Bediako, DK, Nocera DG (2012) Interplay of oxygen–evolution kinetics and photovoltaic power curves on the construction of artificial leaves. *Proc. Natl. Acad. Sci.* **109,** 15617–15621.

9. Osterloh FE (2008) Inorganic materials as catalysts for photochemical splitting of water. *Chem. Mater.* **20,** 35–54.

10. Sun J, Zhong DK, Gamelin DR (2010) Composite photoanodes for photoelectrochemical solar water splitting. *Energy Environ. Sci.* **3,** 1252–1261.

11. Gerischer H (1977) On the stability of semiconductor electrodes against photodecomposition. *J. Electroanal. Chem. Interfacial Electrochem.* **82,** 133–143.

12. Zhong DK, Choi S, Gamelin DR (2011) Near–complete suppression of surface recombination in solar photoelectrolysis by 'Co–Pi' catalyst–modified W:BiVO4. *J Am Chem Soc* **133,** 18370–18377.

13. Lewerenz HJ, Peter L (2013) *Photoelectrochemical Water Splitting* (The Royal Society of Chemistry) Available at: http://dx.doi.org/10.1039/9781849737739.

14. Le Formal F *et al.* (2014) Back electron–hole recombination in hematite photoanodes for water splitting. *J. Am. Chem. Soc.* **136,** 2564–2574.

15. Walter MG *et al.* (2010) Solar water splitting cells. *Chem Rev* **110,** 6446–6473 (2010).

16. Fudig L, Boettcher SW (2014) Adaptive semiconductor / electrocatalyst junctions in water–splitting photoanodes. *Nat. Mater.* **13**, 81–86.

17. Zhang XG (2001) *Electrochemistry of Silicon and Its Oxide.* (Springer, New York).

18. Gordon RG (2000) Criteria for choosing transparent conductors. *MRS Bull.* **25,** 52–57.

19. Kelly NA, Gibson TL (2006) Design and characterization of a robust photoelectrochemical device to generate hydrogen using solar water splitting. *Int. J. Hydrog. Energy* **31,** 1658–1673.

20. Pijpers JJH, Winkler MT, Surendranath Y, Buonassisi T, Nocera DG (2011) Light–induced water oxidation at silicon electrodes functionalized with a cobalt oxygen–evolving catalyst. *Proc. Natl. Acad. Sci.* **108,** 10056–10061.

21. Young ER., Nocera DG, Bulović V (2011) Photo–assisted water oxidation with cobalt–based catalyst formed from thin–film cobalt metal on silicon photoanodes. *Energy Environ. Sci.* **3,** 1726–1728.

22. Sun K*et al.* (2012) Nickel oxide functionalized silicon for efficient photo–oxidation of water. *Energy Environ. Sci.* **5**, 7872–7877.

23. Kenney MJ *et al.* (2013) High–performance silicon photoanodes passivated with ultrathin nickel films for water oxidation. *Science* **342,** 836–840.

24. Farrow CL, Bediako DK, Surendranath Y, Nocera DG, Billinge SJL (2013) Intermediate–range structure of self–assembled cobalt–based oxygen–evolving catalyst. *J. Am. Chem. Soc.* **135**, 6403–6406.

25. Bediako DK, CostentinC, Jones EC, Nocera DG, Savéant, JM. (2013) Proton–electron transport and transfer in electrocatalytic films. Application to a cobalt–based O2–evolution catalyst. *J. Am. Chem. Soc.* **135,** 10492–10502.

26.   Nelson J (2003) *The Physics of Solar Cells*. (Imperial College Press,).

27.   Kanan MW, Surendranath Y, Nocera DG (2009) Cobalt–phosphate oxygen–evolving compound. *Chem. Soc. Rev.* **38,** 109.

28.   Novikov A (2010) Experimental measurement of work function in doped silicon surfaces. *Solid–State Electron.* **54,** 8–13.

29.   Park Y, Choong V, Gao Y, Hsieh BR, Tang CW (1996) Work function of indium tin oxide transparent conductor measured by photoelectron spectroscopy. *Appl. Phys. Lett.* **68,** 2699–2701.

30.   Ho JJ, Chen CY, Hsiao RY, Ho OL (2007) The work function improvement on Indium–Tin–Oxide epitaxial layers by doping treatment for organic light–emitting device applications. *J. Phys. Chem. C* **111,** 8372–8376.

31.   Kraft, A., Hennig, H., Herbst, A. & Heckner, K.–H. Changes in electrochemical and photoelectrochemical properties of tin–doped indium oxide layers after strong anodic polarization. *J. Electroanal. Chem.* **365,** 191–196 (1994).

32.   SurendranathY., Kanan MW, Nocera DG (2010) Mechanistic studies of the oxygen evolution reaction by a cobalt–phosphate catalyst at neutral pH. *J. Am. Chem. Soc.* **132,** 16501–16509

33.   Bediako DK, Surendranath Y, Nocera DG (2013) Mechanistic studies of the oxygen evolution reaction mediated by a nickel–borate thin film Electrocatalyst. *J. Am. Chem. Soc.* **135,** 3662–3674.

34.   Miller EL, Rocheleau, RE (1997) Electrochemical behavior of reactively sputtered iron-doped nickel oxide. *J. Electrochem. Soc.* **144,** 3072–3077.

35.   Rocheleau   RE,   Miller   EL,   Misra   A   (1998)   High–efficiency photoelectrochemical hydrogen production using multijunction amorphous silicon photoelectrodes. *Energy Fuels* **12,** 3–10.

36.   Corrigan DA (1987) The catalysis of the oxygen evolution reaction by iron impurities in thin film nickel oxide electrodes. *J. Electrochem. Soc.* **134,** 377–384.

37.   Hennig H, Heckner KH, Hirsch D, Ladwig H (1982) The Influence of the preparation on layer properties of transparent indium–tin oxide electrodes. *Phys. Status Solidi A* **74,** 133–139.

38.   Kurtz SR, Gordon RG (1987) Transparent conducting electrodes on silicon. *Sol. Energy Mater.* **15,** 229–236.

39.   Visscher W, Barendrecht E (1980) The anodic oxidation of nickel in alkaline solution. *Electrochimica Acta* **25,** 651–655.

40.   Carpenter MK, Corrigan DA (1989) Photoelectrochemistry of nickel hydroxide thin films. *J. Electrochem. Soc.* **136,** 1022–1026.

41.   Hu S, Shaner MR, Beardslee JA, Licterman M, Brunschwig BS, Lewis NS (2014) Amorphous TiO2 coatings stabilize Si, GaAs, and GaP photoanodes for efficienct water–oxidation. *Science* **344**, 1005–1009.

42.   Bediako DK *et al.* (2012) Structure–activity correlations in a nickel–borate oxygen evolution catalyst. *J. Am. Chem. Soc.* **134**, 6801–6809.

Chapter 3– Modeling a coupled photovoltaic electrochemical device using steady–state equivalent circuit analysis.

Portions of this chapter have been published:

Winkler MT, Cox CR, Nocera DG, Buonassisi T (2013) Modeling integrated photovoltaic–electrochemical devices using steady–state equivalent circuits. *Proc. Natl. Acad. Sci.* **110**, E1076–E1082.

3.1 Introduction

Direct solar–to–fuels conversion can be achieved by integrating a photovoltaic device with water–splitting catalysts. In Chapter 2, single–junction crystalline silicon (c–Si) solar cells were functionalized with oxygen evolving catalysts (OECs) to construct a photo–assisted device for promoting the water–oxidation reaction. However, single–junction c–Si (V_{OC} = 0.5–0.7 V) does not supply enough voltage for water–splitting (V_{th} = 1.23 V) without the use of an external potential bias. In order to supply the full potential needed for water–splitting based on c–Si solar cells, multiple single–junction c–Si solar cells need to be connected in series. Steady–state equivalent circuit of analysis of a series connected string of single–junction c–Si solar cells, coupled to the electrochemical process of water–splitting allows us to predict the coupled behavior of a PV–EC device. Specifically, for a PV component consisting of a string of series–connected c–Si solar cells, we can predict the number of solar cells needed to produce a 10% or higher steady–state solar–to–fuels efficiency (SFE) based on the choice of water–splitting catalysts as well as assess resistive losses. This is highly beneficial since one of the primary challenges in creating a stand–alone photovoltaic–electrochemical (PV–EC) device is design integration. The ability to predict the coupled PV–EC behavior before undertaking the complicated materials–related integration aspects allows considerable research struggles to be circumvented.

3.2 Efficiency considerations

The steady–state solar–to–fuels efficiency (SFE) of a photovoltaic used to drive and electrochemical load has been described previously[1-7] and is given by:

$$\eta_{SFE} = \eta_{PV} \times \eta_{EC} \times \eta_C \qquad (3.1)$$

where, η_{PV}, η_{EC}, η_C are the efficiencies of the PV device, the EC components (including electrodes and wires), and the efficiency of the coupling between the two.[3,8] The maximum efficiency of a single–absorber solar cell is limited by the solar spectrum. For maximum conversion efficiency to be achieved, a single–absorber solar cell must absorb a large portion of the solar spectrum to generate a large photocurrent with a concomitant large phototvoltage. The latter contradicts the former since in order to generate a large photovoltage a large band–gap is required, which in turn results in the absorption of only a small fraction of the solar spectrum, thus leading to a small photocurrent. Additionally, due to various types of charge recombination mechanisms, typical solar cell performance is usually 300–400 mV lower than the band–gap at room temperature.[4,9]

The actual efficiency of a given solar cell can be determined by examining the current–voltage characteristics of the solar cell under illumination (Fig. 3.1). The open–circuit voltage (V_{OC}) and short–circuit current (J_{SC}) are the maximum voltage and current of the cell, respectively. However, since the V_{OC} occurs when no current is flowing and the J_{SC} occurs where the voltage is zero, the actual maximum power (P_{MAX}) output of the solar cell occurs where the product of voltage and current is the

greatest ($P_{MAX} = V_{MP} \times J_{MP}$) and is referred to as the maximum power–point (MPP). The fill–factor (FF) describes the ratio of the maximum power of the solar cell to the product of V_{OC} and J_{SC}. Therefore, the PV efficiency given at Air Mass (AM) 1.5 spectrum with an incident power density of 100mA cm^{-2}, is then defined by:

$$\eta_{PV} = \frac{FF \times V_{OC} \times J_{SC}}{P_{SUN}}$$

(3.2)

For silicon with a band–gap of 1.1 eV, the upper–bound solar power to electrical power efficiency of 29%.[10,11] At present c–Si solar cells have reached a fabrication maturity such that the a record efficiency of 25% has been achieved[12] technology ready available PV efficiencies are in the 18–20% range with module efficiencies of 14–20%.[13,14]

The additional voltage required to compensate for reaction kinetics, for a given operational current–density, dominates the efficiency of an electrochemical process such as water–splitting. The efficiency for water–splitting is determined by how much voltage is needed to drive the reaction (V_{OP}) as compared to the thermodynamic potential (V_{th}) and is given by:

$$\eta_{EC} = \frac{V_{th}}{V_{OP}}$$

(3.3)

For water–splitting in which the oxygen–evolution reaction occurs at the anode and the hydrogen evolution reaction occurs at the cathode, V_{EC} accounts for

the thermodynamic potential and the overpotential for each half–reaction, as well as cell resistances (η_R) (i.e. resistance through electrodes, contacts, and solution resistance). The total voltage required is:

$$V_{EC}(J_{EC}) = V_{th} + \eta_{OER}(J_{EC}) + \eta_{HER}(J_{EC}) + \eta_R(J_{EC}) \qquad (3.4)$$

where the η_{OER} and η_{HER} are the overpotentials for the oxygen–evolution and hydrogen–evolution reactions (OER and HER) and for a given current–density J_{OP} are given by the Tafel law:

$$V_{OER,HER} = b \log \frac{J_{OP}}{J_o^{OER,HER}} \qquad (3.5)$$

where b is the Tafel slope and J_o is the exchange current density. The overall efficiency for water–splitting is typically limited by complex nature of the proton–coupled electron–transfer (PCET) chemistry of the water–oxidation reaction[15-20] In order to minimize the overpotential catalysts are used to effect the half reactions and different catalysts operate under different mechanisms, which determines the rate for the reaction. For example, mechanistic studies for the Co–OEC's and Ni–OEC's developed in out lab exhibit different Tafel slopes of 30 and 60 mV decade[-1], respectively, which are indicative of a mechanism involving a one versus two–electron reaction that is proceeded by a rate–limiting chemical step for oxygen evolution.[21,22,23] Typically, the relevant figure of merit is the overpotential required

to operate at a current density of 10mA cm^{-2}, which for most OER catalysts requires

an overpotential of 250–400mV.[24,25] Commercial alkane electrolyzes exhibit

efficiencies around 60–75%,[26,27] and given the best water–splitting catalysts

developed in our group a comparable efficiency may be achieved.[28]

The efficiency of coupling between the PV and EC components is not

fundamentally limited by any physical constraint, but is entirely dependent on how

well matched the maximum power output of the PV is to the electrochemical load

for water– splitting. The simplest mode of coupling the PV and EC components is to

perform the anodic half–reaction (OER) on the positive terminal and the cathodic

half reaction (HER) on the negative terminal of the PV–device. This type of coupling
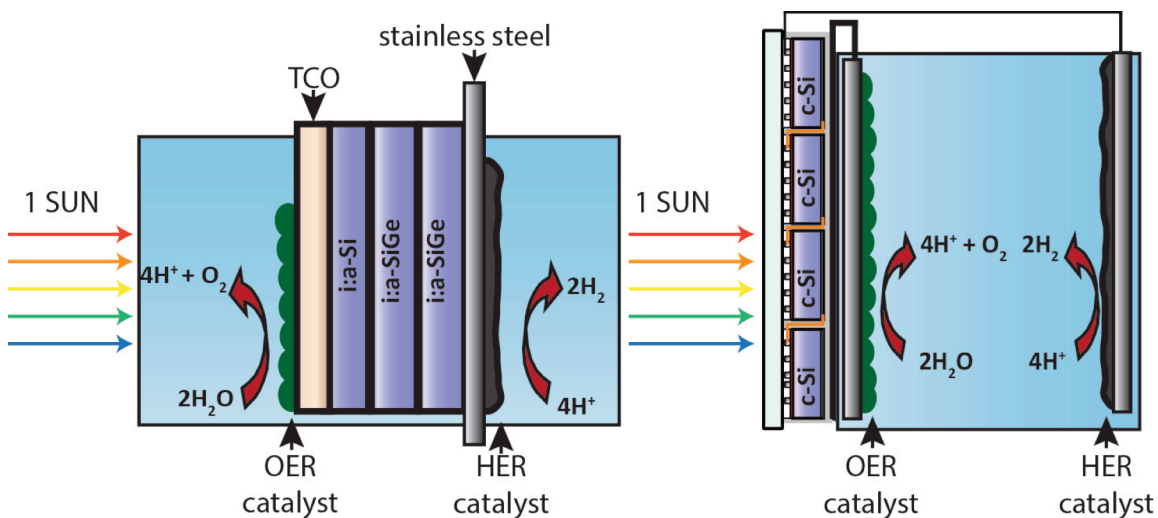
Figure 3.1 Schematic of a wired and wireless PV–EC based on silicon solar cells. Regardless of the mode of coupling between the two, the equivalent circuit is identical.

enforces the two–half reactions to be equipotential with the two terminals of the

PV–device, which is true regardless if the PV is a buried–junction stack or series–

connected single–junction solar cells wired to an anode and cathode (i.e. a wired

and wireless configuration, Fig. 3.1).[9,29] Fig. 3.2 illustrates that this direct electrical

connection is equivalent to constraining the currents and voltages of the PV–EC

system to be identical: $J_{PV} = J_{EC}$ and $V_{PV} = V_{EC}$. The point of intersection (as shown in

Fig. 3.3) between the PV–curve and EC–curve also defines the operational point for a
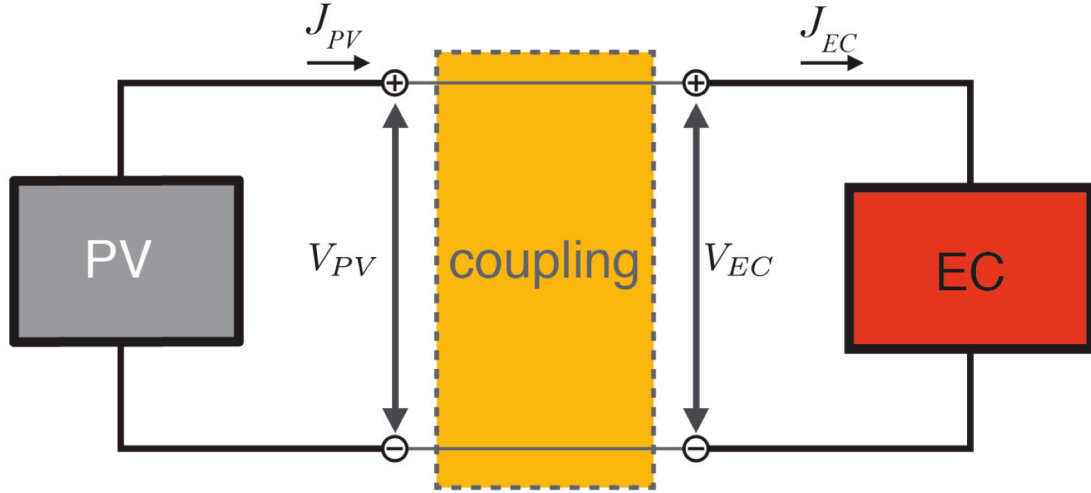
Figure 3.2 Block diagram for a photovoltaic (PV) powered electrochemical cell (EC), where direct electrical connection constrains $J_{PV} = J_{EC}$ and $V_{PV} = V_{EC}$

coupled PV–EC device.[6,7,30] Perfect coupling occurs when the intersection of the PV

and EC curves occurs at the P_{MAX} of the solar cell meaning that the maximum power

output of the PV–component is utilized by the EC–component and is defined by:

$$\eta_C = \frac{V_{OP} \times J_{OP}}{FF \times V_{OC} \times J_{SC}} \tag{3.6}$$

Using the above definitions for η_{PV}, η_{EC}, and η_C of the, equation 3.1 can be re–written

as:

$$\eta_{SFE} = \frac{FF \times V_{OC} \times J_{SC}}{P_{SUN}} \times \frac{V_{th}}{V_{OP}} \times \frac{V_{OP} \times J_{OP}}{FF \times V_{OC} \times J_{SC}} = \frac{V_{th} \times J_{OP}}{P_{SUN}} \tag{3.7}$$

However, at AM 1.5, 100mW cm^{-2} of solar irradiance reduces the expression to

1.23V × J_{OP}.
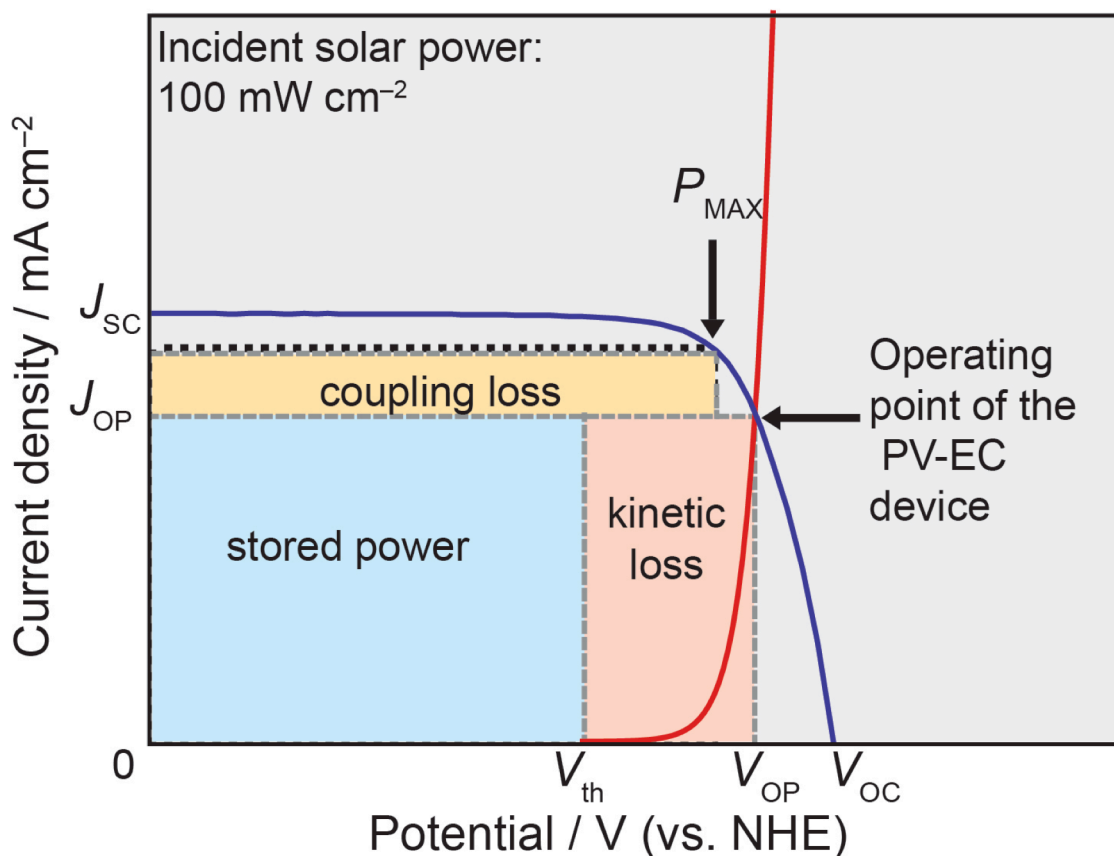
Figure 3.3 The generalized current density–voltage (*J–V*) diagram of a coupled PV–EC system where the point of intersection of the PV–curve (——, blue) and EC–curve (——, red) represents the operational point and SFE of the coupled PV–EC device. The SFE is maximized when the operating point is equal to P_{MAX}.

3.3 Steady–state equivalent circuit analysis

Solar cells and electrochemical reactions do not operate at thermodynamic limits. The steady–state electrical behavior of practical PV and EC systems can be described using equivalent circuits. Circuit analysis enables accurate modeling of

PV–EC devices and provides insight into their realistic performance and efficiency

limitations. The equivalent circuit of a PV device is well known and has been

described extensively in the literature and textbooks.[31] For the purposes of

equivalent circuit analysis of the PV component, the relevant circuit elements are
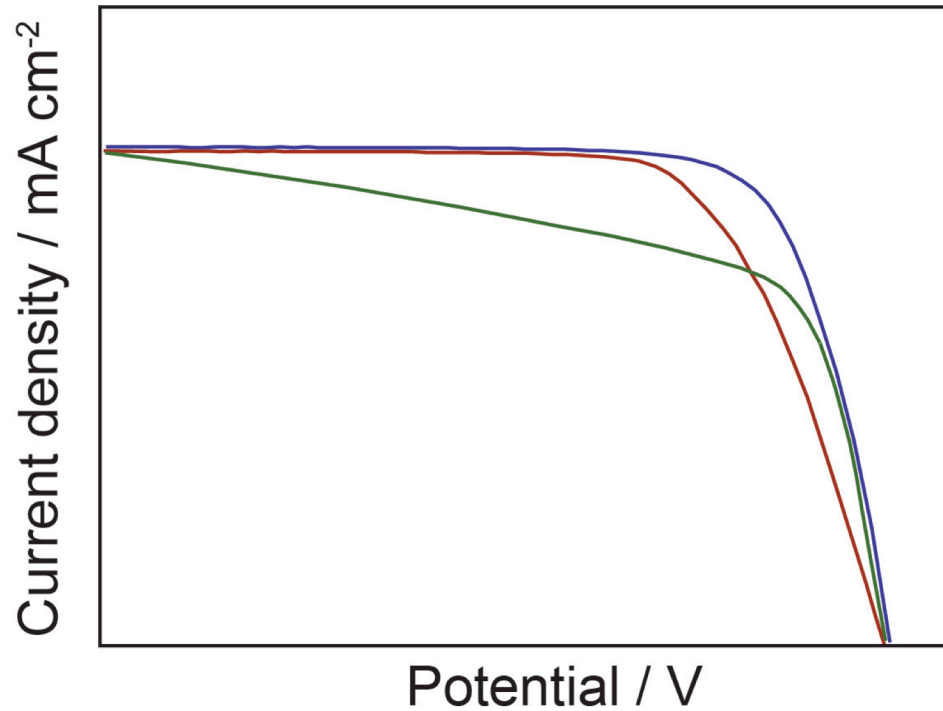
Figure 3.4 Impact on the *J–V* curve for a PV due to shunt (——, dark red) or series (——, dark green) resistance compared to an ideal *J–V* curve (——, dark blue).

discussed. Briefly, in a PV device light absorption generates a current of excited

electrons and holes. Some are separated by the internal junction and flow through

an external circuit with current density J_{PV} and some are lost to recombination

processes and contribute to the dark current of the solar cell J_0. Typically, only two

recombination mechanisms are considered to be relevant. The first recombination

mechanism is dominant at high voltages when bulk and surface recombination are

more prevalent. In this case the ideality factor *n*, which is a measure of how closely

the solar cell follows the ideal diode equation, is close to 1. At lower voltages,

recombination within the junction itself is the dominant recombination mechanism

and makes the ideality factor $n=2$. Both of these recombination mechanisms are

modeled by adding two diodes in parallel to the light generated current J_L. Ohmic

losses can be modeled by introducing shunt (R_{sh}) and series resistances (R_s). Shunt

resistance is caused by manufacturing defects and provides an alternate pathway

for light generated charge–carriers to flow ultimately decreasing the output

current–density (Fig 3.4). Series resistance is due to either resistance through

contact resistance or front metal contacts to silicon and decreases the output

voltage of the solar cell. The output current–density J_{PV} is the difference between the

light generated photocurrent J_L and the recombination currents:

$$J_{PV}(V) = J_L - J_{o,n=1}e^{\left[\frac{q(V + J_{PV}R_s)}{n_1 k_B T}\right]} - J_{o,n=2}e^{\left[\frac{q(V + J_{PV}R_s)}{n_2 k_B T}\right]} - \frac{V + J_{PV}R_s}{R_{sh}} \qquad (3.8)$$

where q is the electron charge, T is temperature, and k_B is Boltzmann's constant. If

multiple solar cells are connected in series then the output voltages are additive and

the current density of the system will decrease by dividing the current by the active

area under illumination.

Since the Tafel law can be rearranged to appear identical to the diode

equation, each electrochemical half–reaction can be represented as a diode under

reverse bias equal to the thermodynamic potential for water–splitting. Given the

constraints imposed by coupling the two PV and EC components, the equivalent

circuit in Fig. 3.5 can be solved numerically for the point of intersection between the

two resulting in the predicted SFE (recall 1.23 V × J_{OP}) for the coupled system.
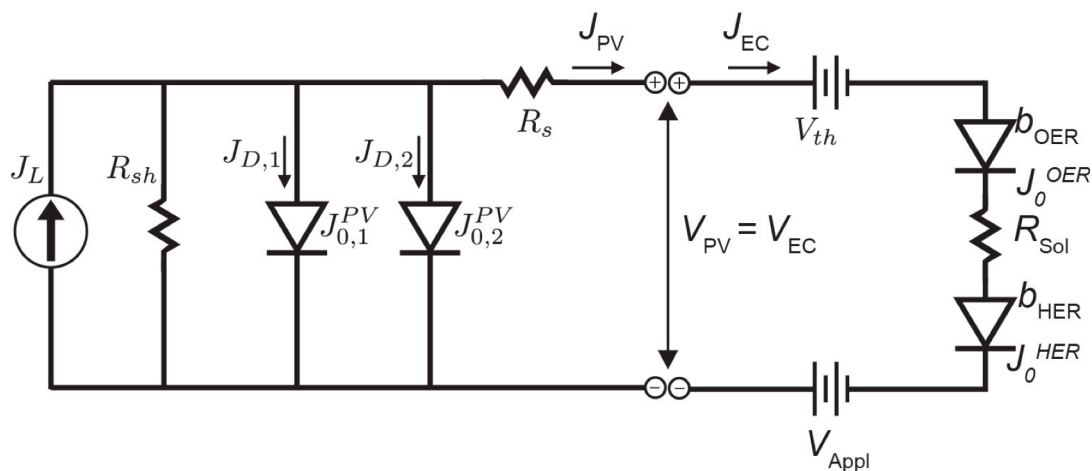
Figure 3.5 Steady–state equivalent circuit of a PV–EC system. An applied voltage is incorporated to illustrate analysis of an externally assisted system.

3.4 Results and Discussion

The PV parameters used herein assume that the system is powered by

multiple high–performance c–Si solar cells with η_{PV} = 20% (Table 3.1). Since the OER

reaction is typically efficiency limiting, two different sets of OER–catalyst

parameters based on the Co–OEC's and Ni–OEC's developed in our lab were used for

comparision (Table 2).[7, 22,23,28, 32–35] For the HER reaction the Tafel behavior is based

on a NiMoZn alloy.[28, 36]

Table 3.1 Solar cell parameters for the modeling

Solar cell parameters	
J_0	4×10^{-10} mA cm^{-2}
R_S	$1.5 \ \Omega$ cm^2
V_{OC}	669 mV
J_{SC}	41 mA cm^{-2}
Efficiency (%)	20

Table 3.2 Electrochemical parameters for the modeling.

Electrochemical parameters		Tafel slope (mV decade^{-1})	Exchange current density (A cm^{-2})
OER kinetics	Case I: Ni–OEC	30	5×10^{-18}
	Case II: Co–OEC	60	2.1×10^{-12}
HER kinetics		30	1×10^{-5}

3.4.1 Impact of η_{PV} on SFE

Fig. 3.6 shows a comparison between a comparison between two PV's where one PV is improved above the baseline $\eta_{PV} = 20\%$ to $\eta_{PV} = 23.3\%$ via a higher J_{SC} (47 mA cm^{-2}) and the other is improved via a higher V_{OC} (0.75 V). The first realization
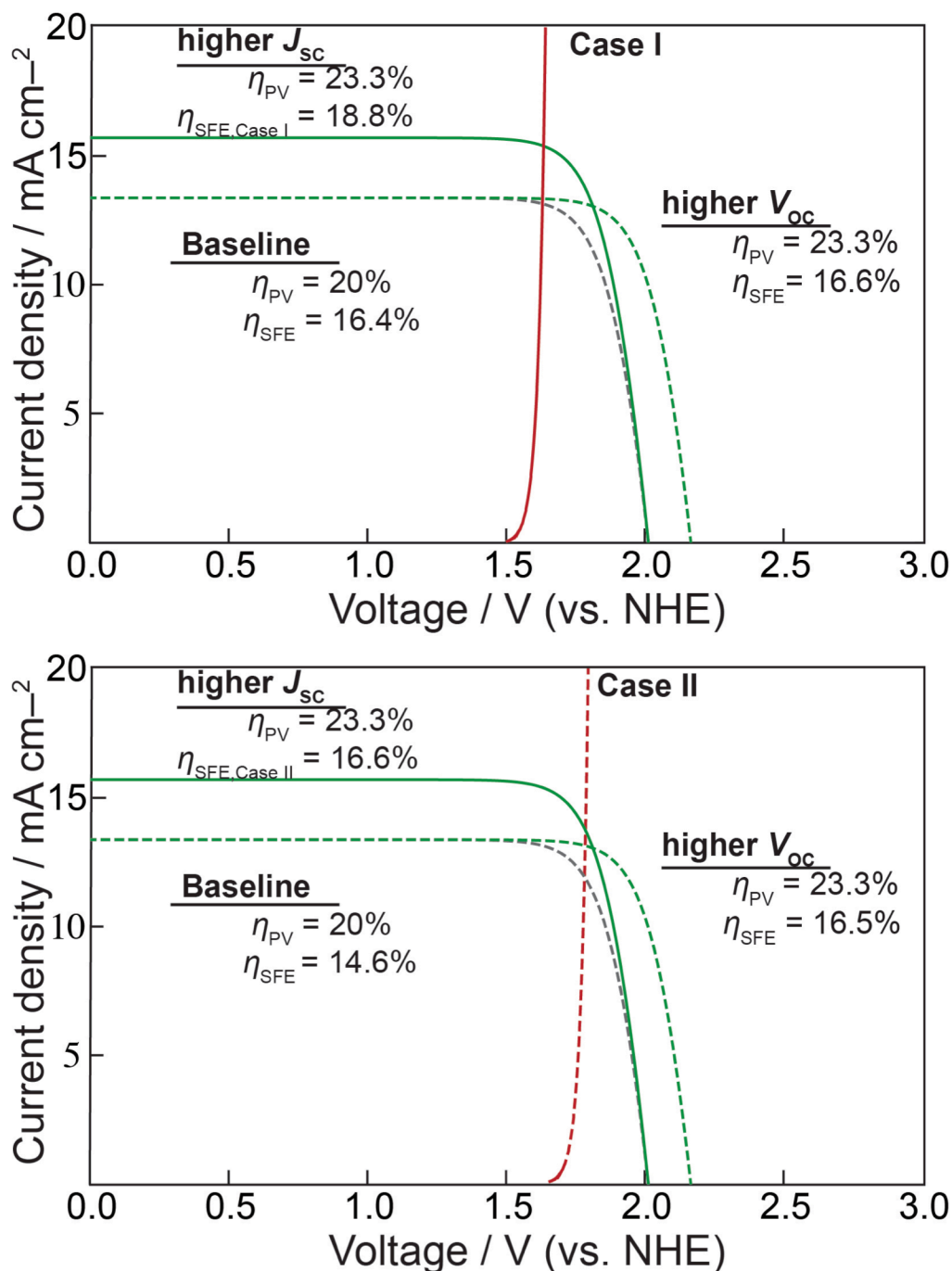
Figure 3.6 Impact on SFE via improvement in PV efficiency compared to the baseline $\eta_{PV} = 20\%$ (-----, grey dash). Given optimal coupling between the PV and EC components (top) a higher relative SFE can be obtained by improving the J_{SC} (——, green) as opposed to the V_{OC} (-----, dashed green). Given poor coupling between the baseline PV and EC (bottom), only minor improvements in the SFE can be obtained.

is that for Case I EC parameters in which there is good coupling between the PV and

EC components (i.e. the EC curve intersects to the left of P_{MAX}), improving η_{PV} via increasing J_{SC} gives a larger relative increase in SFE as compared to increasing the V_{OC} (15% vs. 1%). Additionally, the higher voltage PV hardly improves the SFE compared to the baseline η_{PV} = 20%. However, for Case II EC parameters, (i.e. when the EC curve occurs to the right of P_{MAX}), the higher current and higher voltage PV's show a similar increase in SFE.

3.4.2 Impact of η_{EC} efficiency on SFE

The equivalent–circuit analysis also allows us to determine the number of solar cells needed to achieve a high SFE given choice of catalyst as well as
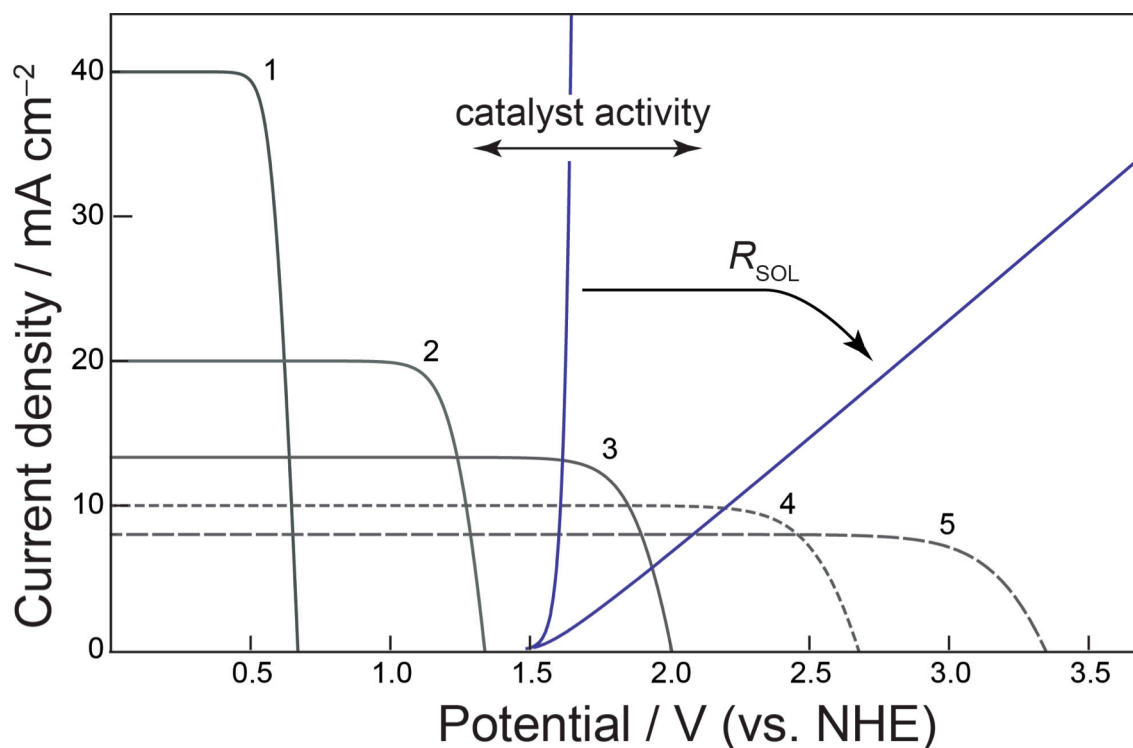
Figure 3.7 *J–V* curves of multiple series connected solar cells with η_{PV} = 20% (———, grey) and EC curves (———, dark blue). The number of solar cells required changes based on choice of catalyst which causes the EC curve to shift left or right and resistive losses due to R_{SOL} cause the EC curve to tilt down.

resistive losses. Since an ionic conductivity is at least four orders of magnitude less than electronic conductivity (i.e. resistance through electrodes or wires) we choose to specifically focus on solution resistance R_{SOL}. Figure 3.7 shows that choice of catalyst shifts the EC curve horizontally and that R_{SOL} causes the EC curve to tilt down and both change the number of solar cells required.

Fig. 3.8 shows the SFE as a function of solution resistance given the η_{PV} = 20% parameters and two sets of EC parameters (Tables 3.1 and 3.2). In order to maintain an SFE of 10% or higher, the number of solar cells changes and 3–5 solar cells are required. For Case I EC parameters an SFE of 10% based on 3 solar cells is only achieved with minimal solution resistance R_{SOL} and rapidly drops below 10%. However, by increasing to 4 cells, a 12% SFE can achieved until the R_{SOL} surpasses 90 Ω cm^2. Interestingly, given the set of PV parameters, increasing to 5 cells produces just under a 10% SFE because J_{OP} / 5 is less than the minimum current–density needed to give a 10% SFE (i.e. 8.13 mA cm^{-2}). The trends are the same for Case II EC parameters. However the lower Tafel slope of the NiB$_i$ catalyst results in a larger η_{EC}, producing a 14.5% SFE using 3–cells and maintains > 10% until R_{SOL} attains 20 Ω cm^2, in which case 4 cells are needed. Again, utilizing 5 cells results in a J_{OP} that is too small to produce a 10% or higher SFE.
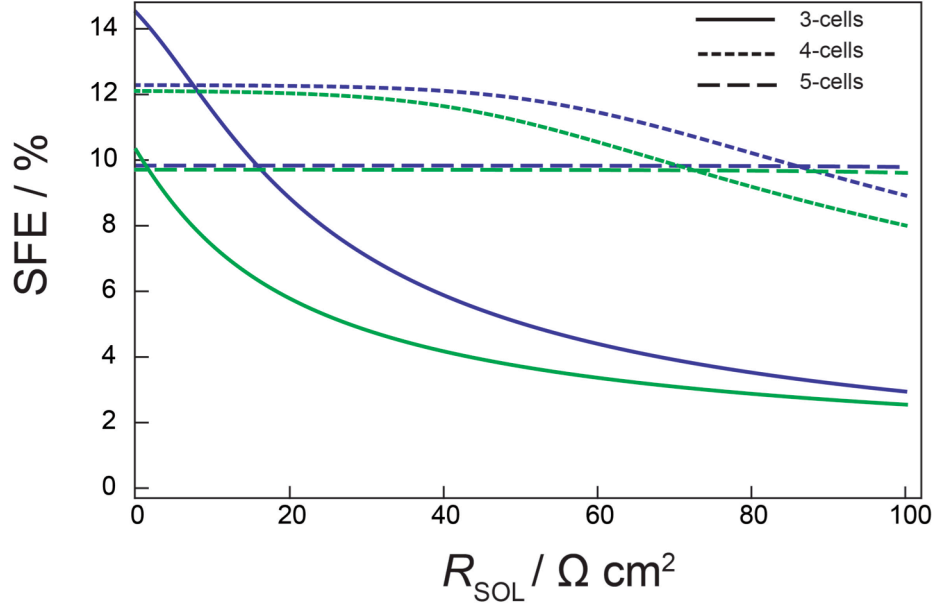
Figure 3.8 Impact of solution resistance and EC parameters on SFE given η_{PV} = 20%. Case I EC parameters (──, green) are based on utilizing the Co–OEC and Case II EC (──, navy) are based on utilizing the Ni–OEC.

3.5 Model validation

As a case study, we used this steady–state equivalent circuit analysis to analyze the OER half–reaction in an experiment identical to those discussed in Chapter 2. In this experiment, the CoB_i catalyst was deposited on the p–terminal of a single–junction c–Si solar cell. Since additional voltage (V_{appl}) was applied to assist in the OER reaction equation 3.4 was modified as follows:

$$V_{EC} + V_{appl} = V_{th} + \eta_{OER}(J_{EC}) \tag{3.9}$$

where V_{th} is now the Nerstian potential for the water–oxidation reaction which is 0.68 V vs. NHE at pH 9.2. This is represented in Fig. 3.9, which shows the J–V

characteristics of the PV device used and *J–V* behavior for the OER reaction

(obtained via steady–state Tafel analysis in isolation from the solar cell) which is

shifted to lower potentials by V_{appl} until the two–curves intersect, resulting in the

predicted behavior of the PV–assisted OER reaction.
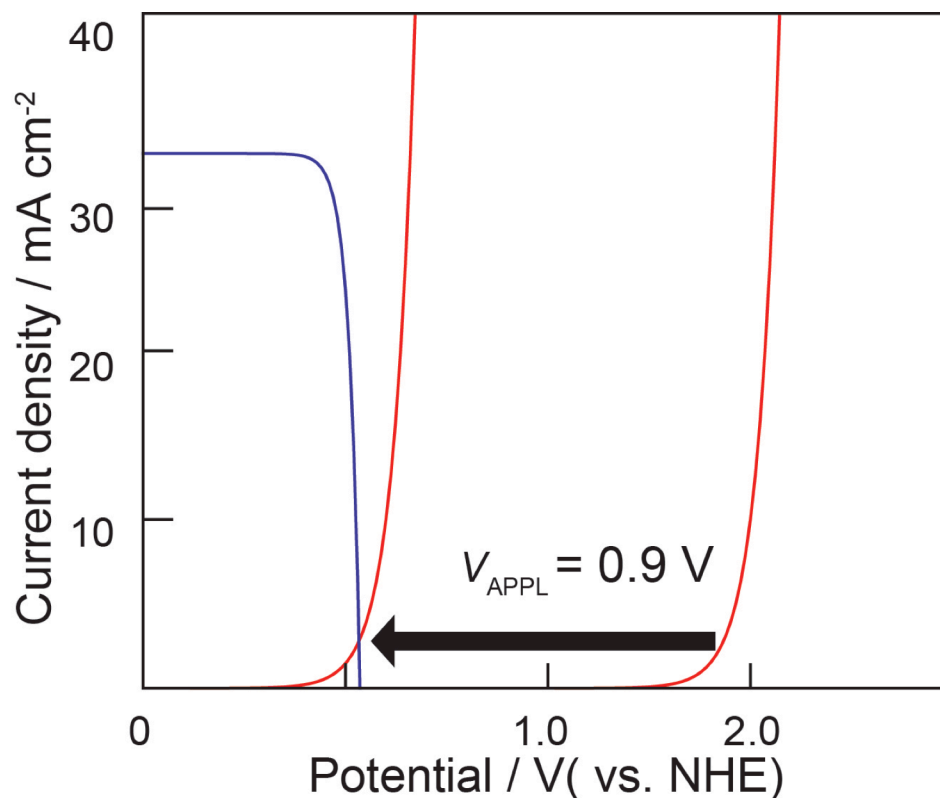
Figure 3.9 Graphical demonstration of how the predictive analysis works for PV–assisted reactions, where the PV–curve (——, blue) is based on the *J–V* characteristics of an in–house built single junction c–Si PV and the EC–curve (——, red) is based on the CoB_i water–oxidation catalyst operating in pH 9.2 solution.

In Fig. 3.10 the predicted behavior of the coupled PV–EC system is compared

to the experimentally measured Tafel analysis of a PV–assisted photoanode. By

using the *J–V* properties of the solar cell depicted in Fig. 3.9, and the independently

measured Tafel analysis of the CoB_i catalyst, the coupled behavior is determined; the

measurement and prediction agree to within < 10mV. Furthermore, as mentioned in

Chapter 2, the voltage offset between the Tafel slopes for the OER–functionalized c–Si photoanodes under the light configuration and the configuration in which the PV is bypassed is exactly the V_{OC} of the solar cell. Since Tafel analysis is conducted at very low current–densities of 1 mA cm^{-2} or lower, this requires that the system must be coupled near the V_{OC} of the solar cell.
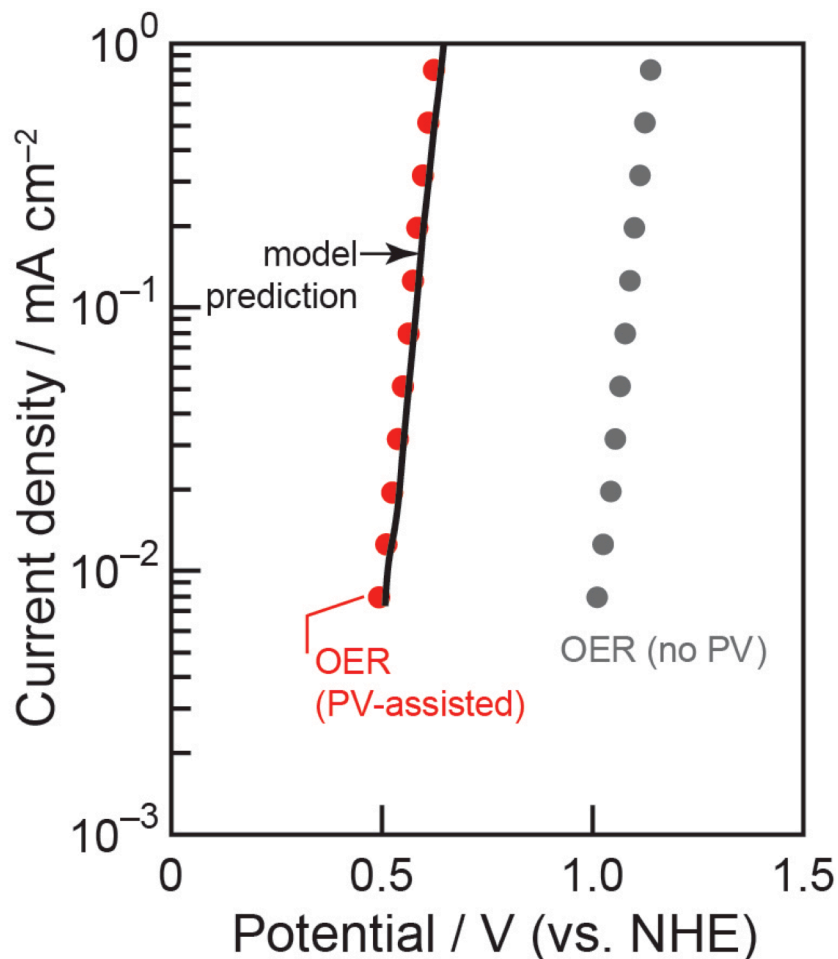
Figure 3.10 Predicted Tafel behavior of a PV–assisted water oxidation system similar to the experiments described in Chapter 2. The electrical properties of the PV (shown in Fig. 3.8) and EC systems were measured independently (●, black dots) and used to predict the coupled behavior (——, black). The Tafel analysis of the PV–assisted photoanode (●, red dots) and predicted behavior match to within 10 mV.

3.6 Conclusion

A framework is outlines for integrating a series of single–junction c–Si solar

cells with recently developed water–splitting catalysts for direct solar–to–fuels conversion. The steady–state equivalent circuit analysis gives a tool that allows us to predict the efficiency for a coupled PV–EC system. This analysis allows us to determine the optimal number of solar cells required for a stand–alone water-splitting device based on catalyst choice and considering resistive losses. The model is validated by correctly predicting the J–V characteristics of a PV–assisted OER photoanode. These results pave a path to our goal of designing a stand–alone water-splitting device based on all terrestrially ready materials exhibiting a solar–to–fuels efficiency of 10% or higher.

3.7 Experimental

Sample Fabrication. Crystalline silicon solar cells were fabricated according to previously published procedures.[37] The CoB$_i$ OER–catalysts was deposited via bulk electrolysis in a two–compartment electrochemical cell with a glass frit of fine porosity. For the electrodeposition, the working compartment was charged with ~50mL solution (25 mL of 0.2M KBi electrolyte and 25 mL of 1mM Co^{2+} solution). The auxiliary compartment was charged with 0.1 M KB$_i$ electrolyte at pH 9.2. The working electrode was the surface passivated c–Si solar cell. Typically, 1 cm^2 are of the working electrode was immersed in the solution and electrolysis was carried out at 0.85 V vs. NHE until 26 mC cm^{-2} of charge passed.

Photoelectrochemistry experiments. Photoelectrochemistry experiments were performed in a one–compartment quartz cell. The light source was a Sol 2A solar simulator (Newport). The Tafel behavior of the surface–passivated, catalyst–

functiaonlized solar cells was measured in the region of water–oxidation over a 200 mV range in 10 to 30 mV increments. The measurements were conducted in a solution containg 0.5 M KB_i and 1.5 M KNO_3 at pH 9.2, using an Ag/AgCl reference electrode and Pt auxiliary electrode.

3.8 References

1. Bolton JR, Hall DO (1979) Photochemical conversion and storage of solar energy. *Annu. Rev. Energy* **4**, 353–401.

2. Parkinson B (1984) On the efficiency and stability of photoelectrochemical devices. *Acc. Chem. Re.s* **17**, 431–437.

3. Bolton JR, Strickler SJ, Connolly JS (1985) Limiting and realizable efficiencies of solar photolysis of water. *Nature* **316**,495–500.

4. Weber MF, Dignam MJ (1984) Efficiency of splitting water with semiconducting photoelectrodes. *J. Electrochem. Soc.* **131**,1258–1265.

5. Weber MF, Dignam MJ (1987) Splitting water with semiconducting photoelecrodes–efficiency considerations. *Int. J. Hydrog. Energy* **4**, 225–232.

6. Rocheleau RE, Miller EL (1997) Photoelectrochemical production of hydrogen: Engineering loss analysis. *Int. J. Hydrog. Energy* **22**,771–782.

7. Surendranath Y, Bediako DK, Nocera DG (2012) Interplay of oxygen–evolution kinetics and photovoltaic power curves on the construction of artificial leaves. *Proc. Natl. Acad. Sci. U.S.A* **39**, 15617–15621.

8. Kelly NA, Gibson TL (2006) Design and characterization of a robust photoelectrochemical device to generate hydrogen using solar water splitting. *Int. J. Hydrog. Energy* **31**,1658–1673.

9. Walter MG et al. (2010) Solar water splitting cells. *Chem. Rev.* **110**, 6446–6473.

10. Shockley W, Queisser HJ (1961) Detailed balance limit of efficiency of p-n junction solar cells. *J. Appl. Phys.* **32**, 510–519.

11. Swanson RM (2005) in *Conference Record of the Thirty–first IEEE Photovoltaic Specialists Conference, 2005*, pp 889–894.

12. Green MA (2009) The path to 25% silicon solar cell efficiency: History of silicon cell evolution. *Prog. Photovolt. Res. Appl.* **17**,183–189.

13. Powell DM et al. (2012) Crystalline silicon photovoltaics: a cost analysis framework for determining technology pathways to reach baseload electricity costs. *Energy Environ. Sci.* **5**, 5874–5883.

14. Rech B, Schmidt SS, Schlatmann R (2013) *Transition to Renewable Energy Systems*, eds Stolten D, Scherer Ing Viktor (Wiley–VCH Verlag GmbH & Co. KGaA).

15. Cukier RI, Nocera DG (1998) Proton–coupled electron transfer. *Annu. Rev. Phys. Chem.* **49**, 337–369.

16. Eisenberg R, Gray HB (2008) Preface on making oxygen. *Inorg. Chem.* **47**,1697–1699.

17. Betley TA et al. (2008) A ligand field chemistry of oxygen generation by the oxygen–evolving complex and synthetic active sites. *Philos. Trans. R. Soc. B Biol. Sci*. **363**,1293–1303.

18. Hammes–Schiffer S (2009) Theory of proton–coupled electron transfer in energy conversion processes. *Acc. Chem. Res.* **42**, 1881–1889.

19. Concepcion JJ et al. (2009) Making oxygen with ruthenium complexes. *Acc. Chem. Res.* **42**, 1954–1965.

20. Surendranath Y, Nocera DG (2011) *Oxygen evolution reaction chemistry of oxide–based electrodes.* Prog. Inorg. Chem. 57 (John Wiley & Sons, INc., Hoboken, NJ, USA).

21. Surendranath Y, Bediako DK, Nocera DG (2012) Interplay of oxygen–evolution kinetics and photovoltaic power curves on the construction of artificial leaves. *Proc. Natl. Acad. Sci.* **109**, 15617–15621

22. Surendranath Y, Kanan MW, Nocera DG (2010) Mechanistic Studies of the oxygen evolution reaction by a cobalt–phosphate catalyst at neutral pH. *J. Am. Chem. Soc.* **132**,16501–16509.

23. Bediako DK, Surendranath Y, Nocera DG (2013) Mechanistic studies of the oxygen evolution reaction mediated by a nickel–borate thin film electrocatalyst. *J. Am. Chem. Soc.* **135**, 3662–3674.

24. Hernández–Pagán EA et al. (2012) Resistance and polarization losses in aqueous buffer–membrane electrolytes for water–splitting photoelectrochemical cells. *Energy Environ. Sci*. **5**, 7582–7589.

25. McCrory CCL, Jung S, Peters JC, Jaramillo TF (2013) Benchmarking heterogeneous electrocatalysts for the oxygen evolution reaction. *J. Am. Chem. Soc.* **135**, 16977–16987.

26.   Nikolic VM et al. (2010) Raising efficiency of hydrogen generation from alkaline water electrolysis – Energy saving. *Int. J. Hydrog. Energy* **35**, 12369–12373.

27.   Zeng K, Zhang D (2010) Recent progress in alkaline water electrolysis for hydrogen production and applications. *Prog. Energy Combust. Sci.* **36**, 307–326.

28.   Reece SY et al. (2011) Wireless Solar Water Splitting Using Silicon–based semiconductors and earth–abundant catalysts. *Science* **334**, 645–648.

29.   Winkler MT, Cox CR, Nocera DG, Buonassisi T (2013) Modeling integrated photovoltaic–electrochemical devices using steady–state equivalent circuits. *Proc. Natl. Acad. Sci.* **110**, E1076–E1082.

30.   Rocheleau RE, Miller EL, Misra A (1998) High–efficiency photoelectrochemical hydrogen production using multijunction amorphous silicon photoelectrodes. *Energy Fuels* **12**, 3–10.

31.   Nelson J (2003) *The Physics of Solar Cells* (Imperial College Press, London).

32.   Kanan MW, Surendranath Y, Nocera DG (2009) Cobalt–phosphate oxygen–evolving compound. *Chem. Soc. Rev.* **38**:109.

33.   Dincă M, Surendranath Y, Nocera DG (2010) Nickel–borate oxygen–evolving catalyst that functions under benign conditions. *Proc. Natl. Acad. Sci.* **107**, 10337–10341.

34.   Huynh M, Bediako DK, Nocera DG (2014) A Functionally stable manganese oxide oxygen evolution catalyst in acid. *J. Am. Chem. Soc.* **136**, 6002–6010.

35.   Huynh M, Bediako DK, Liu Y, Nocera DG (2014) Nucleation and growth mechanisms of an electrodeposited manganese oxide oxygen evolution catalyst. *J. Phys. Chem. C.* Available at: http://dx.doi.org/10.1021/jp501768n [Accessed June 12, 2014].

36.   Steven Y. Reece, Esswein AJ, Sung K, Green Z, Nocera DG (2013) *Compositions, Electrodes, Methods, and Systems for Water Electrolysis and Other Electrochemical Techniques. US Patent Appl. No.* 8361288.

37.   Cox CR, Winkler MT, Pijpers JJH, Buonassisi T, Nocera DG (2013) Interfaces between water splitting catalysts and buried silicon junctions. *Energy Environ. Sci.* **6**, 532–538.

Chapter 4–10% solar–to–fuel efficiency with non–precious materials

4.1 Introduction

In order to make a solar–water–splitting device economically viable the commonly accepted metric is that a 10% or higher solar–to–fuels efficiency (SFE) is required.[1-3] Currently, the record–holding SFE for solar water–splitting devices is between 16–18%.[1,4] Both of these were based on expensive group III–V multi–junction solar cells and precious water–splitting catalysts such as Pt and Ru. More recently, devices constructed utilizing cheaper PV components such as triple–junction amorphous silicon (a–Si) [5-9]and copper indium gallium diselenide (CIGS) have also been demonstrated.[10,11] Of these demonstrations, few used earth–abundant water–splitting catalysts and many operated in highly acidic or basic solutions, which impaired long–term stability. Currently, the record SFE for a stand–alone water splitting device composed of all earth abundant and technology ready materials operating in benign solutions is 4.7%.[7,12] This result was based upon "the artificial leaf," which was composed of a triple–junction a–Si solar cell, a CoB_i oxygen–evolution catalyst (OEC) and a NiMoZn alloy hydrogen–evolution catalyst (HEC). HOwever, given the efficiency limitations of triple–junction a–Si solar cells[13,14] a 10% or higher SFE cannot be achieved until the PV technology has improved.

In Chapter 3, equivalent circuit analysis of a coupled PV–EC system based on a string of single junction c–Si solar cells and earth–abundant catalysts predicted a SFE of 10% could readily be achieved. Guided by steady–state equivalent circuit analysis described in Chapter 3, here we demonstrate that an SFE >10% can be achieved with all non–precious, low-cost, commercially ready components and

materials. Specifically, we present a rational systems design approach to evaluate

each component of a modular PV–EC device comprised of a c–Si PV mini–module

and non–precious catalysts for the hydrogen–evolution and oxygen–evolution

reactions (HER and OER, respectively). Although this approach does not result in a

monolithic structure in which catalysts at directly deposited on the PV device (a.k.a.

an artificial leaf), as discussed in Chapter 3 the equivalent circuit for both constructs

is identical.[15] This approach allows for modular independent optimization, after

which the components could be integrated into a monolithic design.

4.2 Results

Water–splitting catalysts can be integrated with a c–Si PV module either

directly by depositing catalysts onto silicon (Fig. 4.1) or indirectly by wiring the PV–

module to electrodes (Fig.4.2). In order to make the PV–EC device with minimal

fabrication and adopt a completely modular approach such that every component

can be tested, characterized, and replaced systematically we chose apply the

indirect method. Such a configuration also allows us to utilize electrodes that are not

restricted to the PV area. However, for all of the measurements conducted herein

the electrode area was kept proportional to the PV–module area such that all

photoelectrochemical (PEC) measurements would be reflective of an equivalent

monolithic device.

Since the PV–EC modular configuration allows for independent optimization

of the PV–component and electrochemical components (electrodes and catalysts),

the operating point for the coupled PV–EC device can be illustrated graphically as

the intersection point of the independently measured current–voltage (*J*–*V*) curves

for the PV and EC for water–splitting.
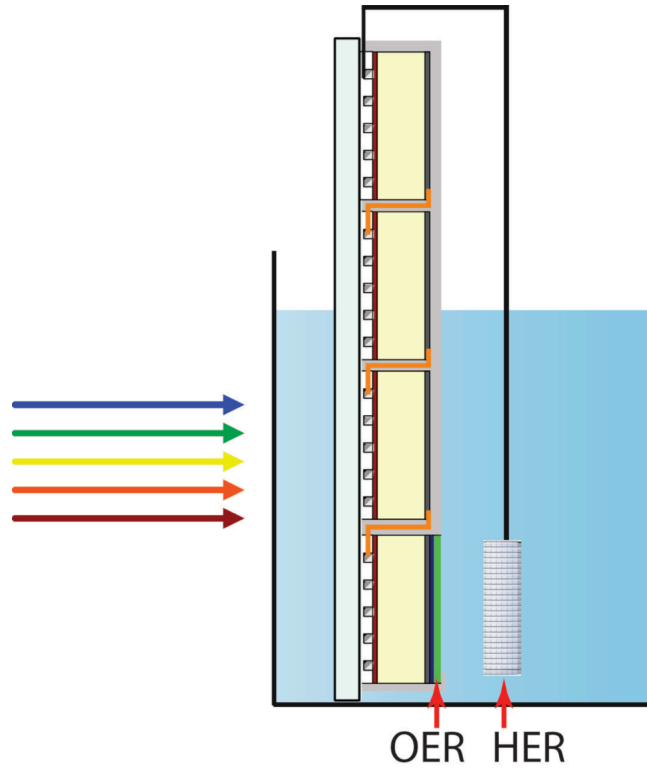
Figure 4.1 Schematic of a PV–EC device based on series–connected single–junction c–Si solar cells and water–splitting catalyst. In this configuration the OER–catalyst is directly deposited on the back of the last solar cell in the stack.
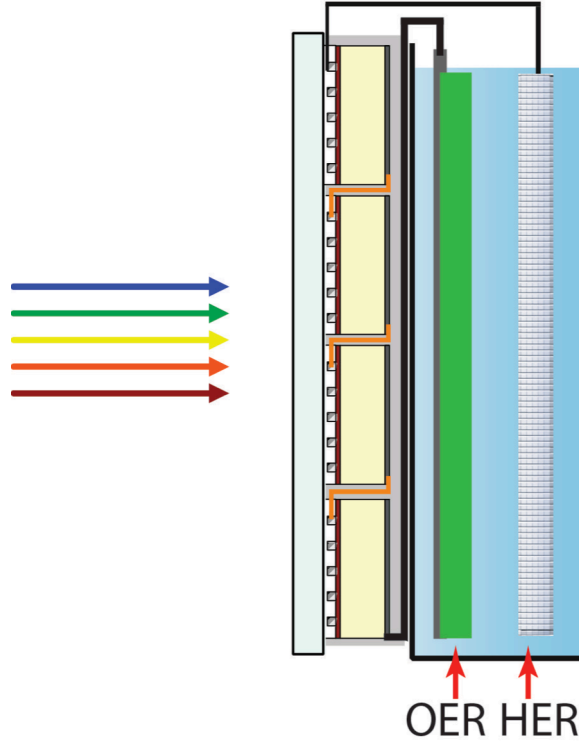
Figure 4.2 Schematic of a PV–EC device used in these studies. In this modular configuration each component can be easily evaluated and replaced independently.

The point of intersection give the operational current density, J_{OP}, which is related to the SFE by multiplying by the thermodynamic potential for water–splitting and Faradaic efficiency, $\eta_{Far:}$

$$\text{SFE} = \frac{(1.23\ \text{V}) \cdot J_{OP} \cdot \eta_{Far}}{P_{sun}(\text{mW cm}^{-2})} \tag{4.1}$$

For maximum SFE, the intersection of the PV and EC J–V curves occurs at a voltage above the minimum voltage required for water–splitting (i.e. thermodynamic potential, plus additional kinetic overpotentials and cell resistances), but below the voltage at the maximum power–point of the PV module,

77

V_{MPP}. This later point is supported by Eq. 4.1, whereby the efficiency is proportional to J_{OP} and maximized at voltages below V_{MPP} as shown in Fig. 4.3 which shows the J–V curve for the mini–modules used for the PV–EC device. The modules were constructed from either 3 or 4 commercial single–junction c–Si solar cells connected in series. When connecting the cells in series, the J–V properties show that upon addition of solar cells the voltages are additive, while the current density decreases as 1/area (see Table 4.1 for PV–module characteristics). It should be noted that the overall PV efficiency is maintained upon connecting N cells in series because the
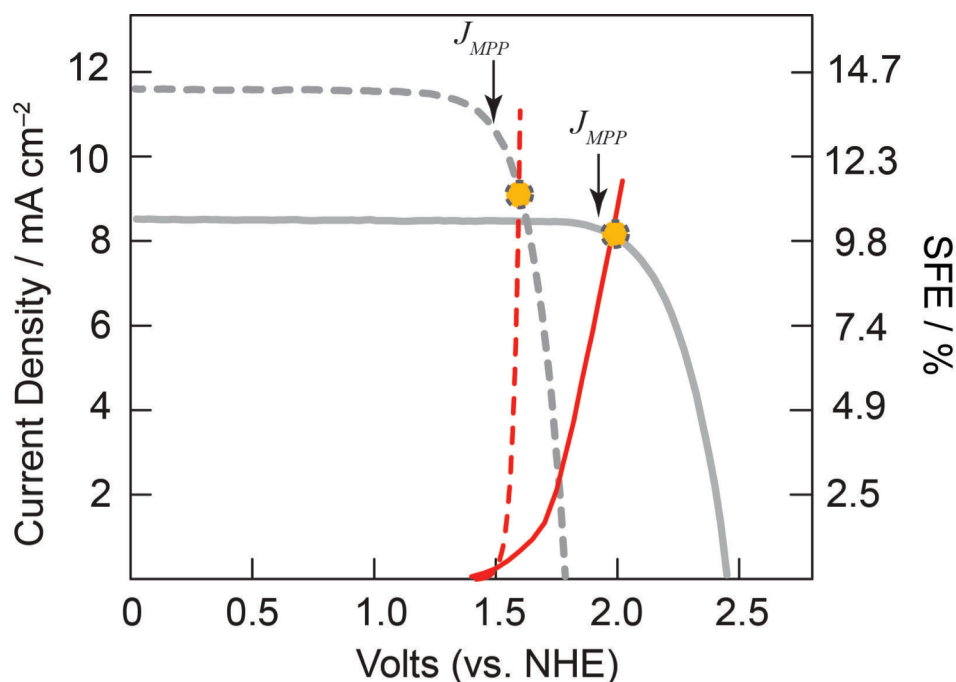
Figure 4.3 J–V curves of the individually measure PV and EC components making up the PV–EC device. The grey curves represent the J–V curves for the PV modules composed of either three (----, grey–dashed) or four (——, grey–solid) single–junction c–Si solar cells measure under AM 1.5 illumination. The red curves represent electrochemical load J–V curves using NiB_i and NiMoZn catalysts, where the ideal EC curve (----, red–dashed) is based on previously reported Tafel analysis and the actual EC curve (——, red) measured in a 2–electrode experiment (0.5M KB_i / 0.5M K_2SO_4, pH 9.2). The point of intersection represents the J_{OP} (●, orange circles) and the SFE of the coupled system.

module voltage will be xN larger than the indivdual cell, and the current density will be x1/N that of an indivdual cell.

Table 4.1. PV characteristics for the 3 and 4–cell c–Si mini–modules.

PV module characteristics	4– cell	3–cell
V_{OC} (V)	2.46	1.79
J_{SC} (mA cm^{-2})	51.0	52.2
Active Area (cm^2)	6.0	4.5
Fill Factor	76.9	76.2
Efficiency (%)	16.0	15.8

The choice of water–splitting catalysts was based upon independent studies of the catalysts developed in our group. Presently, the NiB$_i$ OER catalyst is the most active OEC, requiring only 430 mV of overpotential to achieve a current density of 10mA cm^{-2}, making it an order of magnitude better than the previously developed Co–OEC's given the same amount of material.[16] For the HER–catalyst a NiMoZn alloy was used which has been previously shown to achieve current densities of 700 mA cm^{-2} at 100 mV overpotential and, with continued leaching in 6M KOH can attain activities as high as at 1000 mA cm^{-2} at an overpotential of 35 mV.[7,12,17] Given our modular approach the current–voltage characteristics of out EC–component can be independently evaluated.

Considering a PV–EC device based on commercially available single junction– Si solar cells and literature values for the previously reported Tafel behavior of the

catalysts utilized herein, equivalent–circuit modeling predicts a 10% or higher SFE

can be achieved using three single–junction c–Si devices series connected in a mini–

module with a PV efficiency of 15% or higher (red dashed curve Fig. 4.3). However,

this is only the case if all resistive losses are negligible; if resistive losses are

present, the operating point can occur to the right of V_{MPP}, reducing J_{OP} and SFE.

Modeling indicates that using a 4–cell c–Si module overcomes the impact of resistive

losses on SFE.[15]

 To test these predictions, the steady–state current–voltage characteristics of

the NiB_i anode and NiMoZn cathode were measured in a two–electrode setup in KB_i

buffer at pH 9.2. The intersection at which the overlaid current–voltage

characteristics of the half–reactions with the J–V curve of the PV mini–modules

illustrates J_{OP} and the resulting SFE for the coupled PV–EC device. Confirming the

design considerations for resistive losses, we estimate a SFE of 2.8% for a 3–cell

module and 10% for a 4–cell module (Fig.4.3).

4.2.1 Device integration

 The simplest way to integrate the PV and EC components and verify the

independently estimated SFE is to connect the PV module with the NiB_i anode and

NiMoZn cathode. The photocurrent through the integrated device can be measured

and should match the predicted J_{OP} obtained in Fig. 4.3. The key criteria used to

validate the PV–EC device are the reporting protocols established by Chen *et al.*[18]

These protocols include measurements utilizing a 2–electrode setup without the

influence of an potential bias, product quantification (i.e. H_2 and O_2), and assessment

of the long–term stability of the device under AM 1.5 illumination. In addition to product quantification, we wished to ensure that parasitic currents due to product crossover reactions do not influence J_{OP}. The impact on the SFE due to H_2 oxidation can be estimated by examining the mass–transport limited current density, which is given by:

$$J_L = \frac{nFDc_b}{\delta} \tag{4.2}$$

where, n is the number of electrons, F is Faraday's constant, c_b is the bulk concentration of species in solution, D is the diffusion coefficient (5.11×10^{-5} cm^2 s^{-1} for H_2 in water), and δ is the Nernst diffusion layer thickness. Assuming H_2 saturation in water $c_b = 7.8 \times 10^{-7}$ mol cm^{-3}, and a reasonable value for δ (given a planar electrode with no artificially imposed convection) is around 0.05 cm[19] this estimates that a current density of 8.13 mA cm^{-2} (10% SFE) would have a parasitic current of 0.15 mA cm^{-2} (reducing 10.0% SFE to 9.8% SFE). However, the NiB_i is a specific OER catalyst and Fig. 4.4 shows that the steady–state current density of the catalyst under Ar and H_2 is identical, indicating that this crossover reaction is negligible.
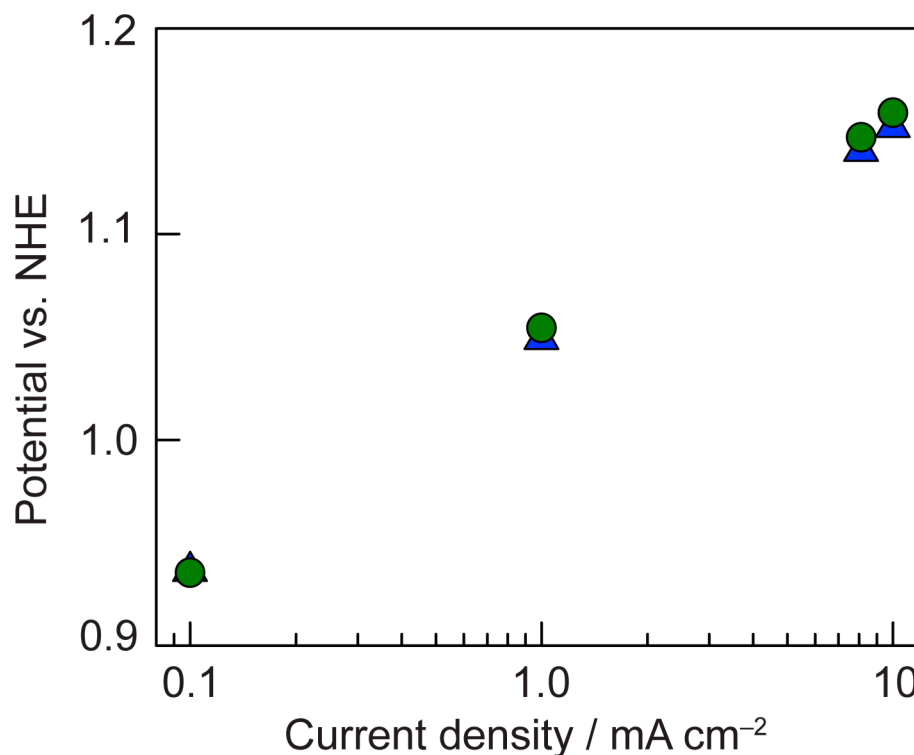
Figure 4.4. Steady-state current voltage behavior for the NiB_i operating in 0.5M KB_i / 0.5 M K_2SO_4 pH 9.2 in H_2 saturated solution (●) and in Ar saturated solution (▲). Since the voltage required to achieve a given current density under both conditions is almost identical indicates that the contribution of H_2 oxidation at the anode is negligible.

Fig. 4.5 shows the measured J_{OP} of the PV–EC device, which initially starts at 8.35 mA cm^{-2} corresponding to an SFE of 10.2%. During the first few min of illumination J_{OP} decreases to a steady–state value of 7.8 mA cm^{-2}. The initial decline in J_{OP} is consistent with heating of the PV–module under illumination causing a decrease in solar cell voltage, which shifts the maximum power point toward the origin.
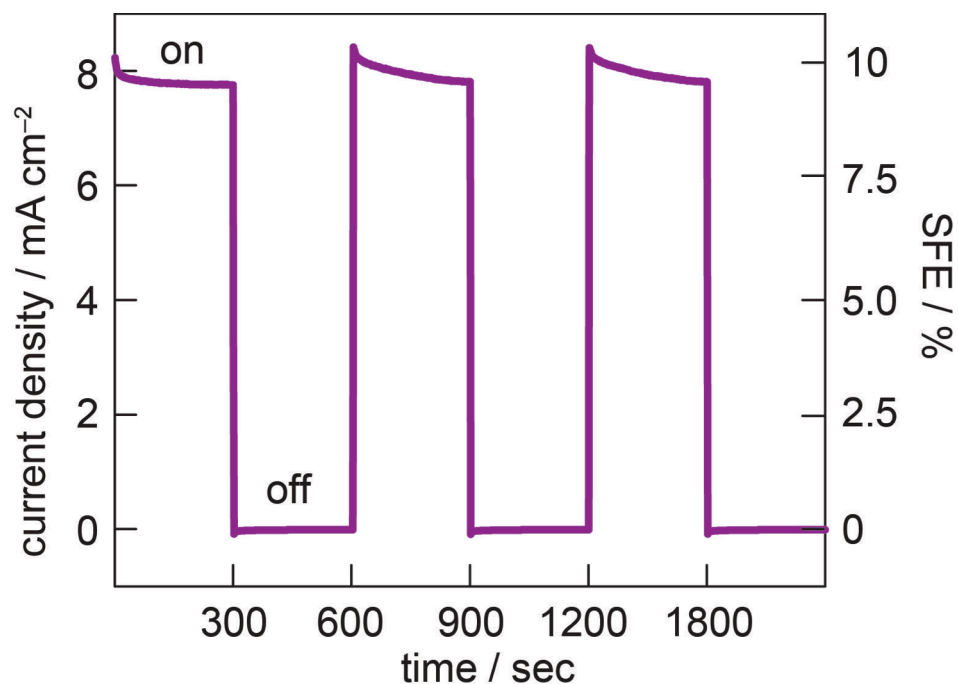
Figure 4.5 Current under chopped illumination representing J_{OP} for the PV–EC device in 0.5M KB_i / 0.5M K_2SO_4 pH9.2. The chopped illumination illustrates the recovery in SFE and reproducibility in measuring J_{OP} through the PV-EC device

This is confirmed by measuring the V_{OC} of the mini–module as a function of time showing ~130 mV decrease which is consistent in a temperature change of 15 °C (Fig. 4.6).[20] In line with PV module heating, turning the lamp off for 5 min and then turning it back on causes the SFE to recover to 10.2% (Fig. 4.6).
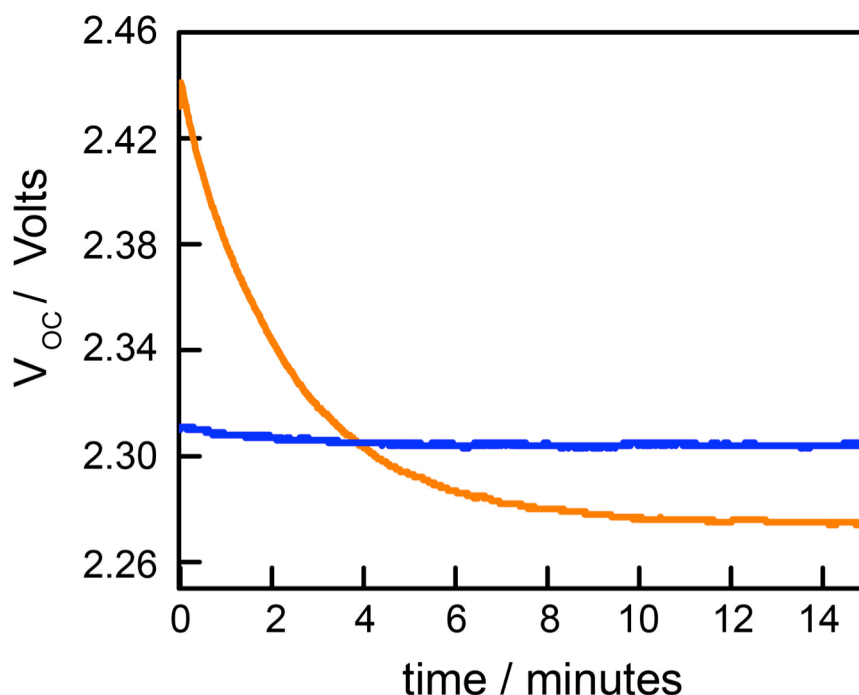
Figure 4.6 Decay of the open–circuit voltage of the 4–cell PV mini–module over the course of ~15 min. The initial V_{OC} at 2.42 V decays to a steady–state of 2.27 V after the first 10 min (——, orange), which contributes to the initial decline in the SFE of the coupled PV–EC device. After overnight illumination, the Voc was measured (——, blue) and shows a slight recovery to 2.31 V, which corresponds to the initial increase in SFE of the PV–EC device during the first 24 h.

4.3 Discussion

The largest efficiency losses for the PV–EC device result from series resistance through the electrodes (R_{EL}) and solution resistance (R_{SOL}). The former is straightforward to address by using metal electrodes as substrates for the OER and HER catalysts. Presumably the use of metallic substrates makes resistance through the electrodes as well as contact resistance negligible. Solution resistance in buffered electrolytes, as opposed to strong acids or bases, remains a challenge. The primary reason for a less than optimal R_{SOL} is the limited solubility of the buffer.[21] In the case of borate buffer this is the solubility limit of boric acid, which is around 1 M

corresponding to a specific conductance of 26 mS cm^{-1}. The specific conductivity can be improved by adding an inert salt as a supporting electrolyte (Fig. 4.7). For example, when utilizing KNO$_3$, the specific conductance of 0.5 M KB$_i$ / 1.5 M KNO$_3$ is 126 mS cm^{-1}.
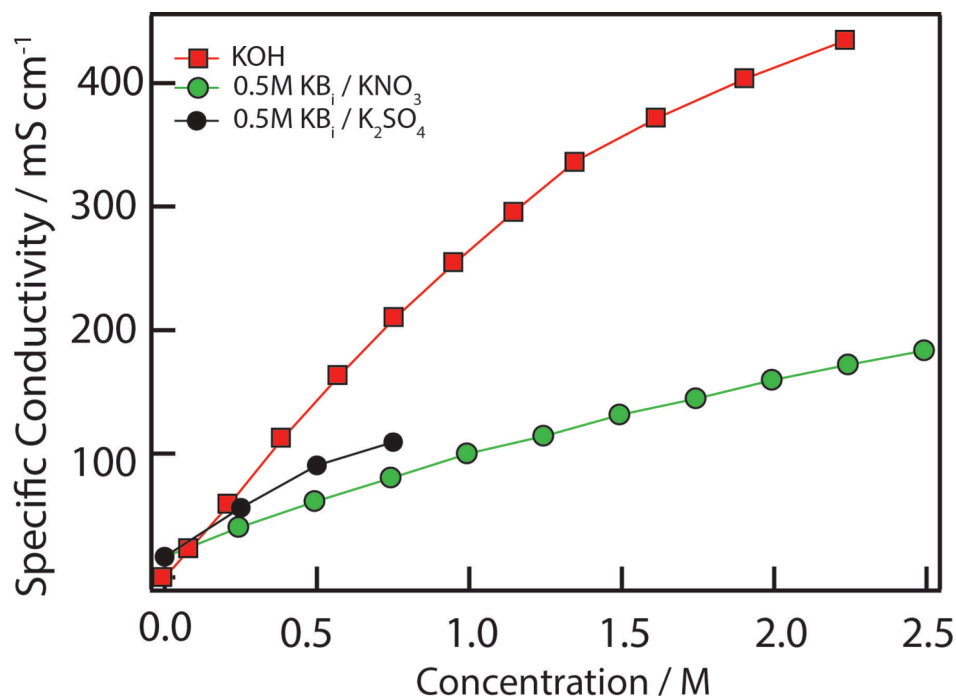
Figure 4.7 Specific conductance measurements for various electrolytes considered to minimize R_{SOL}. KOH (■, red squares) is the most conductive electrolyte; in order to operate in pH near neutral regimes 0.5M KB$_i$ was used with additional supporting electrolyte, such as KNO$_3$ (●, green circles) or K$_2$SO$_4$ (●, black circles).

     The choice or supporting electrolyte is straightforward in typical electrochemical experiments where only one half–reaction at either the anode or cathode is of interest. When considering deleterious side–reactions for both the anode and cathode, the supporting electrolyte must be inert over a wider potential range. Given our modular approach, the choice of supporting electrolyte was determined by measuring the Faradaic efficiency for each electrode/electrolyte

configuration independently before being implemented into the PV–EC device. For example, Fig. 4.8 shows when operating the NiMoZn cathode for HER at current densities of 10 mA cm^{-2} analysis of hydrogen via gas chromatography (GC) analysis showed no hydrogen production indicating that NO$_3^-$ is preferentially reduced as opposed to protons.
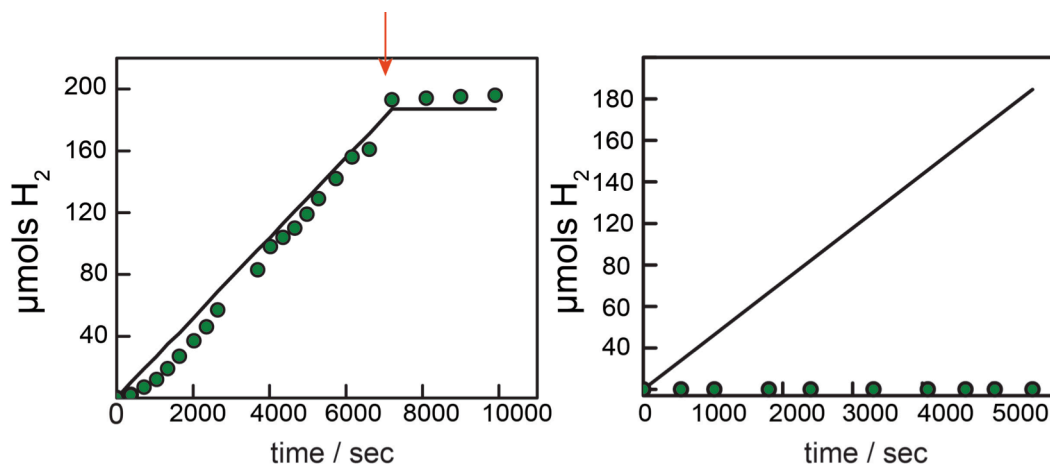
Figure 4.8 Gas quantification for NiMoZn cathode operating in **(left)** 0.5 M KBi / K$_2$SO$_4$ and **(right)** 0.5 M KB$_i$ / KNO$_3$ both at pH 9.2. The black line represents 100% Faradaic efficiency based on the charge passes during electrolysis. The green circles represent H$_2$ measured by gas chromatography. The red arrow indicates when electrolysis was stopped. GC analysis was conducted until the moles of gas measured in the headspace reached a steady–state. The lag period (——, black) in gas generation is due to the buildup of gases in the headspace of the EC cell.

Alternatively, using K$_2$SO$_4$ as a supporting electrolyte results in a Faradaic efficiency of 100%. Fig 4.9 shows that the NiB$_i$ anode operating in 0.5 M KB$_i$ / K$_2$SO$_4$

(pH 9.2) also demonstrates a 100% Faradaic efficiency.
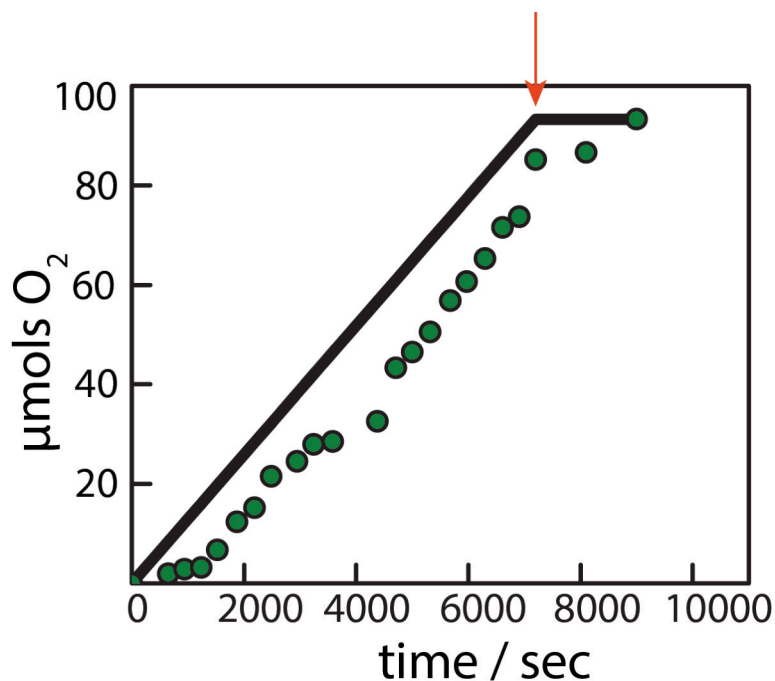
Figure 4.9 Gas quantification for NiB$_i$ cathode operating in (left) 0.5 M KB$_i$ / K$_2$SO$_4$ and at pH 9.2. The black line represents 100% Faradaic efficiency based on the charge passes during electrolysis. The green circles represent O$_2$ measured by gas chromatography. The red arrow indicates when electrolysis was stopped. GC analysis was conducted until the moles of gas measured in the headspace reached a steady–state. The lag period (——, black) in gas generation is due to the buildup of gases in the headspace of the EC cell.

Although the following gas quantification measurements indicate that 0.5 M

KB$_i$ / 0.5 M K$_2$SO$_4$ solution is a reasonable choice, K$_2$SO$_4$ is sparingly soluble at 0.5 M,

once again limiting the specific conductivity of our electrolyte to 90 mS cm^{-1} (Fig.

4.7).
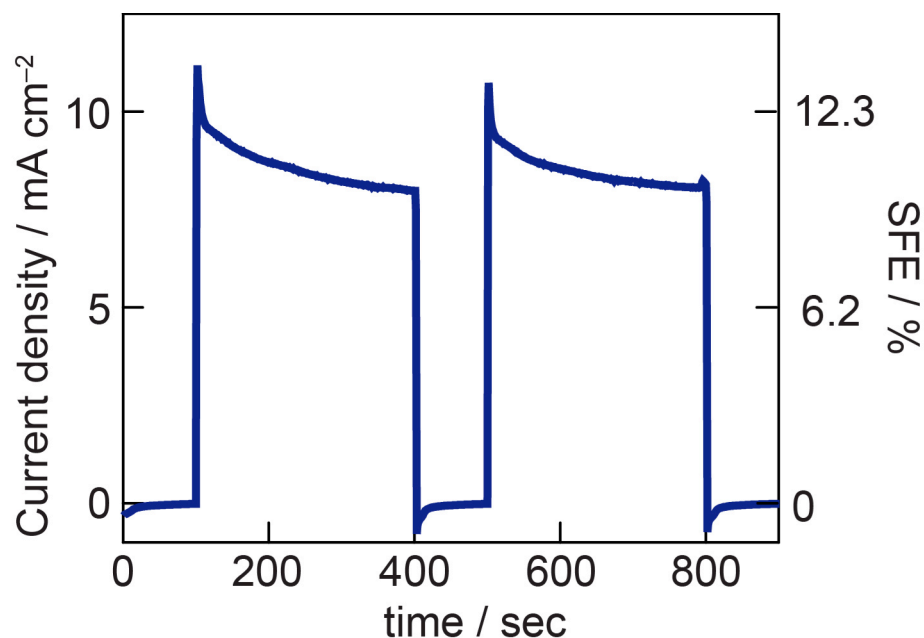
Figure 4.10 Current under chopped illumination representing J_{OP} for a PV–EC device composed of a 3–cell PV–module, a NiB$_i$ anode, and NiMoZn cathode operating in 1M KOH. Because KOH is a more conductive electrolyte, a 12% or greater SFE can be obtain with a 3–cell PV module as opposed to a 4–cell module. The initial drop in SFE is due to the decrease in PV efficiency, due to heating of the PV–module. The chopped illumination represents the recovery in SFE.

By moving to a more conductive electrolyte, such as 1 M KOH (pH 14), a 12% SFE can be obtained with a 3–cell mini–module as opposed to a 4–cell module (Fig. 4.10). This also shows how minimizing R_{SOL} shifts the EC curve closer the ideal curve obtained based on the Tafel analysis of the catalysts used herein (Fig. 4.11). However, it is preferential to avoid the deleterious effect of concentrated base on PV materials by maintaining neutral and near–neutral conditions. We thus prefer to minimize R_{SOL} by utilizing a flow–cell design and optimized cell geometry.[22–24]
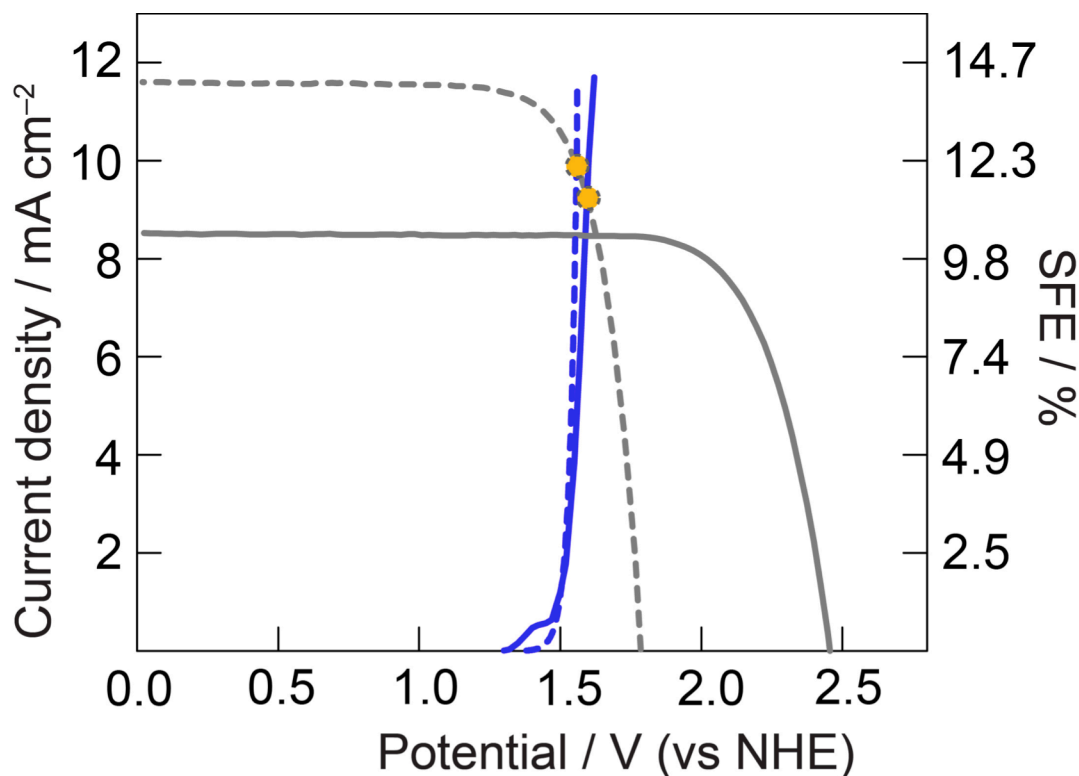
Figure 4.11 *J–V* curves of the individually measure PV and EC components making up the PV–EC device operating in 1M KOH. The grey curves represent the *J–V* curves for the PV modules composed of either three (-----, grey–dashed) or four (——, grey–solid) single–junction c–Si solar cells measure under AM 1.5 illumination. The blue curves represent electrochemical load *J–V* curves using NiB_i and NiMoZn catalysts, where the ideal EC curve (-----, blue–dashed) is based on previously reported Tafel analysis and the actual EC curve (——, blue–solid) measured in a 2–electrode experiment. The point of intersection represents the J_{OP} (●, orange circles) and the SFE of the coupled system.

The operational stability of the coupled PV–EC system showed no decline in J_{OP} for over a week of operation in 0.5 M KB_i pH 9.2 solution (Fig. 4.12). Interestingly, the SFE, inferred from the current, appears to slightly increase during the first 24 h of operation. This small recovery is attributed to a recovery cell voltage over the course of 24 h of illumination (blue line in Fig. 4.6). Initially, the module absorbs heat from the solar simulator photon flux, causing the initial decrease in PV efficiency.[20] Then, under constant illumination at higher temperatures, the observation of a gradual improvement in the current density over

a timescale of tens of hours is consistent with the evolution of the "oxygen–boron defect" a well– studied phenomenon in p–type Czochralski silicon.[25,26] Importantly, the observed fluctuations in J_{OP} can be attributed to fluctuations in the PV module output and are not related to the PV–EC coupling or EC reactions.
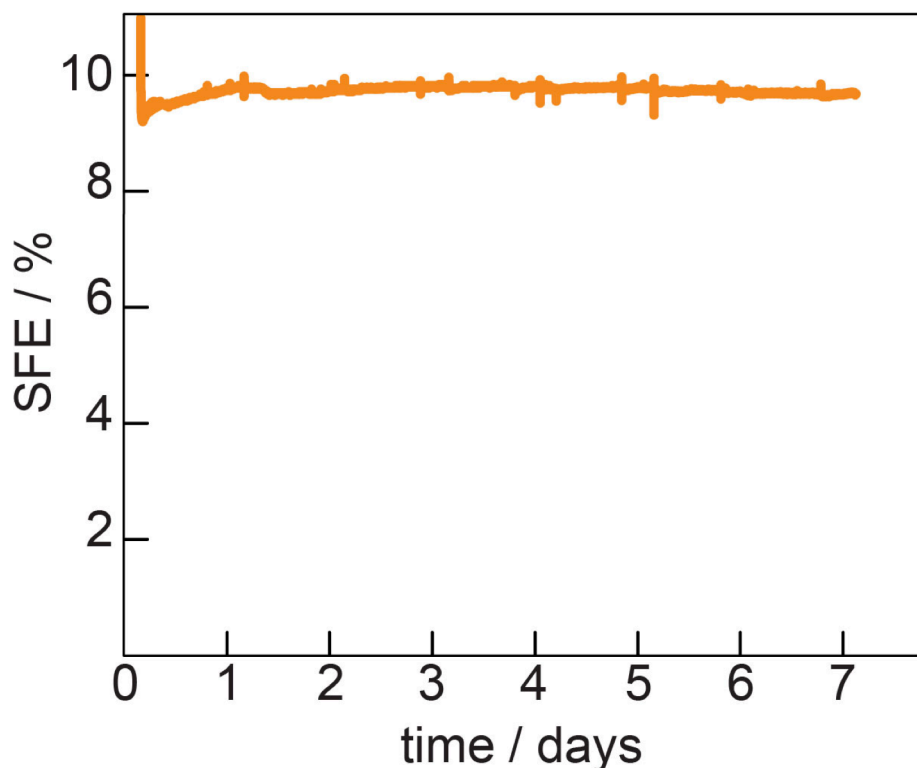
Figure 4.12 SFE inferred from J_{OP} for the PV–EC device operating in 0.5M KB_i / 0.5M K_2SO_4 pH 9.2 measured for over 7 days of operation showing no decrease in SFE over operation time. Spikes are due to the addition of solution to maintain the solution level and pH.

4.4 Conclusion

We demonstrate that an SFE efficiency of 10% can be achieved utilizing non–precious materials and c–Si. This proof of concept capitalizes on the declining cost of high–quality PV devices and earth–abundant catalysts operating under near neutral pH conditions. This modular design of the PV and EC components allows for a wide

variety or PV opposed materials, catalysts, and electrolytes to be implemented where no one component is constrained by the other. This methodology permits facile optimization and characterization. As PV–EC device sub–components reach technological maturity, an increasing emphasis will be placed on system design and integration.

4.5 Experimental

Materials and Methods. Nickel (II) chloride hexahydrate, boric acid, potassium hydroxide, potassium nitrate, potassium sulfate were purchased from Sigma Aldrich and used as received. Steel foil and nickel mesh were purchased from Strem.

Mini–Module Fabrication Crystalline silicon mini–modules were fabricated using commercially available single–junction Czochralski silicon solar cells with stand–alone efficiencies of 18%. Mini–cells were cut out of commercial size wafers by laser scribing with a 1064 nm pulsed laser and mechanical cleaving. Mini–cells were electrically connected via solar tabbing wire and silver epoxy. The mini–module was constructed by sequentially layering glass, EVA, solar cells, and EVA. The glass maintains structural integrity while EVA provides water protection. The mini–module was encapsulated using a double layer vacuum press heated to 120 °C. With the module in the lower chamber of the vacuum press, both the upper and lower chambers were held under vacuum for 5 min. The upper chamber was vented to atmospheric pressure for 5 min to remove air bubbles through the induced pressure difference between the two chambers. The lower chamber was vented and

the mini–module was allowed to cool to room temperature. Excess EVA was removed and the mini–module was stored to protect against mechanical and water degradation.

After laser–cutting the commercial cells, connecting four in series, and encapsulating them with ethylene vinyl acetate, the mini–module efficiency was 16%. The equivalent mini–module for a three–cell series is 15.8%.

Electrochemical methods. Electrochemical experiments were performed using a CH–Instruments 760D potentiostat. For three–electrode measurements potentials were measured against an Ag/AgCl reference electrode (BASi) and converted to NHE by adding 0.197 V. For two electrode experiments the working electrode lead of the potentiostat was connected to the anode and the reference and auxiliary leads of the potentiostat were connected to the cathode.

Catalyst formation. The NiB_i anode was electrodeposited in a two–compartment electrochemical cell with a glass frit junction. The working compartment was charged with ~25 mL of 0.2 M B_i electrolyte and 25 mL of a 1 mM Ni^{2+} solution. The working electrode was a steel substrate, and the NiB_i catalyst was deposited by applying a voltage of 0.95 V (vs. Ag/AgCl) for 1 h. To improve anode activity the electrodes were then anodized at 0.9 V (vs. Ag/AgCl) in 1 M KOH for 1 h

The NiMoZn cathode was electrodeposited from a solution of nickel(II) chloride hexahydrate (9.51 g L^{-1}), sodium molybdate dihydrate (4.84 g L^{-1}), anhydrous zinc chloride (0.0409 g L^{-1}), tetrabasic sodium pyrophosphate (34.57 g L^{-1}) and sodium bicarbonate (74.77 g L^{-1}; VWR). Hydrazine hydrate (1.21 mL L^{-1}) was added immediately before plating. NiMoZn was deposited onto a Ni mesh

substrate that had been pre–treated at 2 V vs. Ag/AgCl in 0.5 M H_2SO_4 for 3 min. The

NiMoZn alloy was deposited at a voltage of 1.8 V (vs. Ag/AgCl) for 30 min. The

deposit was left to de–alloy overnight in 6 M KOH.[7,17]

NiB_i product crossover. H_2 oxidation at the NiB_i anode was examined via

the steady–state activity of the anode in Ar saturated and H_2 saturated 0.5 M KB_i /

K_2SO_4 solution at pH 9.2. The amount of voltage required to achieve a given steady–

sate current–density in both cases was the same indicating that the contribution J_{OP}

as a consequence of H_2 oxidation is negligible.

Photoelectrochemical measurements. The NiB_i anode and NiMoZn

cathode were connected in series with the c–Si mini–module. The light source was a

Sol 2A solar simulator (Newport Corp.). The current through the PV–EC device was

measured by using the potentiostat as an ammeter. In all cases, the area used to

convert current to current–density was the active–area of the c–Si mini–module.

Additionally, the geometric area of the anode and cathode was scaled to match that

of the mini–module. For long–term stability measurements, fresh KB_i buffer solution

was added in order to maintain the solution lost to evaporation as well as pH.

Gas quantification. The Faradaic efficiency for each electrode was evaluated

using gas chromatography. The experiment was performed galvanostatically using a

three–electrode configuration in a custom built two–compartment gas–tight

electrochemical cell. The working electrode was either NiB_i on a steel substrate for

O_2 quantification, or NiMoZn on a nickel mesh substrate for H_2 quantification. The

working electrode operated at a constant current density of 10 mA cm^{-2} for 2 h.

During the course of the experiment, samples of evolved gas were removed from the

headspace and injected into the GC. In order to ensure that the evolved gas reached

a steady state value in the headspace, GC measurements were recorded for 1 h after

cessation of electrolysis. The data was converted into partial pressure of gas in the

headspace using calibration curves defined from known mixtures of H_2/N_2 or O_2/N_2.

The partial pressure of gas was converted to µmol, and corrected using Henry's law

to account for the gas dissolved in solution. The total charge passed during

electrolysis was divided by nF (n corresponding to the number of electrons in each

half reaction) to furnish the calculated gas yield. The total calculated and

experimental gas yields were used to determine the Faradaic efficiency.

4.6 References

1. Khaselev O, Bansal A, Turner JA (2001) High–efficiency integrated multijunction photovoltaic/electrolysis systems for hydrogen production. *Int. J. Hydrog. Energy* **26**, 127–132.

2. Office of Energy Efficiency and Renewable Energy (2014) *Hydrogen, fuel cells, & infrastructure technologies program* (U.S. Department of Energy, Washington DC, USA)

3. Grätzel M (2007) Photovoltaic and photoelectrochemical conversion of solar enegy. Phil. Trans. R. Soc. A. **365**, 993–1005.

4. Licht S et al. (2000) Efficient solar water splitting, exemplified by RuO2–catalyzed AlGaAs/Si Photoelectrolysis. *J. Phys. Chem. B* **104**, 8920–8924.

5. Miller EL, Rocheleau RE, Deng XM (2003) Design considerations for a hybrid amorphous silicon/photoelectrochemical multijunction cell for hydrogen production. *Int. J. Hydrog. Energy* **28**, 615–623.

6. Kelly NA, Gibson TL (2006) Design and characterization of a robus tphotoelectrochemical device to generate hydrogen using solar water splitting. **31**, 1658–1673.

7. Reece SY et al. (2011) Wireless solar water splitting using silicon–based semiconductors and earth–abundant catalysts. *Science* **334**, 645–648.

8. Cristino V et al. (2013) Efficient solar water oxidation using photovoltaic devices functionalized with earth–abundant oxygen evolving catalysts. *Phys. Chem. Chem. Phys.* **15**, 13083–13092.

9. Jin J, Walczak K, Singh MR, Karp C, Lewis NS, Xiang C (2014) An experimental and modeling/simulation and operational performance, characteristics of and integrated, membrane–free, neutral pH solar–driven water–splitting system. *Energy Environ. Sci.* doi: 10.1039/C4EE01824A

10. Jacobsson TJ, Platzer–Björkman C, Edoff M, Edvinsson T (2013) CuInxGa1−xSe2 as an efficient photocathode for solar hydrogen generation. *Int J Hydrog Energy* **38**,15027–15035.

11. Jacobsson TJ, Fjällström V, Sahlberg M, Edoff M, Edvinsson T (2013) A monolithic device for solar water splitting based on series interconnected thin film absorbers reaching over 10% solar–to–hydrogen efficiency. *Energy Environ. Sci*. **6**, 3676–3683.

12. Nocera DG (2012) The artificial leaf. *Acc. Chem. Res.* **45**, 767–776.

13. Green MA, Emery K, Hishikawa Y, Warta W, Dunlop ED (2012) Solar cell efficiency tables (version 39). *Prog Photovolt Res Appl* **20**, 12–20.

14. Bagnall DM, Boreland M (2008) Photovoltaic technologies. *Energy Policy* **36**, 4390–4396.

15. Winkler MT, Cox CR, Nocera DG, Buonassisi T (2013) Modeling integrated photovoltaic–electrochemical devices using steady–state equivalent circuits. *Proc. Natl. Acad. Sci.* **110**, E1076–E1082.

16. Bediako DK, Surendranath Y, Nocera DG (2013) Mechanistic studies of the oxygen evolution reaction mediated by a nickel–borate thin film electrocatalyst. *J. Am. Chem. Soc.* **135**, 3662–3674.

17. Reece SY, Esswein AJ, Sung K, Green Z, Nocera DG (2013) *Compositions, electrodes, methods, and mystems for water electrolysis and other electrochemical techniques. US Patent Appl. No.* 8361288.

18. Chen Z et al. (2010) Accelerating Materials Development for Photoelectrochemical Hydrogen Production: Standards for Methods, Definitions, and Reporting Protocols. *J. Mater. Res.* **25**, 3–16.

19. Bockris JO, Reddy AKN, Gamboa–Aldeco ME (1998) *Modern electrochemistry* (New York: Plenum Press, c1998–c2000).

20. Jones AD, Underwood CP (2001) A thermal model for photovoltaic systems. *Sol Energy* 70:349–359.

21. Hernández–Pagán EA et al. (2012) Resistance and polarization losses in aqueous buffer–membrane electrolytes for water–splitting photoelectrochemical cells. *Energy Environ. Sci.* **5**, 7582–7589.

22. Modestino MA et al. (2013) Robust production of purified H2 in a stable, self–regulating, and continuously operating solar fuel generator. *Energy Environ. Sci.* **7**, 297–301.

23. Haussener S et al. (2012) Modeling, simulation, and design criteria for photoelectrochemical water–splitting systems. *Energy Environ. Sci.* **5**, 9922–9935.

24. Newman J (2013) Scaling with Ohm's Law; wired vs. wireless photoelectrochemical cells. *J. Electrochem. Soc.* **160**, F309–F311.

25.   Schmidt J, Bothe K (2004) Structure and transformation of the metastable boron– and oxygen–related defect center in crystalline silicon. *Phys. Rev. B* **69**, 024107.

26.   Bianca Lim KB (2008) Deactivation of the boron–oxygen recombination center in silicon by illumination at elevated temperature. *Phys. Status Solidi RRL – Rapid Res. Lett.* **2**, 93–95.

Chapter 5–Future Directions

5.1 Introduction

The previous chapters present a completely modular proof–of–concept approach for direct solar–to–fuels conversion using all earth–abundant and technology ready materials. Stand–alone photovoltaic–electrochemical (PV–EC) devices have been created with few design constraints on each component. Continued advances may be made with consideration of alternative materials and concepts for various components of a PV–EC design. Given the versatility of utilizing buried–junction photovoltaics, modifications to the PV–EC design are straightforward. The following chapter discusses alternative concepts and preliminary results for each component of the PV–EC device, which may allow for further improvements in efficiency, cost reduction, and design integration.

5.2 Alternative PV materials

Although crystalline silicon (c–Si) is a high quality material and is an economically viable PV resource, the fact that the solar–to–electrical power efficiency is reaching its thermodynamic limit sets a ceiling on drastic improvements in SFE.[1,2] Additionally, a large portion of the current price for c–Si PV modules is encumbered by balance of systems costs (BOS) as opposed to the price of silicon itself, and it remains unclear if these BOS costs can be significantly reduced.[3,4] Very recently, thin–film PV's consisting of a perovskite absorber, typically $CH_3NH_3PbX_3$ (X = Br, I), sandwiched between a TiO_2 electron conducting layer and an organic hole transporting material (typically spiro–OMeTAD), have emerged as a formidable alternative to c–Si PV's. Perovskite PV's were first introduced in 2009.[5]

Since that time, laboratory scale cells have shown a rapid improvement in solar–to–electrical power efficiency from 10% in 2012 to a record 19.3%%;[6,7] a band–gap of ~1.5 eV with a predicted practical efficiency of 20% speaks to their promise as a future PV material.[8] Moreover, perovskite PVs can be constructed from various low–cost liquid phase chemical reactions and deposition methods such as spin–coating or spray–pyrolysis.[9] Although yet to be implemented on commercial scale, the estimated cost for a perovskite solar cell could be as low as $0.30 W_P^{-1}.[10]

Despite the swift emergence of high efficiency perovskite PVs, current drawbacks include scalability, stability, and environmental safety. Currently, most of the high efficiency perovskite PV's have only been demonstrated to perform on small scales of 0.1 cm^2 or less.[11] Larger scales devices result in lower fill factors, decreasing the PV efficiency. The reason for the loss in fil–factors is unclear, but it is proposed that it due to series resistance through the device.[12] Additionally since perovskites are water–soluble, there is concern about the long–term operation time and the possibility of Pb leaking into the environment. Substitution of Sn^{2+} for Pb^{2+} is promising from the viewpoint of toxicity, but Sn–based perovskites so far have only been stable in a nitrogen environment and have yet to reach efficiencies close to the Pb–based devices.[13,14]

For solar–water–splitting applications, perovskites should be investigated. In order to use perovskite PVs either a series–connected approach can be adopted or alternatively perovskites could be used the top cell in a tandem configuration. For example a perovskite–silicon tandem PV constructed from a 17% efficient perovskite PV and a 23–24% c–Si solar cell could produce a 29.6% PV efficiency.[15]

These properties suggest that these materials combined in a buried junction approach may be a very promising future line of inquiry.

5.3 Alternative catalyst deposition methods

So far the research our group has focused on solution–based electrodeposition of Co, Ni, and Mn oxygen evolution catalysts (OECs) and NiMoZn alloys for hydrogen evolution catalyst (HECs). Years of research has given insight on film formation and optimization of catalyst activity.[16–20] However, due to the highly oxidizing or reducing conditions required for electrodeposition methods, it may not always be the most viable option for direct integration of catalysts with PV materials. An alternative approach for catalyst deposition, vapor deposition techniques such as atomic–layer deposition (ALD), chemical vapor deposition (CVD), electron–beam deposition (E–beam), and sputtering may be an interesting approach for catalyst integration to the PV. Vapor–deposition techniques for direct integration of catalysts with PV devices are superior in terms of controlling film thickness and conformity. Additionally, vapor–deposition techniques and may be better in terms of high throughput manufacturing. Recently E–beam evaporation and ALD have been used to deposit ultra–thin nickel or cobalt films onto silicon and function as both a protective layer and upon oxidation an OER catalyst.[21–23] Interestingly, it has also been observed that the oxidation of such crystalline cobalt and nickel films used for OER catalysts become amorphous over the course of operation and then resemble electrodeposited versions of Co or Ni–OEC's developed in our lab.[21,24,25] These structural changes are important since amorphous

electrodeposited OECs are known to exhibit a porous film morphology. Therefore, while a compact vapor–deposited film may initially appear promising as a dual protective–layer and catalyst material, over the course of operation time it may become porous to expose the underlying PV. It is important to determine if the vapor–deposited films will demonstrate the same electrochemical activity as the electrodeposited versions and if structural changes occur over the course of operation time.

Preliminary studies have evaluated the catalytic activity via Tafel analysis for water–oxidation of a sputtered NiFeO film. Tafel analysis shows that this catalyst achieves a 45 mV decade^{-1} Tafel slope making it a highly active OER catalyst. Of significance, in contrast to the electrodeposited Co, Ni, and Mn–OECs, which are
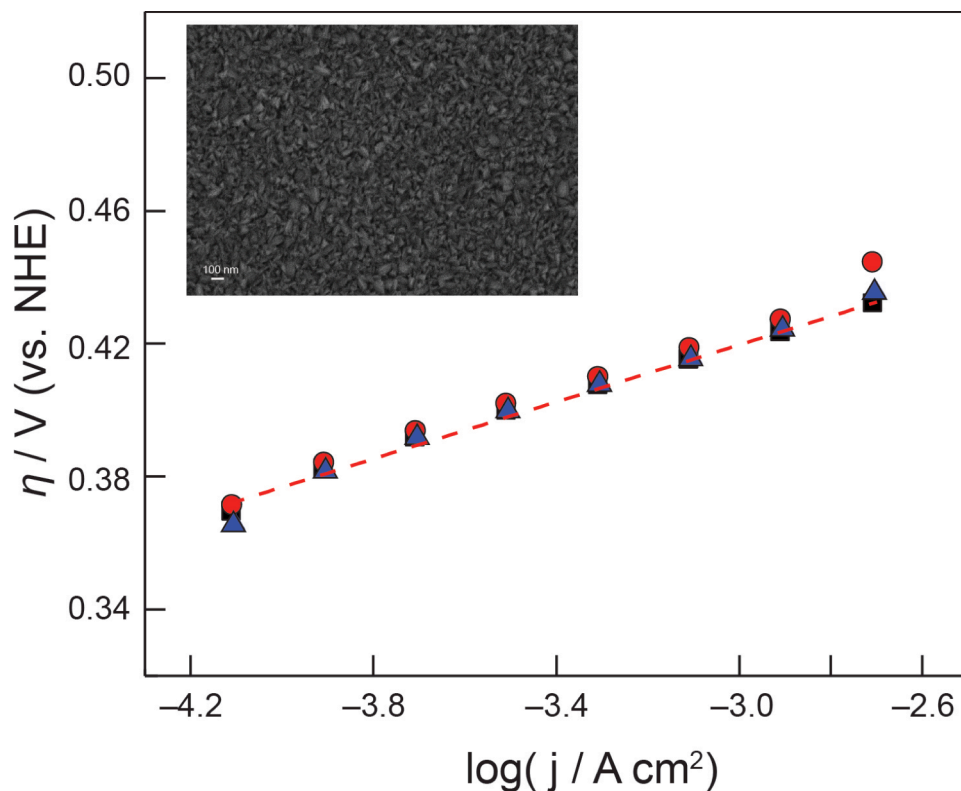
Figure 5.1 Tafel plot of a sputtered NiFeO OER catalyst operating in 0.5 M KB$_i$ / 1.5M KNO$_3$ pH 9.2. A Tafel slope of 45 mV decade^{-1} is observed for a 50nm (■), 100nm (●) and 200nm (▲) thick NiFeO film. **Inset:** SEM image of a NiFeO shows a very dense, compact film.

porous in nature, NiFeO appears to show little improvement in activity with increased catalyst thickness (Fig. 5.1) implying that the sputtered NiFeO catalyst is a very dense film (Fig 5.1 inset). Additionally initial results also show that the NiFeO catalyst demonstrates different catalytic activity depending on the operational pH of the solution indicating that catalyst activity and therefore likely the mechanism changes with pH (Fig 5.2). This unusual behavior suggests that further analysis is

required to fully how this dense catalyst operates.
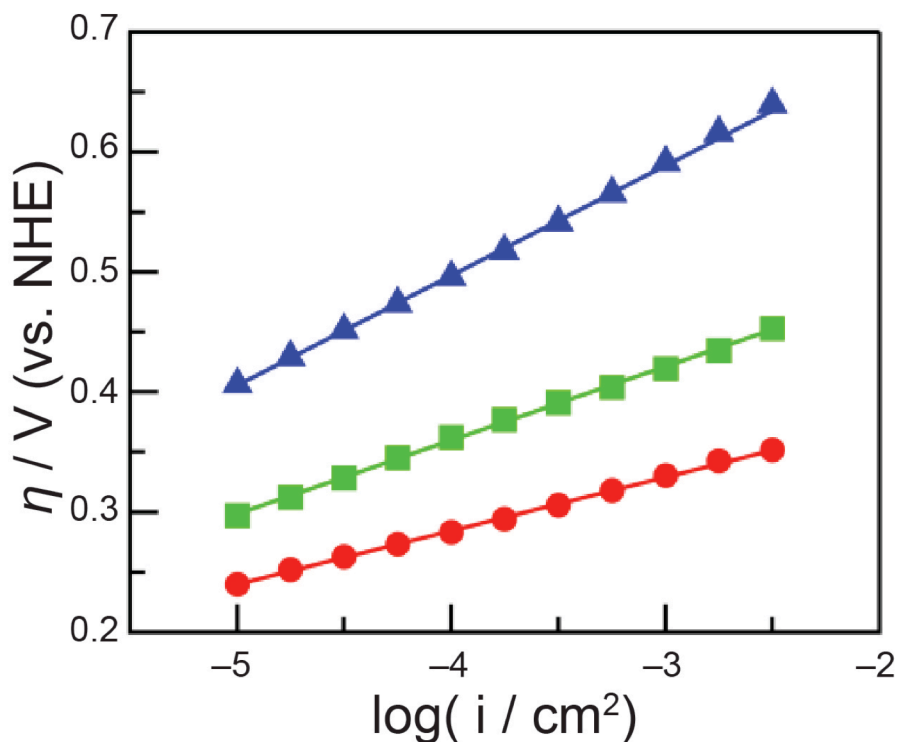
Figure 5.2 Tafel plots of 200 nm thick NiFeO (81% mol Ni, 19% mol Fe) on Ni–coated glass operated in (▲) 0.2 M KP_i, pH 7.0, 92 mV decade^{-1} slope; (■) 0.2 M KB_i, pH 9.3, 61 mV decade^{-1} slope; (●) 1.0 M KOH, pH 13.9, 45 mV decade^{-1} slope.

Previous work has shown that the CoP_i catalyst can be made by first sputtering a thick film of metallic cobalt (800 nm) followed by subsequent electrochemical anodization in phosphate buffer.[26–28] However, the catalytic activity of the films formed from metallic cobalt exhibited inferior activity as compared to those made from solution electrodeposition. We ascribe this difference in behavior to slow charge transport through the thick films. Studies on electrodeposited Co–OEC's showed that (a) the structure and thickness influences the charge transfer through the films, and (b) films deposited from borate

solutions, rather than phosphate, produce films with an extended structure that improves charge transfer through the film.[17,20,29,30] Preliminary results show that the same is true when forming the Co–OEC from metallic films. Anodizing the metallic film in KB$_i$ as opposed to KP$_i$ solution, lowers the Tafel slope from 100
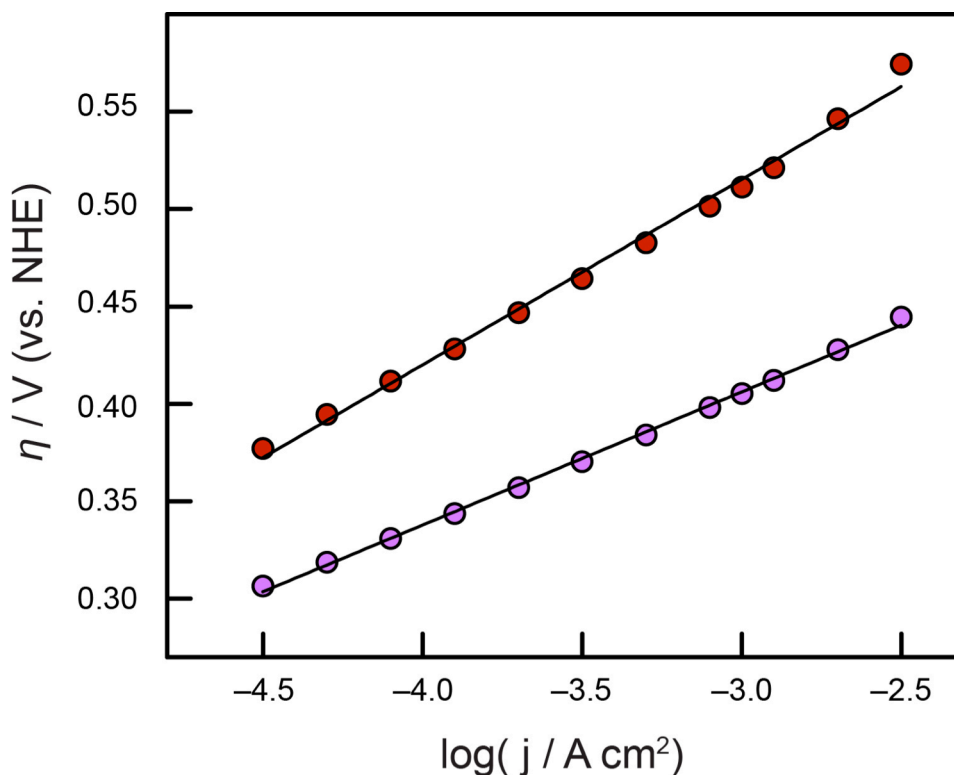

Figure 5.3 Tafel analysis of Co–OEC films formed and operated in KB$_i$ (●) as opposed to KP$_i$ (●) solution. The films formed from KB$_i$ exhibit a lower Tafel slope and therefore demonstrate higher activity than those formed in KP$_i$.

to 60 mV/decade, which matches the activity of the electrodeposited catalyst (Fig.

5.3).
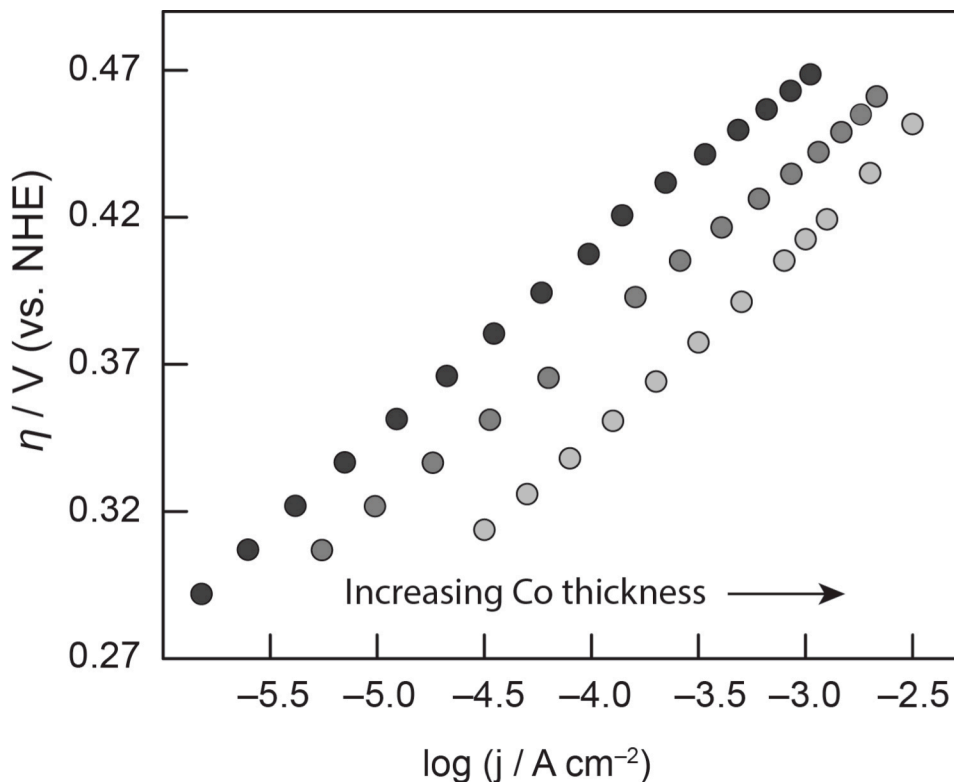
Figure 5.4 Tafel analysis of Co–OEC's formed from anodizing metallic cobalt in KB$_i$ solution. In all cases the Co–OEC exhibits a Tafel slope of 60 mV decade^{-1}, however starting with thicker metallic films produces Co–OEC's with higher activity than thinner films.

Additionally, the activity of CoB$_i$ films made from metallic cobalt demonstrate an increase in catalytic activity with increased film thickness suggesting that the catalyst films do exhibit some porosity as opposed to terminating in a thin–layer on the surface of the metallic film (Fig. 5.4). Future work to define the parameters for precise control over films formed from vapor deposition techniques and their subsequent activity should be undertaken.

5.4 Cell design

Since many semiconductors are unstable in strongly acidic or basic solutions, working in moderate pH regimes relaxes the stability constraint on PV devices. However, solution resistance (R_{SOL}) is low in strongly acidic or basic solutions. Due to the solubility limits of buffers when working under moderate pH conditions, the concentrations of protons and hydroxide ions are quite low and addition of an inert salt (i.e. a supporting electrolyte) is needed to carry the ionic current.[31,32] However, as shown in Chapter 4, use of a supporting electrolyte still doesn't compete with strong acids or bases in terms of minimizing solution resistance. Recent developments have shown that utilization of novel flow–cell designs can circumvent some of the ion–transport problems imposed by solution resistance.[32] Moreover, some cell configurations require the use of membranes in order to prevent mixing of of H_2 and O_2 which could lead to safety concerns. Typically these membranes are either Nafion or anion/cation exchange membranes.[31,32]When introducing a membrane additional resistive losses are imposed due to the added resistance of the membrane as well as formation of undesirable concentration gradients in the anodic and cathodic compartments. These additional components increase the voltage required for water–splitting as follows:

$$V_{EC}(J_{EC}) = V_{th} + \eta_{OER}(J_{EC}) + \eta_{HER}(J_{EC}) + \eta_R(J_{EC}) + \eta_{MEM}(J_{EC}) + \eta_{pH}(J_{EC})$$

(5.1)

where η_{MEM} is the membrane resistance and η_{pH} is the overpotential caused by pH gradients in solution. It has been modeled and demonstrated that η_{MEM} can be

optimized by modifying the thickness and porosity of the membrane.[33,34] However, a more elegant solution is required in order to prevent pH gradients from forming at the anode and cathode.
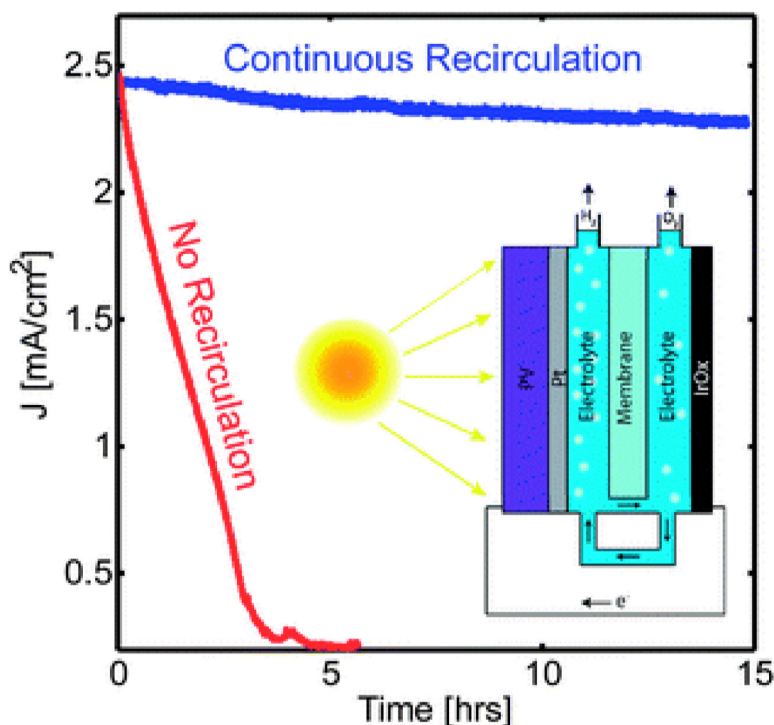
Figure 5.5 The current density traces show that recirculating streams allow the device to function stably and continuously (purple trace), while without recirculation the device performance deteriorates as concentration gradients form across the cell and ionic species are depleted in the oxygen–evolution side(red trace). The inset in the graph corresponds to a schematic representation of the parallel–plate solar–hydrogen generator. Reprinted with permission from reference 32.

Recently, work by Modestino et. al has shown that a flow–cell design with a controlled recirculating stream can prevent pH changes between the anode and cathode compartments.[32] Additionally, they incorporated a PV–EC device consisting of a high–efficiency triple–junction $GaInP_2$/GaAs/Ge solar cell connected to an iridium–oxide anode for oxygen–evolution and a platinum cathode on the hydrogen–evolution, separated by a thin Nafion membrane and 1M KB_i as an

electrolyte. Utilizing a controlled recirculating stream between compartments, they showed that pH gradients didn't form and demonstrated a solar–to–fuel efficiency of 6.2%, that operated continuously for 15 hours (Fig. 5.5).

5.5 Conclusion

The future challenges in solar–water–splitting stem primarily from low–cost of PV and EC components while integrating all the necessary components to produce a high efficiency and robust system. Alternative materials, designs, and concepts that can be applied to create next generation PV–EC devices.

5.6 Experimental

Electrochemical Methods. Electrochemical experiments were performed in a two–compartment electrochemical cell using a CH Instruments 760C or 760D potentiostat and an Ag/AgCl reference electrode (BASi, MF–2052). All electrode potentials were converted to the NHE scale using $E(NHE) = E(Ag/AgCl) + 0.197$ V. Platinum mesh (Alfa Aesar) was used as the auxiliary electrode. Unless otherwise stated, the electrolyte was 0.5 M KB_i at a pH of 9.2 with 1.5 M KNO_3 as a supporting electrolyte.

Catalyst Film Preparation NiFeO catalyst films were deposited by reactive sputtering using the AJA International sputtering system. Films were deposited by reactive sputtering from an iron–doped nickel sputtering target (19% Fe) in an Ar:O_2 atmosphere of 3:1.[35] Co–OEC's were made by sputtering metallic cobalt onto a FTO electrode. The metallic films were anodized in either 0.2M P_i or 0.2M B_i for 20

109

hours at a current density of 1 mA cm^{-2}. The films were then rinsed and subsequent

Tafel analysis was conducted in either 1.0M KP$_i$ or KB$_i$ electrolyte at pH 7 or 9.2,

respectively.

5.7 References

1.   Swanson RM (2005) in *Conference Record of the Thirty–first IEEE Photovoltaic Specialists Conference, 2005*, pp 889–894.

2.   Green MA (2009) The path to 25% silicon solar cell efficiency: history of silicon cell evolution. *Prog. Photovolt. Res. Appl.* **17**, 183–189.

3.   Powell DM et al. (2012) Crystalline silicon photovoltaics: a cost analysis framework for determining technology pathways to reach baseload electricity costs. *Energy Environ. Sci.* **5,** 5874–5883.

4.   Bazilian M et al. (2013) Re–considering the economics of photovoltaic power. *Renew. Energy* **53**, 329–338.

5.   Kojima A, Teshima K, Shirai Y, Miyasaka T (2009) Organometal halide perovskites as visible–light sensitizers for photovoltaic cells. *J. Am. Chem. Soc.* **131**, 6050–6051.

6.   Wojciechowski K, Saliba M, Leijtens T, Abate A, Snaith HJ (2014) Sub–150 °C processed meso–superstructured perovskite solar cells with enhanced efficiency. *Energy Environ. Sci.* **7**, 1142–1147.

7.   Zhou H et al. (2014) Interface engineering of highly efficient perovskite solar cells. *Science* **345**, 542–546.

8.   Park N–G (2013) Organometal Perovskite Light Absorbers Toward a 20% efficiency low–cost solid–state mesoscopic solar cell. *J. Phys. Chem. Lett.* **4**, 2423–2429.

9.   Nazeeruddin MK, Gao P, Grätzel M (2014) Organohalide lead perovskites for photovoltaic applications. *Energy Environ. Sci*. Available at: http://pubs.rsc.org/en/content/articlelanding/2014/ee/c4ee00942h [Accessed May 27, 2014].

10.   Green MA, Ho–Baillie A, Snaith HJ (2014) The emergence of perovskite solar cells. *Nat. Photonics* **8**, 506–514.

11.   Hodes G, Cahen D (2014) Photovoltaics: Perovskite cells roll forward. *Nat. Photonics* **8**, 87–88.

12.   Sum TC, Mathews N (2014) Advancements in Perovskite Solar Cells: Photophysics behind the Photovoltaics. *Energy Environ. Sci*. Available at:

http://pubs.rsc.org/en/content/articlelanding/2014/ee/c4ee00673a
[Accessed May 7, 2014].

13. Noel NK et al. (2014) Lead–free organic–inorganic tin halide perovskites for photovoltaic applications. *Energy Environ. Sci*. Available at: http://pubs.rsc.org/en/content/articlelanding/2014/ee/c4ee01076k [Accessed August 5, 2014].

14. Hao F, Stoumpos CC, Cao DH, Chang RPH, Kanatzidis MG (2014) Lead–free solid–state organic–inorganic halide perovskite solar cells. *Nat. Photonics* **8**, 489–494.

15. Snaith HJ (2013) Perovskites: The Emergence of a new era for low–cost, high–efficiency solar cells. *J. Phys. Chem. Lett.* **4**, 3623–3630.

16. Surendranath Y, Kanan MW, Nocera DG (2010) Mechanistic studies of the oxygen evolution reaction by a cobalt–phosphate catalyst at neutral pH. *J. Am. Chem. Soc.* **132**, 16501–16509.

17. Surendranath Y, Lutterman DA, Liu Y, Nocera DG (2012) Nucleation, growth, and repair of a cobalt–based oxygen evolving catalyst. *J. Am. Chem. Soc.* **134**, 6326–6336.

18. Bediako DK et al. (2012) Structure–activity correlations in a nickel–borate oxygen evolution catalyst. *J. Am. Chem. Soc.* **134**, 6801–6809.

19. Bediako DK, Surendranath Y, Nocera DG (2013) Mechanistic studies of the oxygen evolution reaction mediated by a nickel–borate thin film electrocatalyst. *J. Am. Chem. Soc.* **135**, 3662–3674.

20. Huynh M, Bediako DK, Liu Y, Nocera DG (2014) Nucleation and growth mechanisms of an electrodeposited manganese oxide oxygen evolution catalyst. *J. Phys. Chem. C*. Available at: http://dx.doi.org/10.1021/jp501768n [Accessed June 12, 2014].

21. Kenney MJ et al. (2013) High–performance silicon photoanodes passivated with ultrathin nickel films for water oxidation. *Science* **342**, 836–840.

22. Hu S et al. (2014) Amorphous TiO2 coatings stabilize Si, GaAs, and GaP photoanodes for efficient water oxidation. *Science* **344**,1005–1009.

23. Yang J et al. (2014) Efficient and sustained photoelectrochemical water oxidation by cobalt oxide/silicon photoanodes with nanotextured interfaces. *J. Am. Chem. Soc.* **136**, 6191–6194.

24. Lee SW et al. (2012) The nature of lithium battery materials under oxygen evolution reaction conditions. *J. Am. Chem. Soc.* **134**, 16959–16962.

25. Risch M et al. (2013) Structural changes of cobalt–based perovskites upon water oxidation investigated by EXAFS. *J. Phys. Chem. C* **117**, 8628–8635.

26. Young ER, Nocera DG, Bulović V (2010) Direct formation of a water oxidation catalyst from thin–film cobalt. *Energy Environ. Sci.* **3**, 1726–1728.

27. Young ER, Costi R, Paydavosi S, Nocera DG, Bulović V (2011) Photo–assisted water oxidation with cobalt–based catalyst formed from thin–film cobalt metal on silicon photoanodes. *Energy Env. Sci.* **4**, 2058–2061.

28. Costi R, Young ER, Bulović V, Nocera DG (2013) Stabilized CdSe–CoPi Composite Photoanode for Light–Assisted Water Oxidation by Transformation of a CdSe/Cobalt Metal Thin Film. *ACS Appl. Mater. Interfaces* **5**:2364–2367.

29. Farrow CL, Bediako DK, Surendranath Y, Nocera DG, Billinge SJL (2013) Intermediate–range structure of self–assembled cobalt–based oxygen–evolving catalyst. *J. Am. Chem. Soc.* **135**, 6403–6406.

30. Bediako DK, Costentin C, Jones EC, Nocera DG, Savéant J–M (2013) Proton–electron transport and transfer in electrocatalytic films. Application to a cobalt–based O2–evolution catalyst. *J. Am. Chem. Soc.* **135**, 10492–10502.

31. Hernández–Pagán EA et al. (2012) Resistance and polarization losses in aqueous buffer–membrane electrolytes for water–splitting photoelectrochemical cells. *Energy Environ. Sci.* **5**, 7582–7589.

32. Modestino MA et al. (2013) Robust production of purified H2 in a stable, self–regulating, and continuously operating solar fuel generator. *Energy Environ. Sci.* **7**, 297–301.

33. Haussener S et al. (2012) Modeling, simulation, and design criteria for photoelectrochemical water–splitting systems. *Energy Environ. Sci.* **5**, 9922–9935.

34. Berger A, Segalman RA, Newman J (2014) Material Requirements for Membrane Separators in a Water–Splitting Photoelectrochemical Cell. *Energy Environ Sci*. Available at: http://pubs.rsc.org/en/content/articlelanding/2014/ee/c3ee43807d [Accessed February 12, 2014].

35. Miller EL, Rocheleau RE (1997) Electrochemical behavior of reactively sputtered iron–doped nickel oxide. *J. Electrochem. Soc.* **144**, 3072–3077.